NASA TM X-249

TECHNICAL MEMORANDUM

X-249

AERODYNAMIC AND HYDRODYNAMIC CHARACTERISTICS OF A PROPOSED SUPERSONIC MULTIJET WATER-BASED HULL-TYPE AIRPLANE WITH A VARIABLE-INCIDENCE WING

By William W. Petynia, Albin O. Pearson, and Roger H. Fournier

Langley Research Center
Langley Field, Va.

NATIONAL AERONAUTICS AND SPACE ADMINISTRATION

WASHINGTON

April 1960

NATIONAL AERONAUTICS AND SPACE ADMINISTRATION

TECHNICAL MEMORANDUM X-249

AERODYNAMIC AND HYDRODYNAMIC CHARACTERISTICS OF A PROPOSED SUPERSONIC MULTIJET WATER-BASED HULL-TYPE AIRPLANE WITH A VARIABLE-INCIDENCE WING*

By William W. Petynia, Albin O. Pearson, and Roger H. Fournier

SUMMARY

The aerodynamic and hydrodynamic characteristics of a supersonic multijet water-based airplane with and without modifications have been investigated. The results of tests of the stepped-hull-type configuration have indicated that the drag rise occurs near a Mach number of 0.94. At the design Mach number of 2.0, the maximum lift-drag ratio was approximately 4.0, the same as that of a hydro-ski version of the same basic configuration. All configurations were stable up to the design Mach number.

Excess thrust was available for a take-off in 42 seconds for a distance of 7,000 feet. With afterbody flow deflectors, the high-speed resistance was reduced by about 46 percent, a reduction which resulted in a 30-second take-off time and 5,000-foot take-off distance comparable with those of the hydro-ski version. The stability and spray during take-off and landing were satisfactory.

INTRODUCTION

The high-speed-seaplane research program undertaken at the Langley Research Center has included investigations of the performance capabilities of a number of design configurations based on various mission requirements. (See refs. 1 to 6.) These airplanes have exhibited suitable aerodynamic qualities without impairment of the hydrodynamic performance.

*Title, Unclassified.

One of these missions required a high-speed water-based bomber capable of a Mach 2 dash and a 1,500-nautical-mile combat radius. One approach to such an airplane made use of a variable incidence wing with a fuselage-type hull and a retractable hydro-ski (ref. 1). Another design solution is a hull-type configuration having, as nearly as possible, the same basic performance capabilities. The present report describes such an approach. The rounded fuselage (ref. 1) was modified to incorporate a hull-type vee-bottom with a conventional step with forebody and afterbody planing surfaces. In other respects, the general arrangement of the components and the aerodynamic surfaces were the same as the hydro-ski configuration of reference 1.

In the present investigation, the wind-tunnel and tank evaluations of the basic configuration were made. The effects of vertical chine strips, rounded chines, step fairings, and wingtip floats on the aerodynamic characteristics were determined.

SYMBOLS

Aerodynamic

All aerodynamic data have been reduced to standard nondimensional coefficients. The wind-tunnel data are referred to the axis system shown in figure 1 with the axes originating in the model plane of symmetry at 35 percent of the mean aerodynamic chord in the wing-chord plane and 26.6 percent of the mean aerodynamic chord above the hull baseline.

C_L lift coefficient, $\frac{\text{Lift}}{qS}$

C_D drag coefficient, $\frac{\text{Drag}}{qS}$

C_m pitching-moment coefficient, $\frac{\text{Pitching moment}}{qS\bar{c}}$

C_l rolling-moment coefficient, $\frac{\text{Rolling moment}}{qSb}$

C_n yawing-moment coefficient, $\frac{\text{Yawing moment}}{qSb}$

C_Y side-force coefficient, $\frac{\text{Side force}}{qS}$

M free-stream Mach number

L/D lift-drag ratio, C_L/C_D

q free-stream dynamic pressure, lb/sq ft

S wing area, sq ft

$\bar{c}$ wing mean aerodynamic chord, ft

b wing span, ft

α angle of attack of wing-chord plane referred to baseline, deg

β angle of sideslip, deg

i_t angle of incidence of horizontal tail, referred to wing-chord plane when wing incidence is at 2.5°, deg

C_{L_α} lift-curve slope, measured at zero lift, $\frac{\partial C_L}{\partial \alpha}$, per deg

$C_{m_{C_L}}$ pitching-moment-curve slope, $\frac{\partial C_m}{\partial C_L}$ $\left(C_m \approx 0\right)$

$C_{m_{i_t}}$ rate of change of pitching-moment coefficient with tail incidence, $\frac{\partial C_m}{\partial i_t}$, per deg

C_{l_β} rate of change of rolling-moment coefficient with sideslip angle, $\frac{\partial C_l}{\partial \beta}$, per deg

C_{n_β} rate of change of yawing-moment coefficient with sideslip angle, $\frac{\partial C_n}{\partial \beta}$, per deg

C_{Y_β} rate of change of side-force coefficient with sideslip angle, $\frac{\partial C_Y}{\partial \beta}$, per deg

Subscripts:

min	minimum
max	maximum

Hydrodynamic

All hydrodynamic data presented have been converted to full-size values. The center of gravity of the model was located at 25 percent of the mean aerodynamic chord in the wing-chord plane and at 26.6 percent of the mean aerodynamic chord above the hull baseline.

b	hull beam, ft
C_{Δ_0}	gross-load coefficient, $\frac{\Delta_0}{wb^3}$
w	specific weight of water (63.3 lb/cu ft for these tests)
Δ_0	gross load, lb
τ	trim, angle between forebody keel at step and horizontal, deg
δ_e	elevator deflection referred to stabilizer chord, positive when trailing edge is down, deg
δ_s	stabilizer deflection referred to hull baseline, positive when trailing edge is down, deg
r	rise, vertical distance of center of gravity from its position at zero trim with trailing edge of step touching free-water surface, positive upward, ft unless otherwise specified
R	total resistance (including model air drag), lb
V	speed, fps

DESCRIPTION OF MODELS

A general arrangement of the configuration is shown in figure 2 and the lines of the hull-type fuselage are shown in figure 3. The pertinent characteristics and dimensions of the full-size aircraft are given in table I.

Wind-Tunnel Model

Photographs of the $\frac{1}{42.5}$-size basic configuration used for the wind-tunnel tests are presented in figure 4. The wing, the pylon-mounted nacelles, and the tail surfaces were made of stainless steel. The tail-mounted nacelles were constructed of plastic and fiber-glass cloth. The hull was made of plastic and fiber-glass cloth over a steel core with the rear portion cut off to allow for installation of the support sting (fig. 4). For the modified configurations, the wingtip floats and the vertical chine strips were made of plastic; whereas the step fairing was made of wood.

Tank Model

Photographs of the $\frac{1}{20}$-size dynamic model used for the hydrodynamic investigation are presented in figure 5. The fuselage was of plastic-impregnated fiber glass. The wing and tail surfaces, which were constructed of balsa covered with plastic, were the same as those used for the hydro-ski configuration of reference 1. Leading-edge slats were used to prevent premature wing stall that usually is encountered at low Reynolds numbers in the hydrodynamic tests in which velocity is determined on the basis of Froude number correlation.

The horizontal stabilizer and elevators could be fixed at angles from 5° to -15° and 20° to -20°, respectively. The wing incidence could be fixed at angles of $2\frac{1}{2}^\circ$, $7\frac{1}{2}^\circ$, 10°, and $12\frac{1}{2}^\circ$ relative to the forebody keel.

Vertical chine strips of $\frac{1}{16}$-inch-thick fiber glass and plastic were located along the forebody chine from a position 4.4 inches ahead of the step centroid to the bow of the model as shown as full scale in figure 3. The strips had a depth of 0.25 inch at the rear and were faired to zero depth at the bow. Also shown in this drawing are the afterbody flow deflectors, which were rectangular in plan form (3 by 3 inches) with the trailing edge 9 inches behind the point of the step. The deflectors were constructed of 0.0079-inch-thick spring bronze with the leading edge rigidly attached to the model. With no load, the trailing edge deflected downward approximately 25°. A load of 0.27 pound (1 percent of the gross weight) applied at the trailing edge compressed the deflectors against the hull bottom.

Thrust for the two forward engines was simulated by cold-air jets as in the hydrodynamic tests of reference 1. Air was supplied to the model by $\frac{3}{8}$-inch-diameter flexible plastic tubing from a high-pressure supply on the towing carriage.

Electric contacts were located in the hull keel at the bow, step, and sternpost to indicate when these portions of the model were in contact with the water. These electric contacts also were used to release the trim brake during the landing tests.

APPARATUS AND PROCEDURE

Aerodynamic

Apparatus.- The aerodynamic investigation was conducted in the Langley 8-foot transonic pressure tunnel at Mach numbers from 0.60 to 1.42 and in the Langley Unitary Plan wind tunnel at Mach numbers from 1.57 to 2.20.

The transonic facility has a slotted test section in which the Mach number can be varied continuously up to a Mach number of 1.2. Fairings, which are described in reference 8, were used to enclose the slots of the test section to produce a Mach number of 1.42. All data presented from this tunnel are essentially free of wall-reflected disturbances. The accuracy of the drag data at a Mach number of 1.15, however, appears to be questionable, and it is believed that the accuracy may be influenced by disturbances coming upstream through the sting-support boundary layer. The present investigation was conducted at stagnation pressures of either 0.5 or 1.0 atmosphere and at such a dewpoint as to make the airflow free of condensation shocks.

The supersonic tests were conducted in the low Mach number test section of the Langley Unitary Plan wind tunnel, which is a variable-pressure, continuous-flow wind tunnel. The nozzle leading to the test section is of the asymmetric, sliding-block type, which permits a continuous variation of Mach number from about 1.5 to 2.9. Both stagnation temperature and stagnation pressure can be controlled independently. For this investigation most of the tests were performed at a stagnation pressure of 0.68 atmosphere and at such a dewpoint as to avoid condensation shocks.

The variation of Reynolds number with Mach number for different values of stagnation pressure is presented in figure 6.

Measurements.- The models were mounted on a six-component strain-gage balance and were sting-supported in the usual manner as shown in figure 4. The force and moment results have been adjusted to the condition of free-stream static pressure on the base of the model. In addition, the internal drag has been subtracted from the drag data to give a net external drag. The internal-drag values used are given in reference 1.

The model angle of attack was varied from about -4° to a maximum of approximately 17.5°. Characteristics of the model in sideslip were obtained at angles of sideslip of 0°, 2°, and 5° in the 8-foot transonic pressure tunnel and at sideslip angles of 0° and 4° in the Unitary Plan wind tunnel. The angles of attack and of sideslip have been corrected for balance and sting deflections and for stream-flow angularity.

Accuracy.- Based upon balance calibration and repeatability of data, it is estimated that the various measured quantities are accurate within the following limits:

	8-foot transonic pressure tunnel	Unitary Plan wind tunnel
Mach number	±0.005	±0.015
α, deg	±0.1	±0.1
β, deg	±0.1	±0.1
C_L	±0.03	±0.01
C_D	±0.002	±0.001
C_m	±0.010	±0.002
C_l	±0.0013	±0.0005
C_n	±0.0038	±0.0005
C_Y	±0.03	±0.0025

Procedure.- Aerodynamic tests of the basic model configuration with a wing incidence of 2.5°, a horizontal tail incidence of -2.5°, and natural transition were made at transonic and supersonic speeds. Additional tests also were made with various horizontal-tail-incidence angles and with modifications to the basic model consisting of the addition of wingtip floats, rounded chines, vertical chine strips or a step fairing. The investigation was extended at the higher supersonic speeds to include tests of configurations having combinations of these model modifications.

The effects due to fixed transition also were investigated. The transition was fixed by means of No. 120 carborundum grains attached in

a 0.1-inch-wide strip at 10 percent of the local chord behind the leading edge and on upper and lower surfaces of all airfoils. Similar strips were attached at approximately 5 percent of the respective lengths behind the upstream end of the hull, the pylon-mounted nacelles, and the tail-mounted nacelles.

A summary of the configurations tested and the test conditions is presented in table II.

Hydrodynamic

Apparatus.- The hydrodynamic investigation was made in Langley tank no. 1, which is described in reference 9. The apparatus and procedure used to investigate the hydrodynamic characteristics of dynamic models were similar to those described in reference 10. A photograph of the model and the towing apparatus is presented in figure 7.

Measurements.- The model was mounted from a vertical towing staff, and the horizontal force was measured by a mechanical-optical dynamometer mounted on the towing carriage. Air tares of the towing gear were measured by using the same dynamometer. Trim and rise of the model were measured by means of resistance slide wires and were recorded against time on an oscillograph. Carriage speed and distance along the tank also were recorded. Motion pictures and observations were made of the spray and model motions.

Accuracy.- The accuracy of the measurements as determined by static calibrations is believed to be within the following limits:

Resistance, lb	±0.1
Trim, deg	±0.1
Speed, fps	±0.1
Rise, in.	±0.1

Procedure.- The hydrodynamic tests were made with a wing incidence of 10°, a model weight corresponding to 225,000 pounds, and a center-of-gravity location of 0.25$\bar{c}$. Some resistance tests were made with a wing incidence of $12\frac{1}{2}°$.

The resistance (power off) of the complete model was determined during a series of constant-speed tests for each of a range of fixed-stabilizer deflections. The air tare of the towing staff and power leads was subtracted from the measured horizontal force to obtain the net resistance, which included the air drag of the model. The thrust moment of the four engines was simulated by a weight moment, and the

load was corrected for the vertical component of the thrust by a reduction in the gross weight. During the tests with power, the thrust of the forward engines was simulated by cold-air jets. The thrust moment and lift force of the rear engines were simulated by weight forces as before. Spray observations and photographs also were obtained during the constant-speed runs.

The trim limits of stability were determined during constant-speed runs using stabilizer control. The trim of the model was adjusted by using the stabilizer until porpoising was noted or until the maximum or minimum stabilizer deflection was obtained. The trim at which porpoising was first observed was taken as the limit of stability.

Take-offs were made with a range of fixed-stabilizer deflections at a rate of acceleration of 5 ft/sec^2 based on an average value of excess thrust as determined from the constant-speed resistance tests.

Landings were made for a range of landing trims. The attitude of the model was fixed until contact with the water was made. Upon contact with the water, the electrical trim brake was released by the short-circuiting of contacts in the model hull.

RESULTS AND DISCUSSION

An index of the figures presenting the aerodynamic results is given in table III and the hydrodynamic results in table IV.

Aerodynamic Characteristics

All the configurations tested exhibit linear lift characteristics up to a lift coefficient of approximately 0.5. (See, for example, figs. 8 to 13.)

In general, the lift-curve slopes for the various model configurations are similar and follow the usual trend for the speed range presented (fig. 14). The effects on C_{L_α} due to modifications to the basic model are insignificant.

Reference 1 presents data for a water-based hydro-ski aircraft which is identical to the basic model of the present investigation with the exception of the fuselage. A comparison of the minimum drag coefficients of these two aircraft (fig. 15(a)) indicates that the transonic drag rises are abrupt and occur near $M = 0.94$. The hull-type

fuselage of the present investigation has the greater $C_{D,min}$ up to a Mach number of about 1.4, but near the design maximum Mach number of 2.0 the $C_{D,min}$ of the basic model of the present investigation is lower than that of the hydro-ski aircraft. The modifications to the basic model tend, in general, to reduce $C_{D,min}$ at subsonic speeds but to increase $C_{D,min}$ at the higher supersonic speeds (figs. 15(b) and 15(c)).

A comparison of the maximum lift-drag ratio of the basic model with that of the hydro-ski aircraft of reference 1 (fig. 16(a)) shows that the maximum lift-drag ratio of the basic model is considerably lower at the low speeds but is essentially the same near the design maximum Mach number of 2.0. The performance of the basic model is improved at the lower speeds, however, by the various modifications investigated, but the high-speed performance is penalized as shown in figures 16(b) and 16(c).

No pitch-up tendencies were observed throughout the lift coefficient and Mach number ranges of this investigation for all configurations tested. (See, for example, figs. 8 to 10.)

For all configurations, a large rearward movement of the aerodynamic center is noted in the transonic speed range (fig. 17). For the basic model, this rearward movement of the aerodynamic-center location is about 17 percent of the mean aerodynamic chord. The modifications to the basic model have a negligible effect on the stability level (figs. 17(b) and 17(c)).

Horizontal-tail effectiveness (fig. 18) is maintained at all Mach numbers of this investigation.

All configurations tested are stable laterally and directionally except at $M = 2.20$ for angles of attack greater than 13°, where directional instability is indicated (figs. 19 to 23).

Hydrodynamics

Spray characteristics.- Photographs of the spray over the speed range to take-off at the normal gross load are shown in figure 24.

The bow spray blister was effectively thrown clear of the forebody by the vertical chine strips. Without these strips, flow clung to and flowed up the fuselage sides and also heavily wetted the wing nacelles.

With the chine strips, the wing engine inlets were clear of spray at all speeds. Only the rear portion of the nacelle was struck by spray and then only for a short speed range near 50 knots (fig. 24(e)). The

underside of the wing was wetted by forebody chine spray over the speed range from 80 to 110 knots (fig. 24(f)).

In figure 24(e) it may be noted that the step has started to ventilate and that only the rear half of the afterbody is wetted. In the speed range from 80 to 150 knots (figs. 24(f), 24(g), and 24(h)) the afterbody was running clear in the wide, deep wake from the forebody with only the stern touching lightly. At a speed near take-off, the flow reattached to the afterbody (fig. 24(i)). This reattachment appeared as the forebody wake narrowed and only the center portion of the pointed main step was wetted. The high take-off speed provided a high velocity water flow which, for restricted clearances, produced a low pressure on the long afterbody sides leading to the observed sudden attachment of flow to the afterbody bottom. This attached flow appeared as foam in the wake behind the model (fig. 24(i)).

Flow deflectors located behind the step on the afterbody bottom were quite effective in reducing the afterbody wetting. The deflectors turned the flow originating from the forebody, provided greater clearances between the forebody wake and the afterbody bottom and sides, and thus prevented reattachment.

Airflow to simulate the jet exhaust of the forward engine dispersed the chine blister in the region of the jet exhaust and accelerated the flow along the afterbody sides. For speeds greater than approximately 100 knots, power had no significant effect upon the spray.

The engine inlets and horizontal tail were clear of spray throughout the speed range for all conditions investigated.

Resistance.- The effect of variation in the gross load on the resistance, trim, and rise at speeds up through the hump speed is shown in figure 25. Data are presented for 78, 100, and 110 percent of the normal gross load.

At low speeds, an increase in load increased the draft, but had little effect on the static trim. Variation in load appeared to have little effect on the speed at which hump resistance occurred. The minimum gross-load—resistance ratio was nearly the same for the gross loads presented and varied from 3.8 for the overload to 4.0 for the underload condition.

The variation in resistance, trim, and rise with stabilizer and elevator settings at the normal gross load is presented in figure 26. Below a speed of 100 knots, the tail settings had little effect upon the trim.

The resistance increased abruptly for all tail settings at speeds near take-off. As may be noted for the stabilizer setting of -5° corresponding to the condition for the flow pictures of figure 24, the most pronounced increase in resistance occurred between speeds of 144 and 163 knots. As explained in the section on spray, a reattachment of afterbody flow occurred in this speed region. With the flow attached to the afterbody, the trim remained high and the elevator effectiveness was reduced. The resistance did not decrease until the step left the water. For some conditions the afterbody continued to plane on the water although the forebody was clear of the water. In this condition a large reduction in resistance below the resistance with the forebody planing was noted. Increased resistance at high speed has been noted in other high-speed hull-type configurations with long afterbodies (refs. 4 and 6). The take-off speeds were lower for the reference configurations and the resulting increase in resistance at high speeds did not present as serious a problem.

An increase in the wing incidence of $2\frac{1}{2}^{\circ}$ did not decrease the take-off speed sufficiently to obtain an appreciable reduction in the high-speed resistance (fig. 27).

The total resistance, trim, and rise are presented in figure 28 for the model with afterbody flow deflectors and several stabilizer and elevator settings. With the flow deflectors on, small undamped oscillations in trim and rise are shown in the figure by cross hatching. These results are compared with those of figure 25 for the same tail settings without afterbody flow deflectors. With the stabilizer set at -7.5°, there was little change in the trim caused by the deflector, but a large reduction in resistance was obtained. For the -5° stabilizer setting, a definite reduction in trim resulted with the flow deflector, indicating a complete removal of the afterbody flow which is reflected in the large reduction in resistance (46 percent at 176 knots).

The resistance, trim, and rise of the hull-type model are compared in figure 29 with those of the hydro-ski configuration of reference 1. Data are presented for the hull model with and without afterbody flow deflectors. In the displacement speed region, the drag of the submerged hydro-ski produces a resistance increment over that of the hull. At high speed the excellent clearances provided by the hydro-ski result in low resistance. With the afterbody flow deflectors, the hull resistance at high speed is nearly the same as that of the hydro-ski configuration.

The flow deflectors reduced the take-off time and distance of the hull configuration from 42 seconds and 7,000 feet to 30 seconds and 5,000 feet, which are nearly the same as for the hydro-ski configuration.

Trim limits.- The trim limits of stability are presented in figure 30. The lower trim limit was similar to that encountered for many seaplane hulls in that it was a function of the forebody only. Upper-limit instability at the normal position of the center of gravity was encountered at speeds above 150 knots and then was only obtained by inducing an oscillation through a violent deflection of the stabilizer. In this speed region the trim motions appeared to be highly damped by the attached flow on the afterbody. At speeds and trims at which the flow was not attached to the afterbody, the model had the same low aerodynamic damping noted for the hydro-ski configuration of reference 1, and some small-amplitude nondivergent oscillations were encountered. These oscillations did not appear to be significant but made it difficult to determine the point of entering the lower limit.

Take-off stability.- Variations in trim during accelerated take-offs at the normal gross weight for a range of stabilizer deflections are shown in figure 31. At speeds of less than 95 knots, trim was not affected by the tail setting. For all except the -2° and -3° stabilizer settings, the model trim was high in the high-speed region, and the flow was attached to the afterbody. For the -2° and -3° settings with no power (fig. 31(a)), the model trimmed below the lower trim limit and porpoising resulted. At the same tail settings, -2° and -3°, with power on (fig. 31(b)), the model also porpoised at high speeds but at somewhat greater average trim. Power, therefore, appears to have only a minor effect on take-off stability, probably because the jet exhaust has little effect on the flow on the afterbody at high speeds. The period of the trim oscillation was sufficiently long and the tail effectiveness was such that a pilot probably could reduce the trim motions to permit relatively smooth take-offs to be made. Take-offs at these tail deflections would be desirable because the afterbody is clear of the attached flow at high speeds and the total resistance is reduced.

Landing stability.- Smooth-water landings were made over a range of landing trims from 5.8° to 14.7° at the normal gross load of 225,000 pounds. The variations in trim and rise for landing angles of 5.8° and 14.7° are presented in figure 32. The landings were stable, although some nondivergent oscillations in trim and rise occurred during all the landing runouts. The trim during the landing runout remained above the lower trim limit of stability.

CONCLUDING REMARKS

The transonic drag rise of all configurations investigated was abrupt and occurred near a Mach number of 0.94.

Near the design maximum Mach number of 2.0, the performance of the basic model as shown by the maximum lift-drag ratio was essentially the same as a hydro-ski version of the model. The various modifications investigated tended to improve the low-speed performance but to penalize the high-speed performance.

All configurations tested were stable longitudinally, laterally, and directionally except at a Mach number of 2.20 for angles of attack greater than 13°, where all configurations indicated some directional instability. The maximum variation of the longitudinal stability over the speed range corresponds to a rearward movement of the aerodynamic-center location of about 17 percent of the mean aerodynamic chord for the basic configuration.

Excess thrust was available for take-off throughout the speed range but acceleration was reduced by high resistance near take-off speed. The time and distance for a stable take-off were approximately 42 seconds and 7,000 feet, respectively. Afterbody flow deflectors reduced the resistance at high speed by approximately 46 percent and reduced the take-off time and distance to 30 seconds and 5,000 feet, respectively. With afterbody flow deflectors, the take-off time and distance were approximately the same as those of the hydro-ski version.

Satisfactory take-offs could be made over a range of fixed stabilizer settings, although some nondivergent oscillations in trim and rise were noted. Landings were acceptable over the range of landing trims investigated.

The engine inlets and the horizontal tail were free from spray for all conditions investigated.

Vertical chine strips were required on the forebody for spray control. Power appeared to have only minor effect on spray or longitudinal stability during take-off.

Langley Research Center,
National Aeronautics and Space Administration,
Langley Field, Va., December 2, 1959.

REFERENCES

1. Petynia, William W., Hasson, Dennis F., and Spooner, Stanley H.: Aerodynamic and Hydrodynamic Characteristics of a Proposed Supersonic Multijet Water-Based Hydro-Ski Aircraft With a Variable-Incidence Wing. NACA RM L57G05, 1957.

2. Petynia, William W., Croom, Delwin R., and Davenport, Edwin E.: Low-Speed Aerodynamic and Hydrodynamic Characteristics of a Proposed Supersonic Multijet Water-Based Hydro-Ski Aircraft With Upward-Rotating Engines. NASA MEMO 10-13-58L, 1958.

3. Blanchard, Ulysse J.: Hydrodynamic Investigation of a Model of a Supersonic Multijet Water-Based Aircraft With Engines Exhausting From the Step. NACA RM L57F20, 1957.

4. Bielat, Ralph P., Coffee, Claude W., Jr., and Petynia, William W.: Aerodynamic and Hydrodynamic Characteristics of a Deck-Inlet Multijet Water-Based-Aircraft Configuration Designed for Supersonic Flight. NACA RM L56H01, 1956.

5. Morse, Archibald E., Jr., Woodward, David R., and Blanchard, Ulysse J.: An Investigation of the Hydrodynamic Characteristics of a Dynamic Model of a Transonic Seaplane Design Having a Planing-Tail Hull. NACA RM L56C28a, 1956.

6. Olson, Roland E., and Bielat, Ralph P.: An Aerodynamic and Hydrodynamic Investigation of Two Multijet Water-Based Aircraft Having Low Transonic Drag Rise. NACA RM L55A11a, 1955.

7. McKann, Robert E., and Coffee, Claude W.: Limited Hydrodynamic Investigation of a 1/15-Size Model of a Modified Nose-Inlet Multijet Water-Based Aircraft. NACA RM L55J19, 1956.

8. Matthews, Clarence W.: An Investigation of the Adaptation of a Transonic Slotted Tunnel to Supersonic Operation by Enclosing the Slots With Fairings. NACA RM L55H15, 1955.

9. Truscott, Starr: The Enlarged N.A.C.A. Tank, and Some of Its Work. NACA TM 918, 1939.

10. Olson, Roland E., and Land, Norman S.: Methods Used in the NACA Tank for the Investigation of the Longitudinal-Stability Characteristics of Models of Flying Boats. NACA Rep. 753, 1943. (Supersedes NACA WR L-409.)

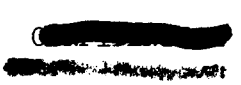

[redacted]

TABLE I

PERTINENT CHARACTERISTICS AND DIMENSIONS OF

THE FULL-SIZE WATER-BASED AIRPLANE

General:	
Gross weight, lb	225,000
Wing area, sq ft	1,500
Turbojet engines	4
Take-off thrust (with afterburners), lb	126,000
Take-off wing loading, lb/sq ft	150
Ratio of take-off thrust to weight	0.56
Wing:	
Span, ft	72.5
Wing area, sq ft	1,500
Airfoil section	NACA 65A003
Aspect ratio	3.5
Taper ratio	0.067
Sweepback (0.25$\bar{c}$), deg	28.9
Sweepback (0.80$\bar{c}$), deg	0
Dihedral, deg	0
Wing mean aerodynamic chord, ft	26.0
Incidence range, deg	2.5 to 12.5
Twist, deg	0
Horizontal tail:	
Span, ft	30.3
Airfoil section	NACA 65A004
Area, sq ft	230
Aspect ratio	4.0
Taper ratio	0
Sweepback (0.25$\bar{c}$), deg	36.9
Dihedral, deg	0
Tail arm, $\bar{c}/4$ of wing to $\bar{c}/4$ of horizontal tail, ft	52.0
Vertical tail:	
Airfoil	NACA 65A006
Aspect ratio	1.2
Sweepback (0.25$\bar{c}$), deg	41.2
Fuselage:	
Forebody length (F.P. to step centroid), ft	85.5
Afterbody length (step centroid to A.P.), ft	75.7
Length, overall, ft	161.2
Beam, maximum, ft	7.7
Height, maximum, ft	13.8
Step plan form	50° vee
Step depth at keel, ft	1.0
Step depth at keel, percent beam	13
Step depth at chine, ft	0.934
Dead rise at step, deg	35
Dead rise at A.P., deg	40
Afterbody keel angle, deg	5.0
Sternpost angle, deg	5.8
Center of gravity above fuselage baseline, ft	7.8
Ratio of forebody length to beam	11.1
Ratio of afterbody length to beam	9.8
Ratio of fuselage length to beam	20.9
Gross-load coefficient, C_{Δ_0}	7.8
Area curve:	
Maximum net cross-sectional area, sq ft	107
Maximum diameter of equivalent body, ft	11.7
Length, ft	161.2
Fineness ratio of equivalent body	13.8

[redacted]

TABLE II

SUMMARY OF AERODYNAMIC CONFIGURATIONS

Basic model with -	Figure number	Mach number	Horizontal tail incidence, i_t, deg	Type of transition	Stagnation pressure, atm
No addition	8	0.60 to 1.42	1.5, -2,5, -6.5, -12.5, off	Natural	0.5
No addition	8	1.57 to 2.20	1.5, -2.5, -12.5	Natural	0.68
No addition	11	0.60 to 1.42	-2.5	Fixed, natural	0.5
No addition	13	0.60 to 1.42	-2.5	Natural	1.0, 0.5
Vertical chine strips	9	0.60 to 1.42	-2.5	Natural	0.5
Vertical chine strips	9	1.57 to 2.20	-2.5	Natural	0.68
Step fairings	9	0.60 to 1.42	-2.5	Natural	0.5
Wingtip floats	9	0.60 to 1.42	-2.5	Natural	0.5
Wingtip floats	9	1.57 to 2.20	-2.5	Natural	0.68
Step fairings and wingtip floats	10	1.57 to 2.20	-2.5	Natural	0.68
Vertical chine strips, wingtip floats, and step fairings	10	1.57 to 2.20	-2.5	Natural	0.68
Round chines, step fairings, and wingtip floats	10	1.57 to 2.20	-2.5	Natural	0.68
Vertical chine strips, step fairings, and wingtip floats	12	1.57 and 1.77	-2.5	Fixed and natural	0.68

TABLE III

INDEX OF FIGURES PRESENTING AERODYNAMIC RESULTS

Figure	Type of plot	Configuration	Remarks
8	C_m, α, and C_D against C_L	Basic model with and without horizontal tail; $i_t = 1.5^\circ$, -2.5°, -6.5°, -12.5°	Effects of horizontal incidence
9	C_m, α, and C_D against C_L	Basic model with and without vertical chine strips, step fairing, and wingtip floats	Effects of model modification to basic model
10	C_m, α, and C_D against C_L	Basic model and basic model plus wingtip floats, step fairing, and with and without chine modification	Effects of chine modifications
11	C_m, α, and C_D against C_L	Basic model	Effects of transition
12	C_m, α, and C_D against C_L	Basic model plus wingtip floats, step fairings, and vertical chine strips	Effects of transition
13	C_m, α, and C_D against C_L	Basic model	Effects of Reynolds number
14	C_{L_α} against M	Basic model with and without horizontal tail, vertical chine strips, step fairing, and wingtip floats. Basic model plus wingtip floats, step fairing, and with and without chine modifications	Summary
15	$C_{D,min}$ against M	Model of ref. 1 and basic model; basic model with and without vertical chine strips, step fairing, and wingtip floats. Basic model plus wingtip floats, step fairing, and with and without chine modification	Summary
16	$(L/D)_{max}$ against M	Model of ref. 1 and basic model; basic model with and without vertical chine strips, step fairing, and wingtip floats. Basic model plus wingtip floats, step fairing, and with and without chine modification	Summary
17	$C_{m_{C_L}}$ against M	Model of ref. 1 and basic model; basic model with and without vertical chine strips, step fairing, and wingtip floats. Basic model plus wingtip floats, step fairing, and with and without chine modification	Summary
18	$C_{m_{i_t}}$ against M	Basic model	Summary
19	C_m, α, C_D, C_l, C_n, and C_Y against C_L	Basic model	Effects of sideslip
20	C_m, α, C_D, C_l, C_n, and C_Y against C_L	Basic model plus wingtip floats	Effects of sideslip
21	C_m, α, C_D, C_l, C_n, and C_Y against C_L	Basic model plus wingtip floats, step fairing, and vertical chine strips	Effects of sideslip
22	C_{l_β}, C_{n_β}, and C_{Y_β} against α	Basic model with and without wingtip floats. Basic model plus wingtip floats, step fairing, and vertical chine strips	Summary
23	C_{l_β}, C_{n_β}, and C_{Y_β} against M	Basic model with and without wingtip floats. Basic model plus wingtip floats, step fairing, and vertical chine strips	Summary

TABLE IV

INDEX OF FIGURES PRESENTING HYDRODYNAMIC RESULTS

Figure	Type of plot	Configuration	Remarks
25	R, τ, and r against V	Basic model, gross load = 175,000, 225,000, and 250,000 lb; $\delta_s = -2.5^\circ$; $\delta_e = -5^\circ$	Effect of gross load upon resistance, trim, and rise
26	R, τ, and r against V	Basic model, gross load = 225,000 lb; $\delta_s = -2.5^\circ$, -3.0°, -5.0°, -7.5°, and -10°	Effect of stabilizer setting upon resistance, trim, and rise
27	R, τ, and r against V	Basic model, gross load = 225,000 lb. Wing incidence = 10 and 12.5 degrees	Effect of wing incidence upon resistance, trim, and rise
28	R, τ, and r against V	Basic model, basic model with afterbody flow deflectors	Effect of afterbody flow deflectors upon resistance, trim, and rise
29	R, τ, and r against V	Basic model, basic model with afterbody flow deflectors and hydro-ski version	The resistance, trim, and rise of hull model compared with that obtained for similar hydro-ski version
30	τ against V	Basic model, gross load = 225,000 lb	Trim limits of stability
31	τ against V	Basic model with and without power; $\delta_s = -2^\circ$, -3°, -5°, -7.5°, and -10°	Variations in trim during smooth water take-offs with and without power
32	τ against V	Basic model; landing trim = 5.8° and 14.7°	Variations in trim and rise for two typical smooth-water landings

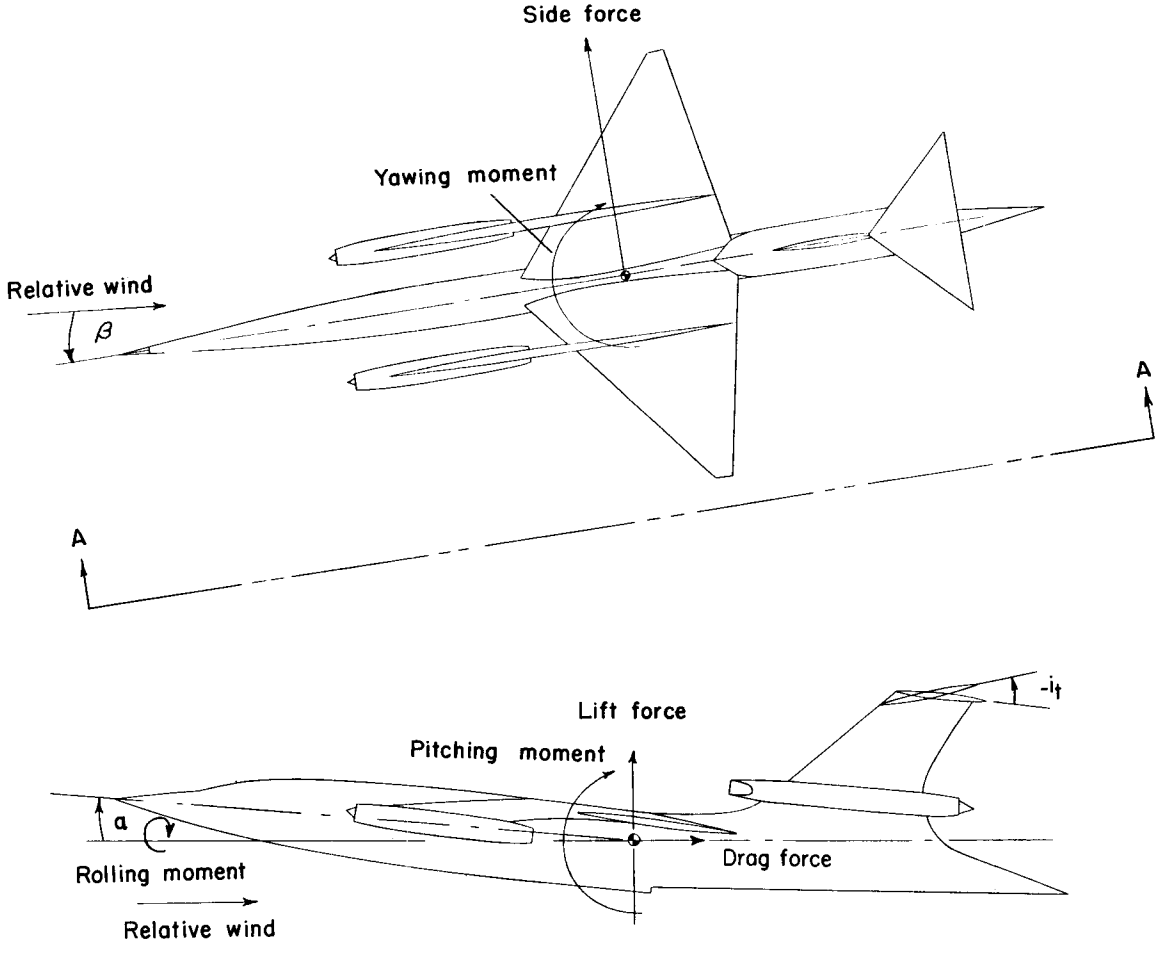

Figure 1.- Views of model showing positive direction of forces and moments.

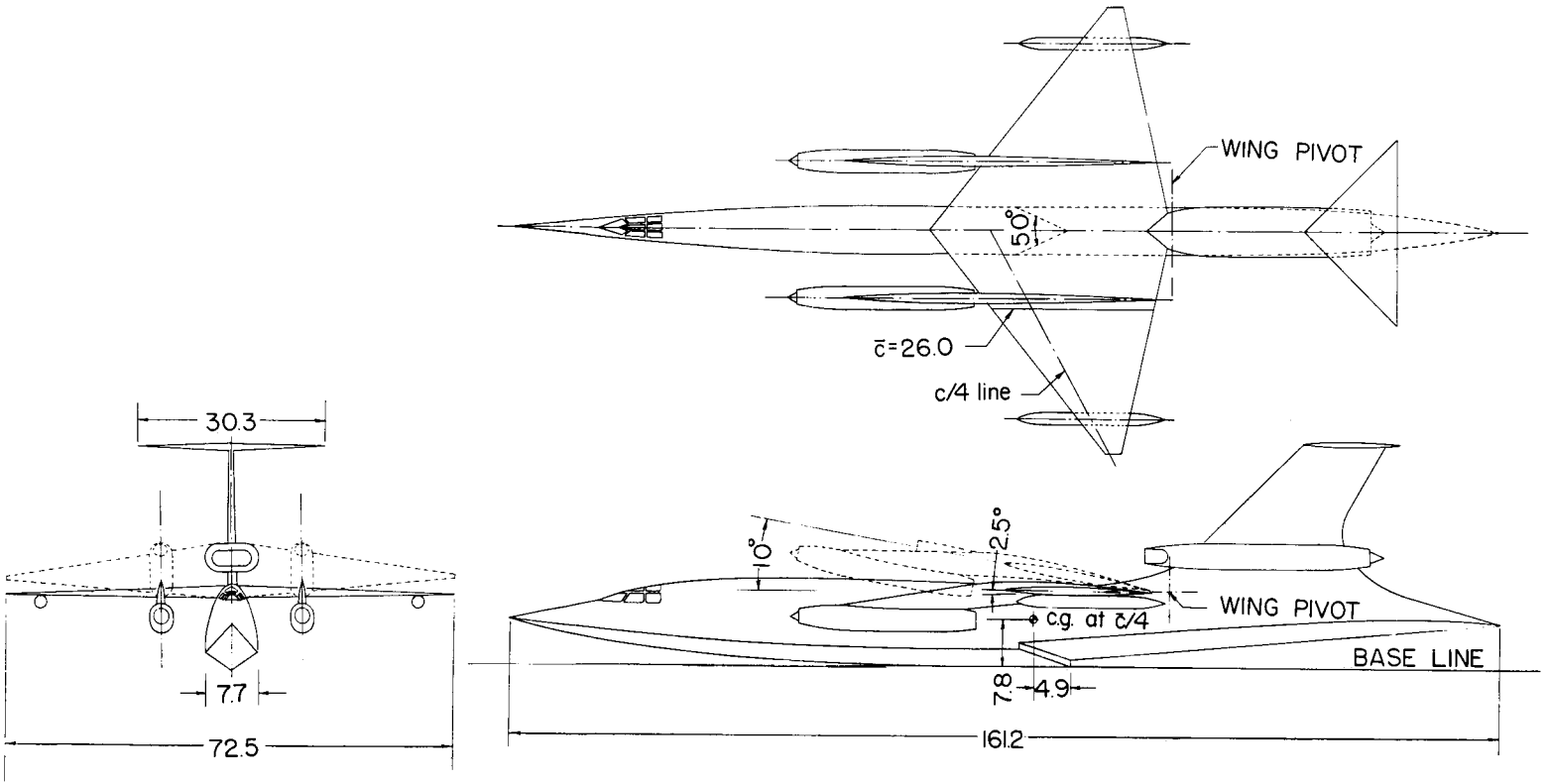

Figure 2.- General arrangement of configuration. All dimensions in feet unless otherwise noted.

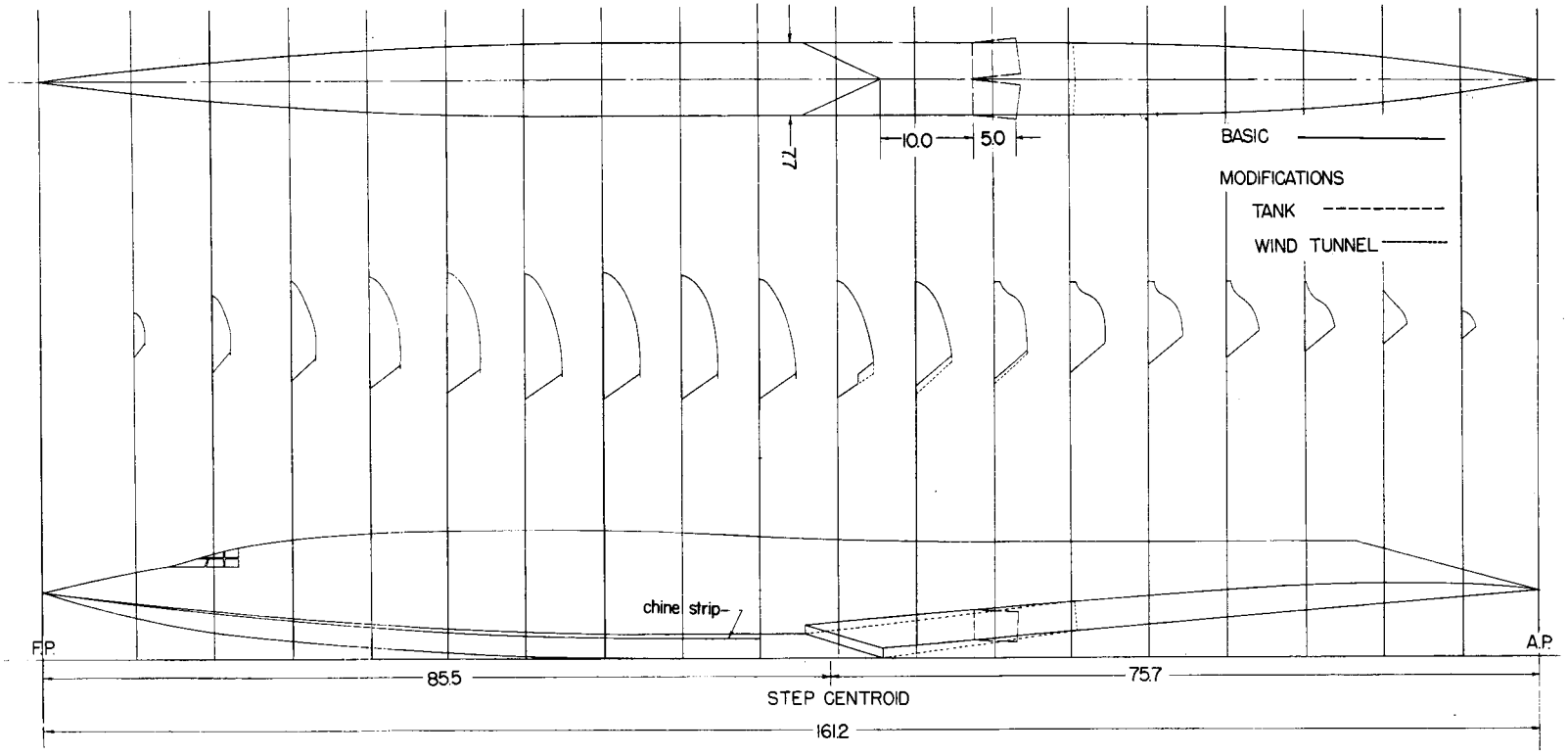

Figure 3.- Layout of hull-type fuselage lines.

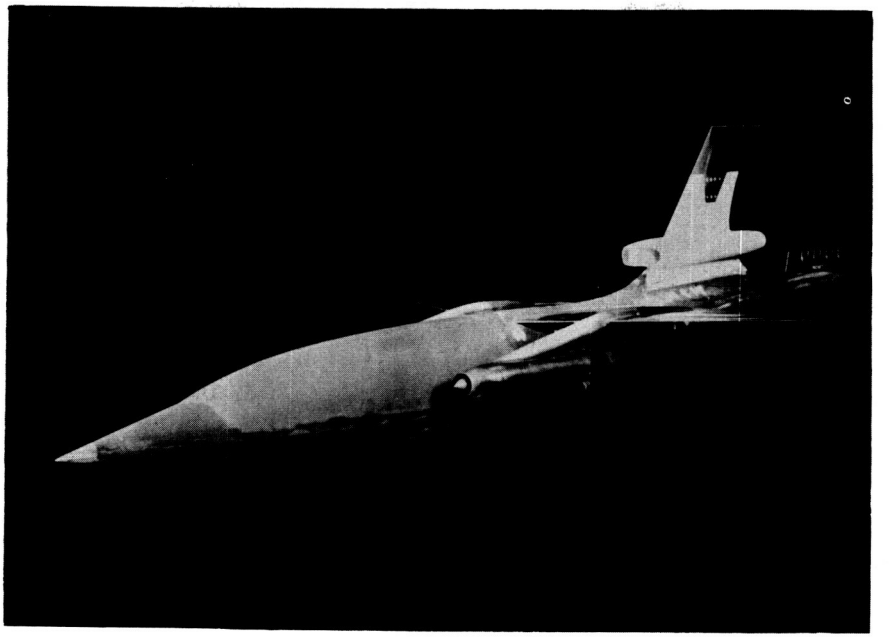

L-57-4178

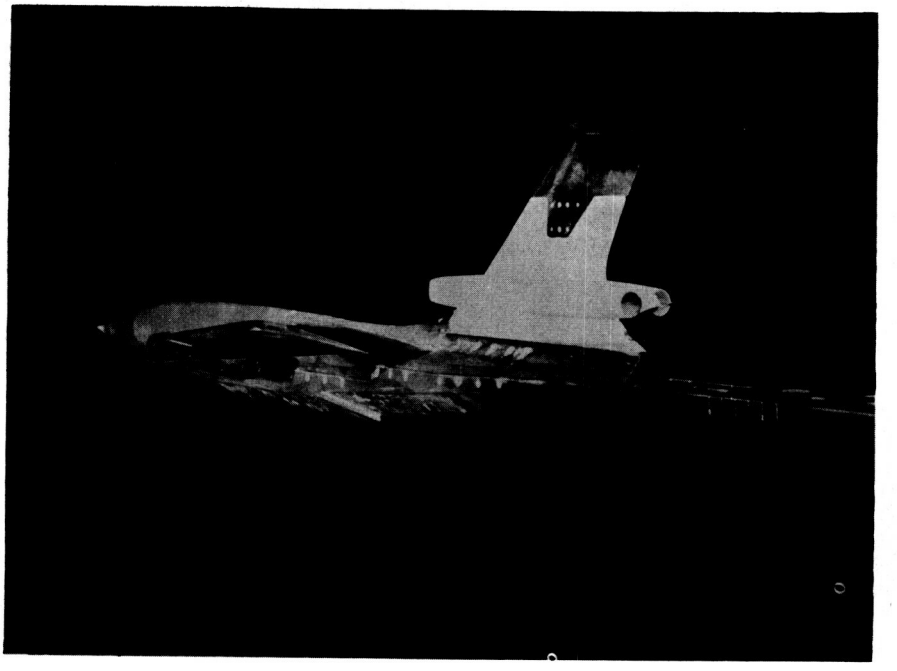

L-57-4179

Figure 4.- Photographs of $\frac{1}{42.5}$-size wind-tunnel model.

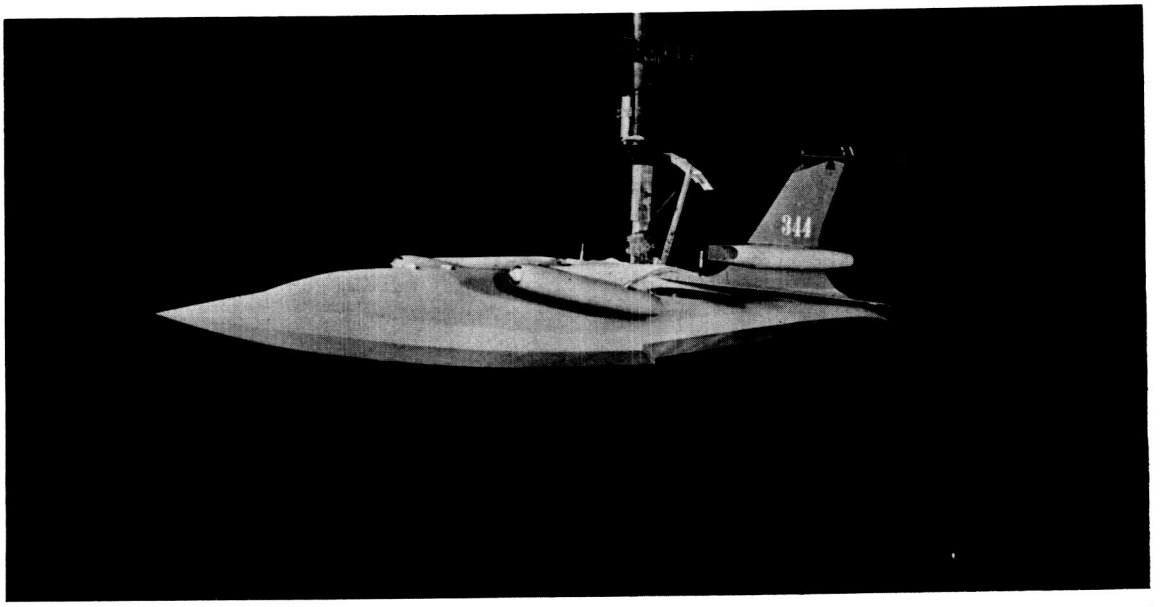

L-95313

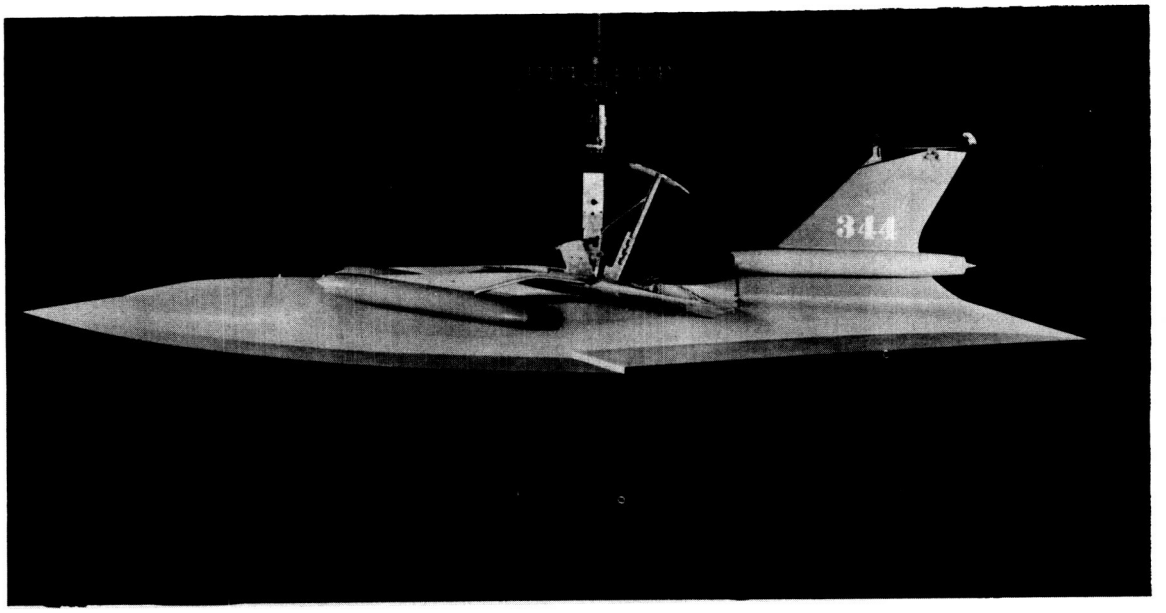

Figure 5.- Photographs of $\frac{1}{20}$-size tank model. L-95312

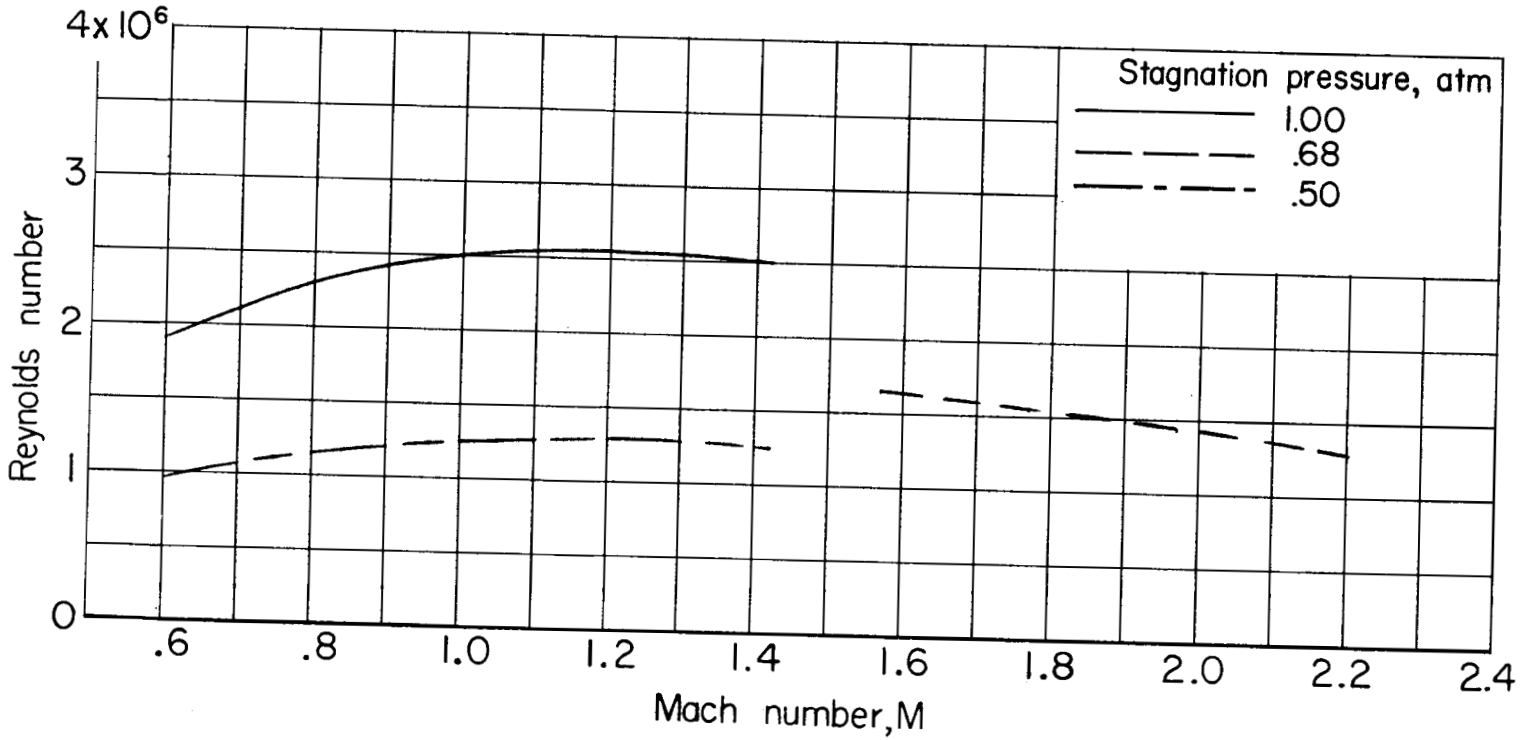

Figure 6.- Variation of Reynolds number based on $\bar{c}$ with Mach number.

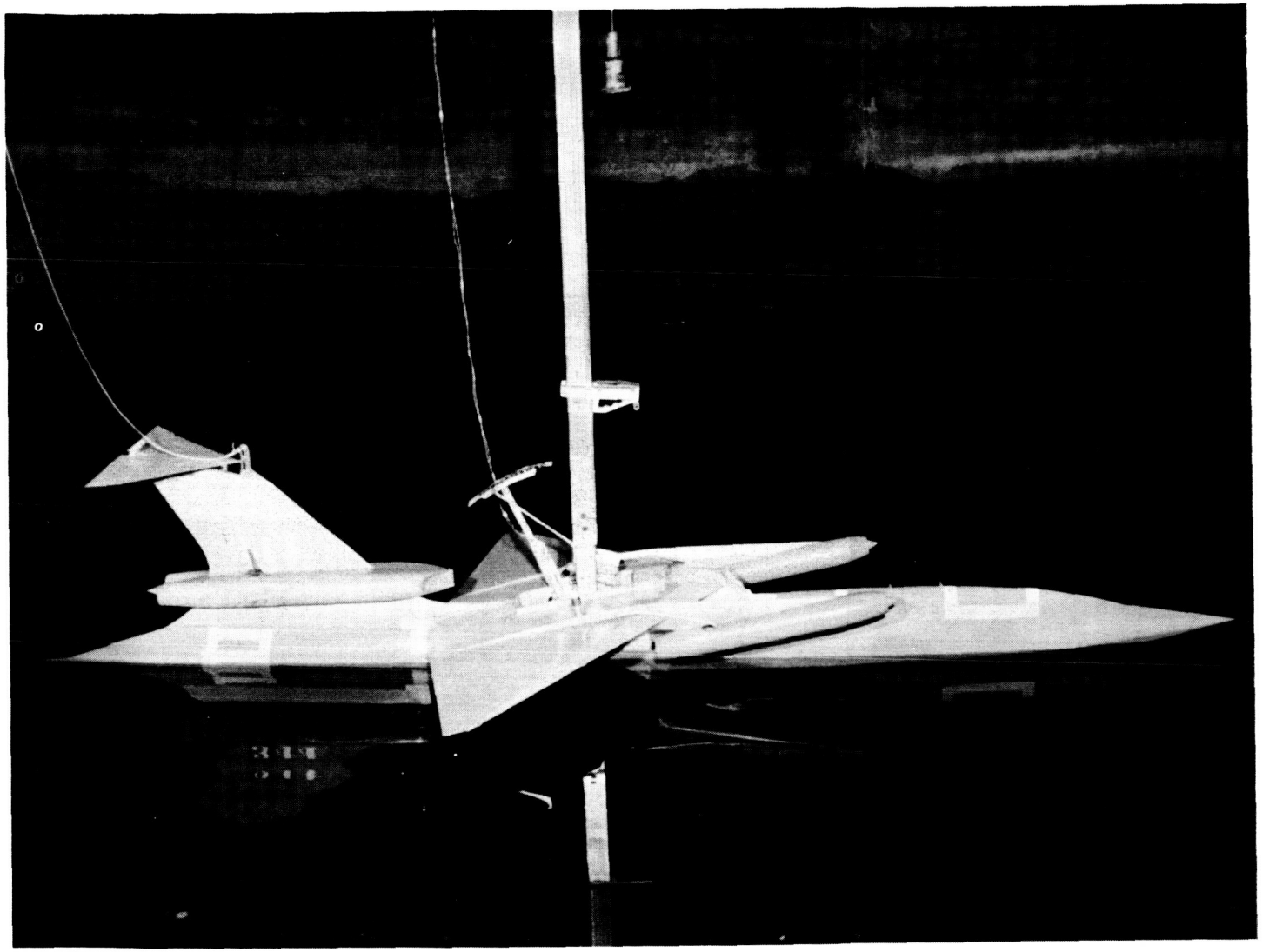

Figure 7.- Setup of model on towing gear. L-59-6499

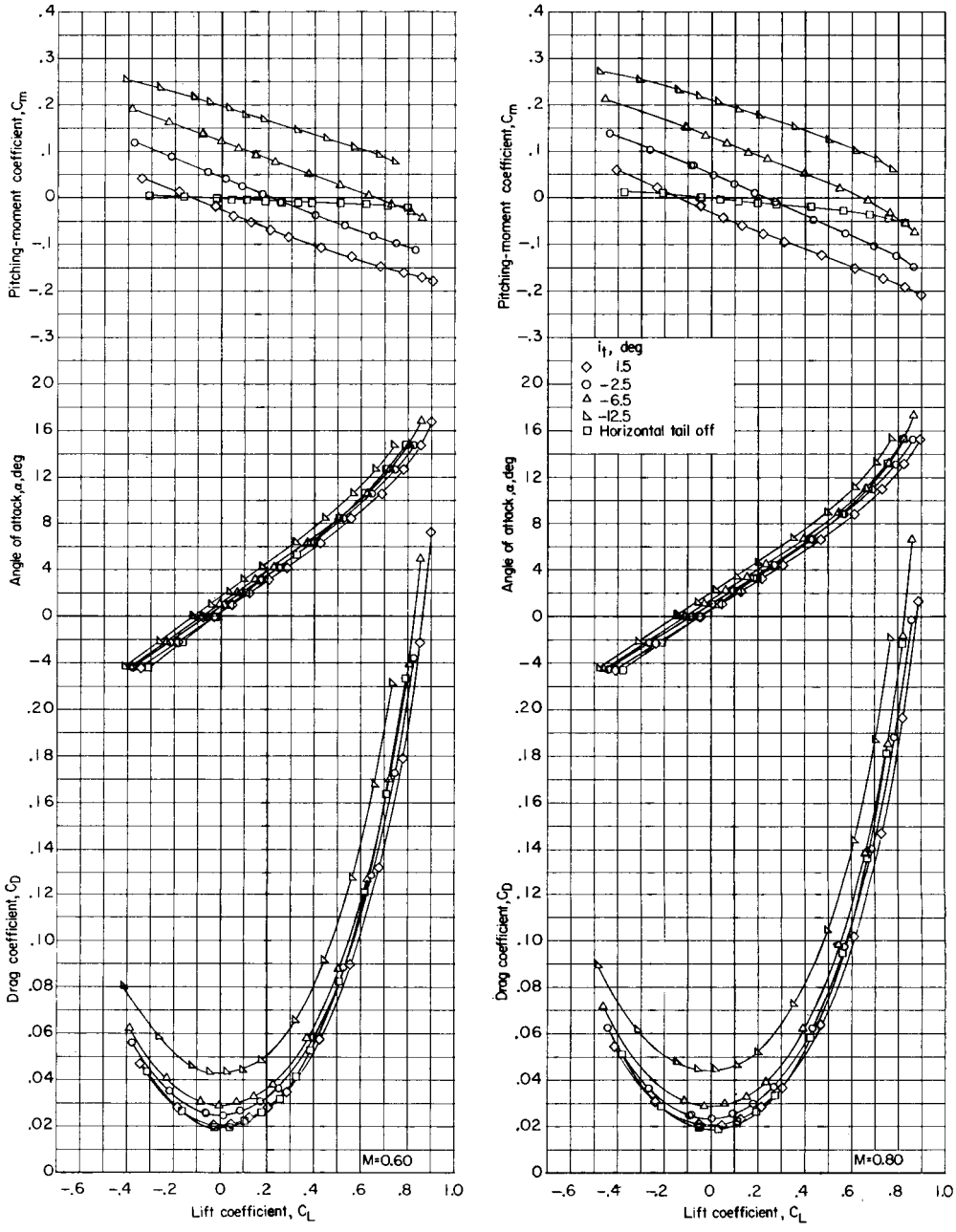

(a) M = 0.60 and 0.80; stagnation pressure, 0.5 atm.

Figure 8.- Effects of horizontal-stabilizer deflection on longitudinal aerodynamic characteristics of basic model with natural transition.

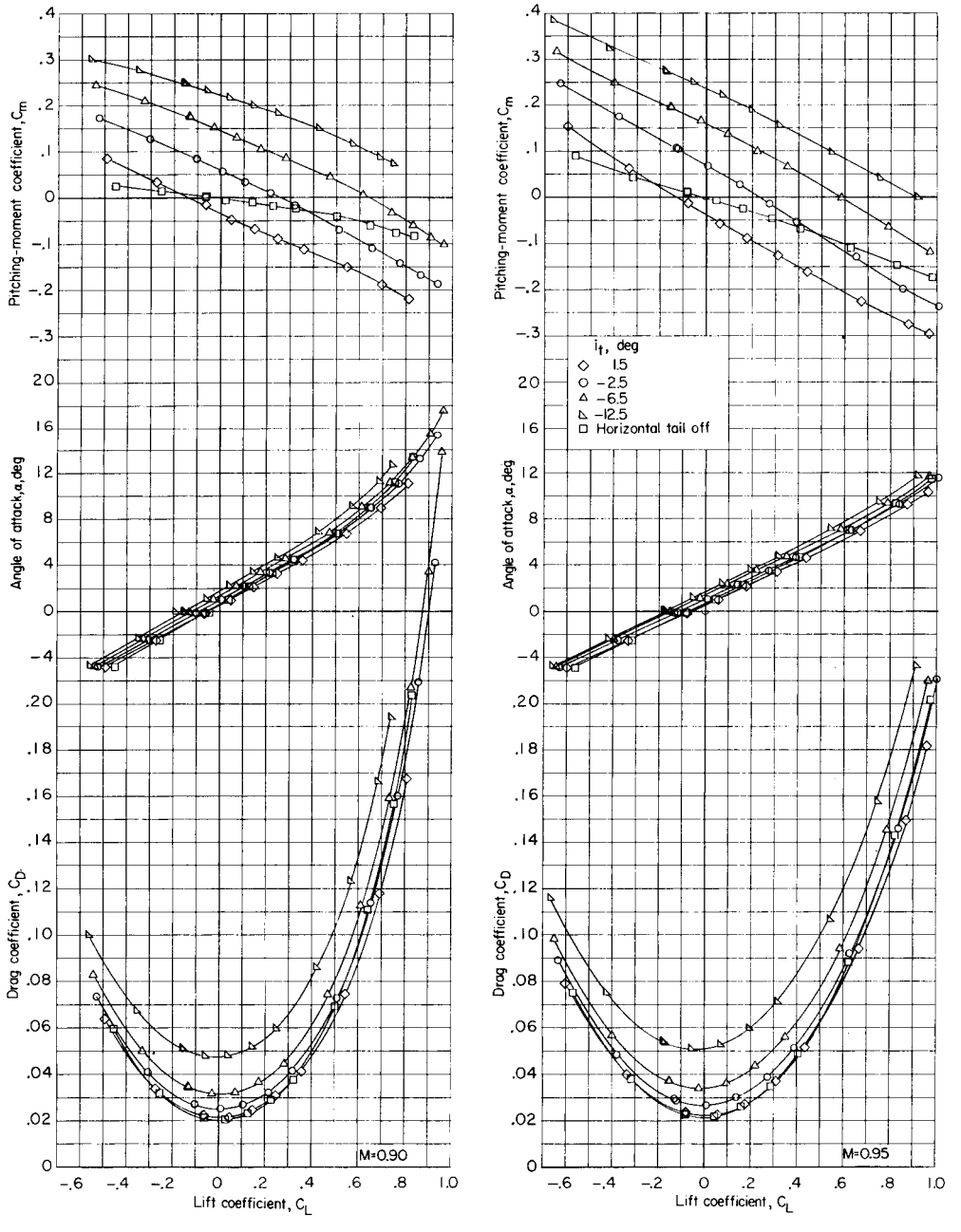

(b) M = 0.90 and 0.95; stagnation pressure, 0.5 atm.

Figure 8.- Continued.

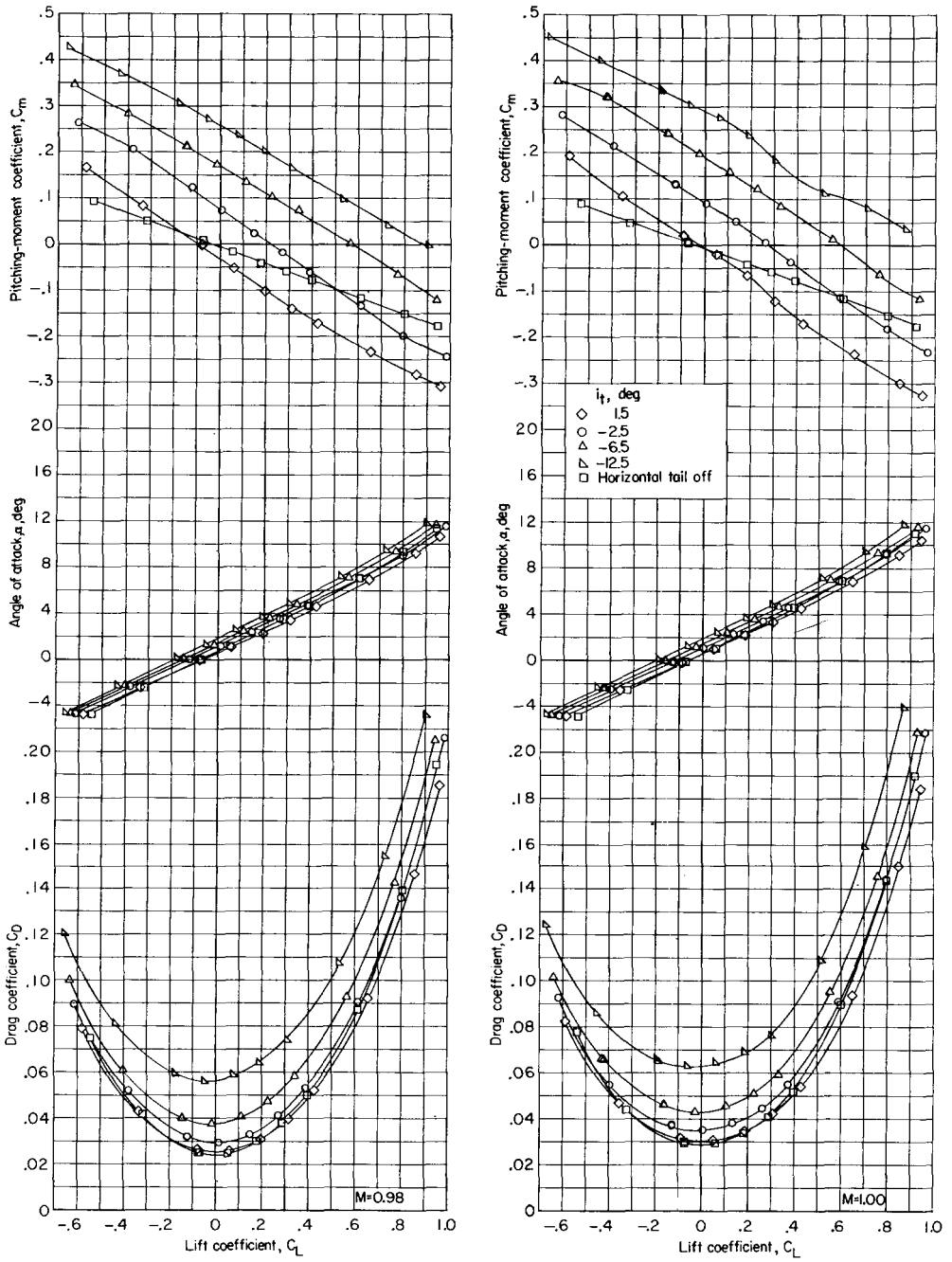

(c) M = 0.98 and 1.00; stagnation pressure, 0.5 atm.

Figure 8.- Continued.

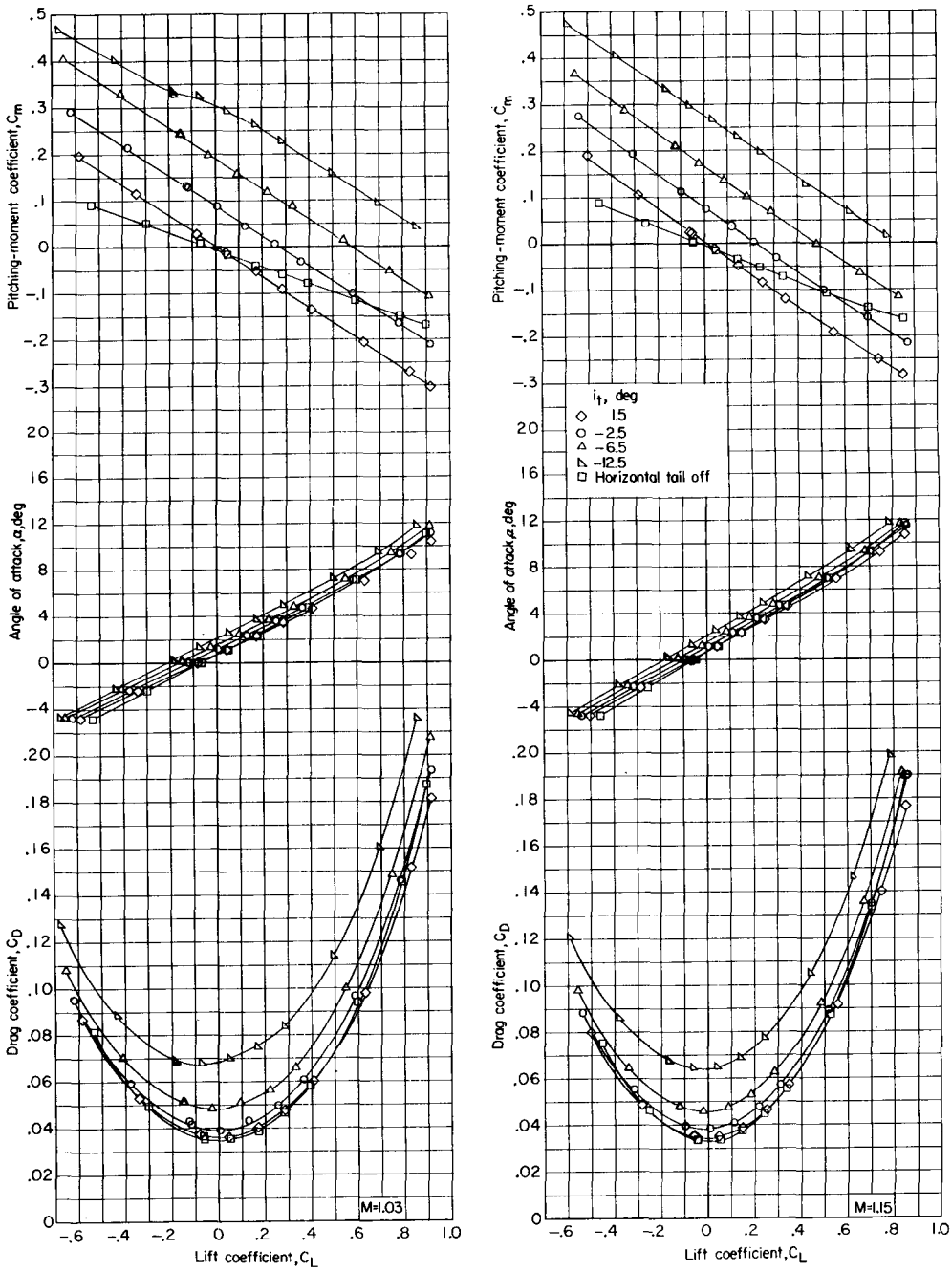

(d) M = 1.03 and 1.15; stagnation pressure, 0.5 atm.

Figure 8.- Continued.

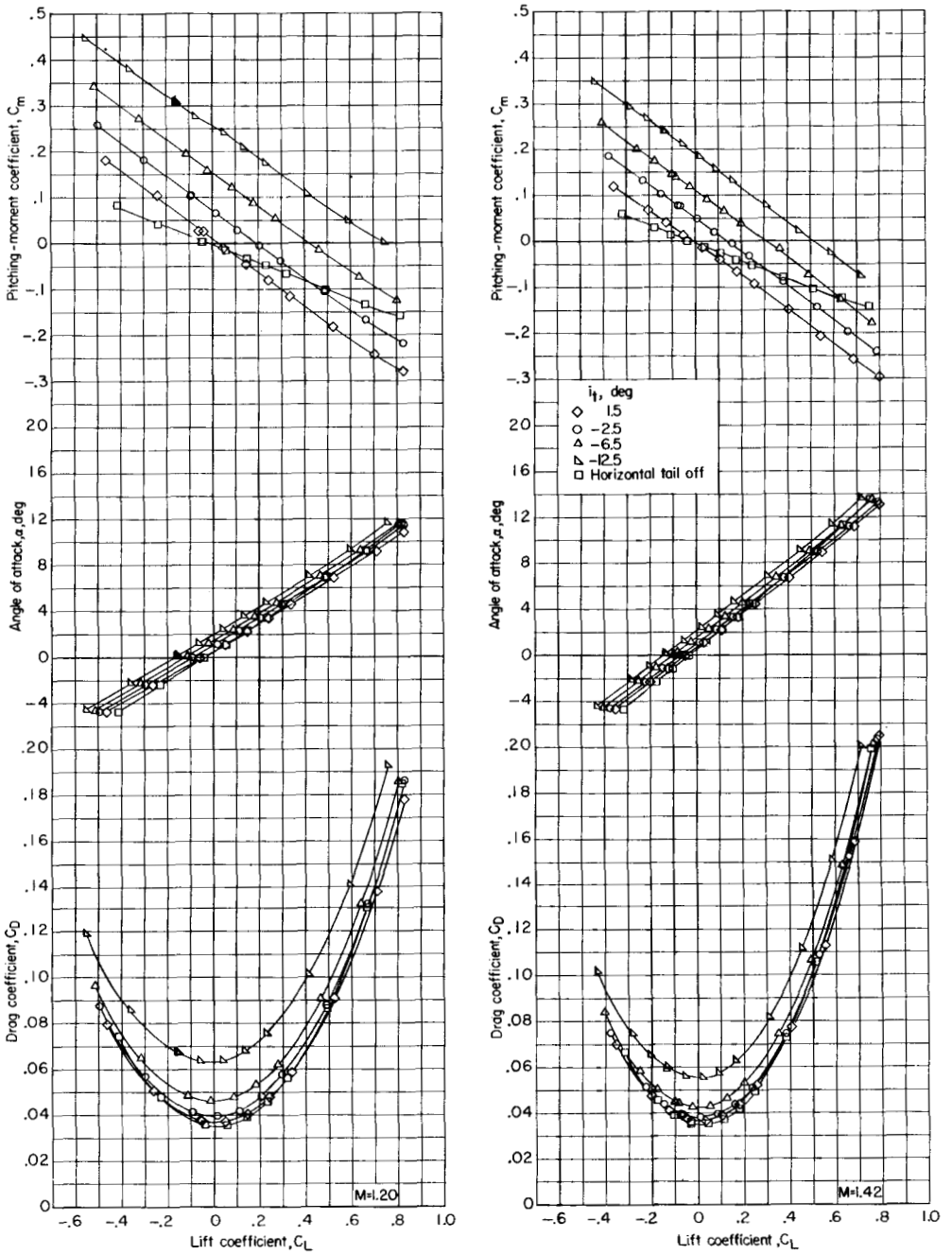

(e) M = 1.20 and 1.42; stagnation pressure, 0.5 atm.

Figure 8.- Continued.

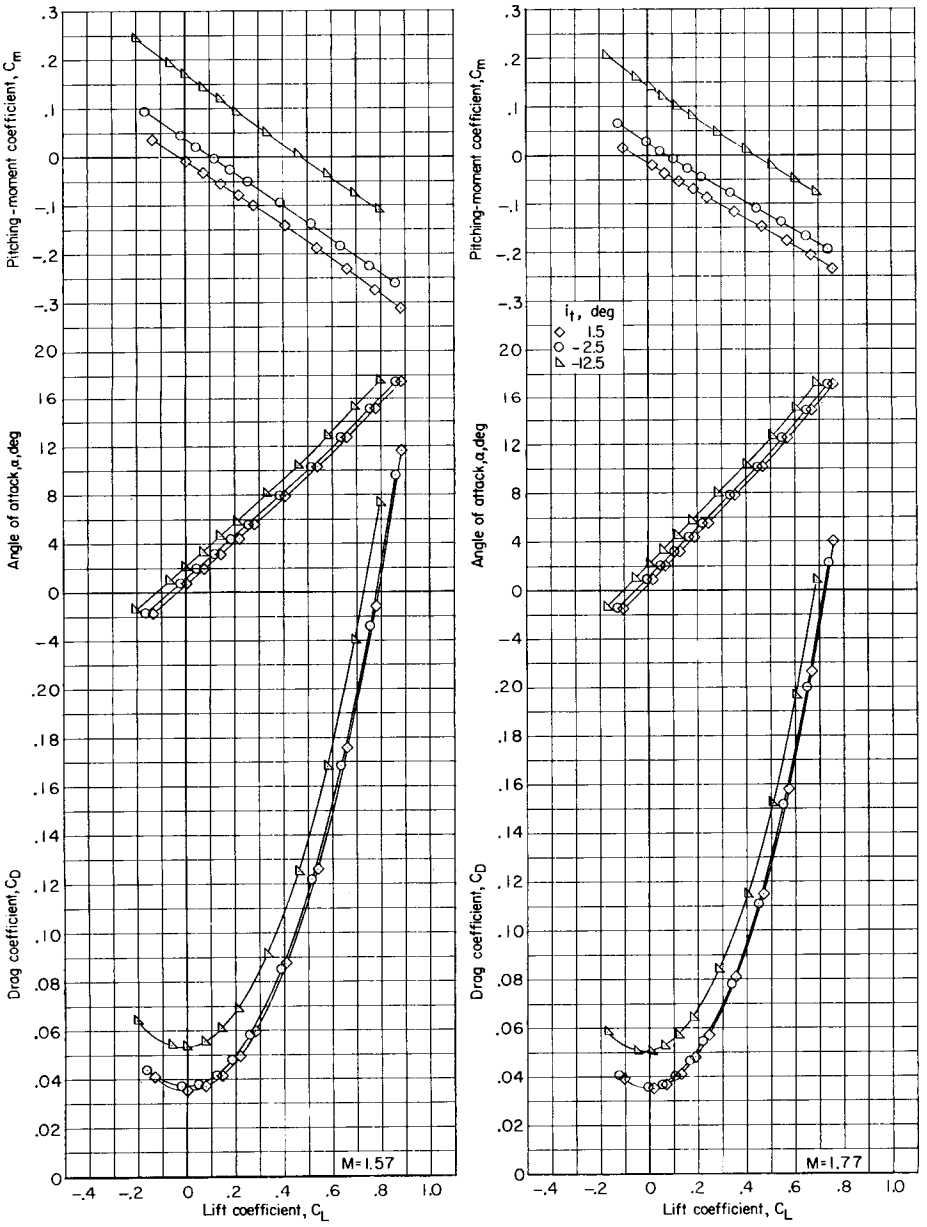

(f) M = 1.57 and 1.77; stagnation pressure, 0.68 atm.

Figure 8.- Continued.

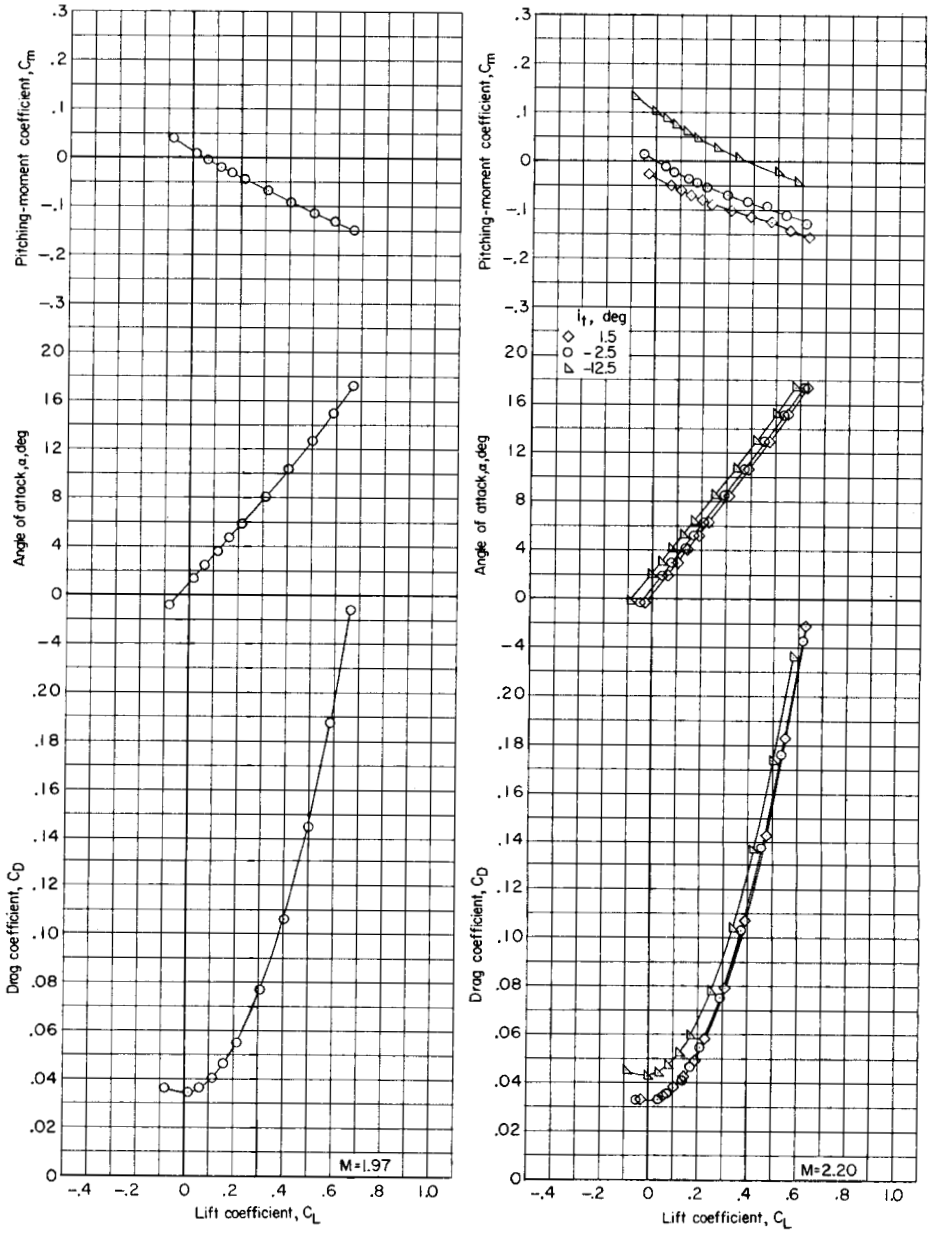

(g) M = 1.97 and 2.20; stagnation pressure, 0.68 atm.

Figure 8.- Concluded.

[redacted]

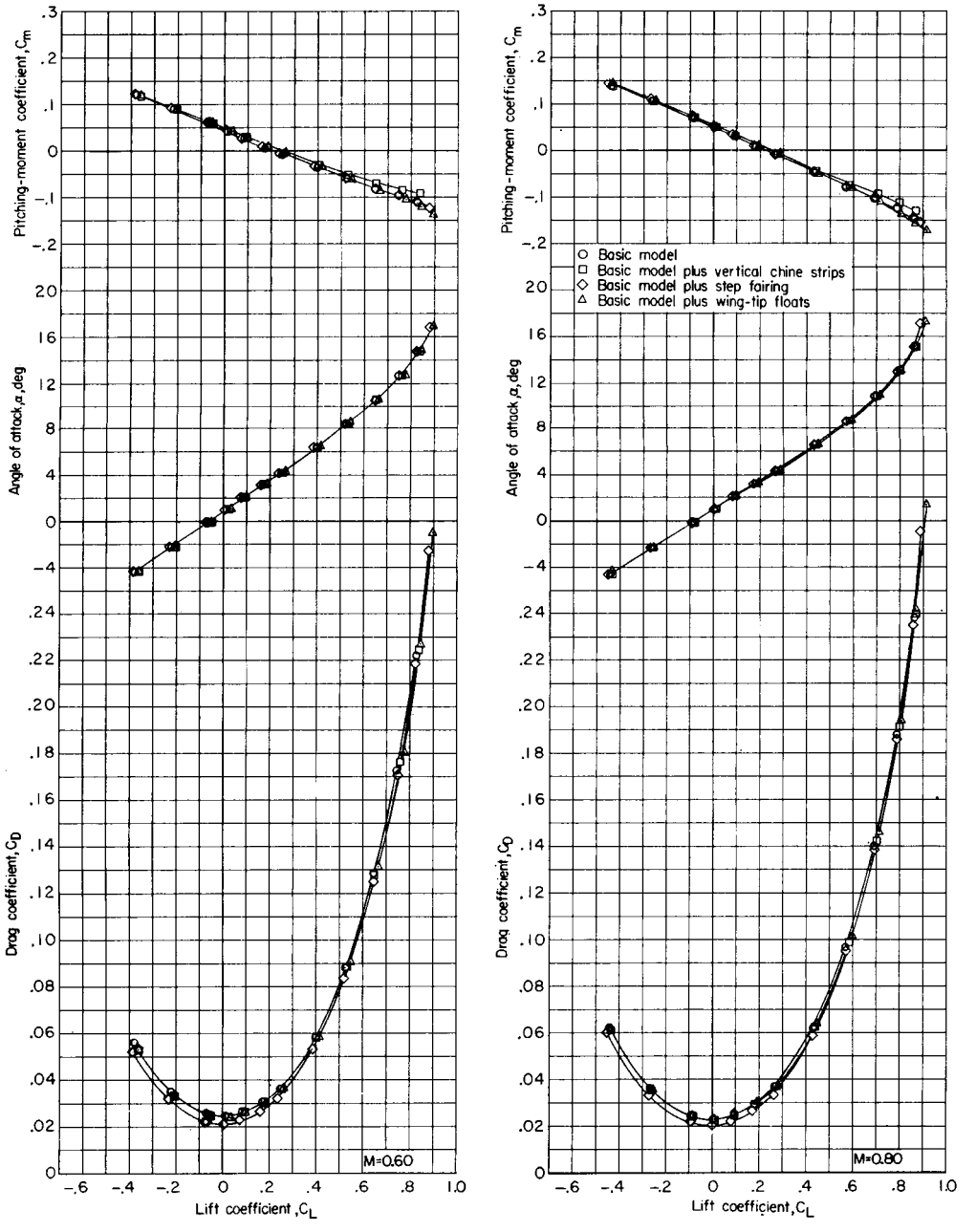

(a) M = 0.60 and 0.80; stagnation pressure, 0.5 atm.

Figure 9.- Effects of model modifications on longitudinal aerodynamic characteristics of basic model. Transition natural; $i_t = -2.5^o$.

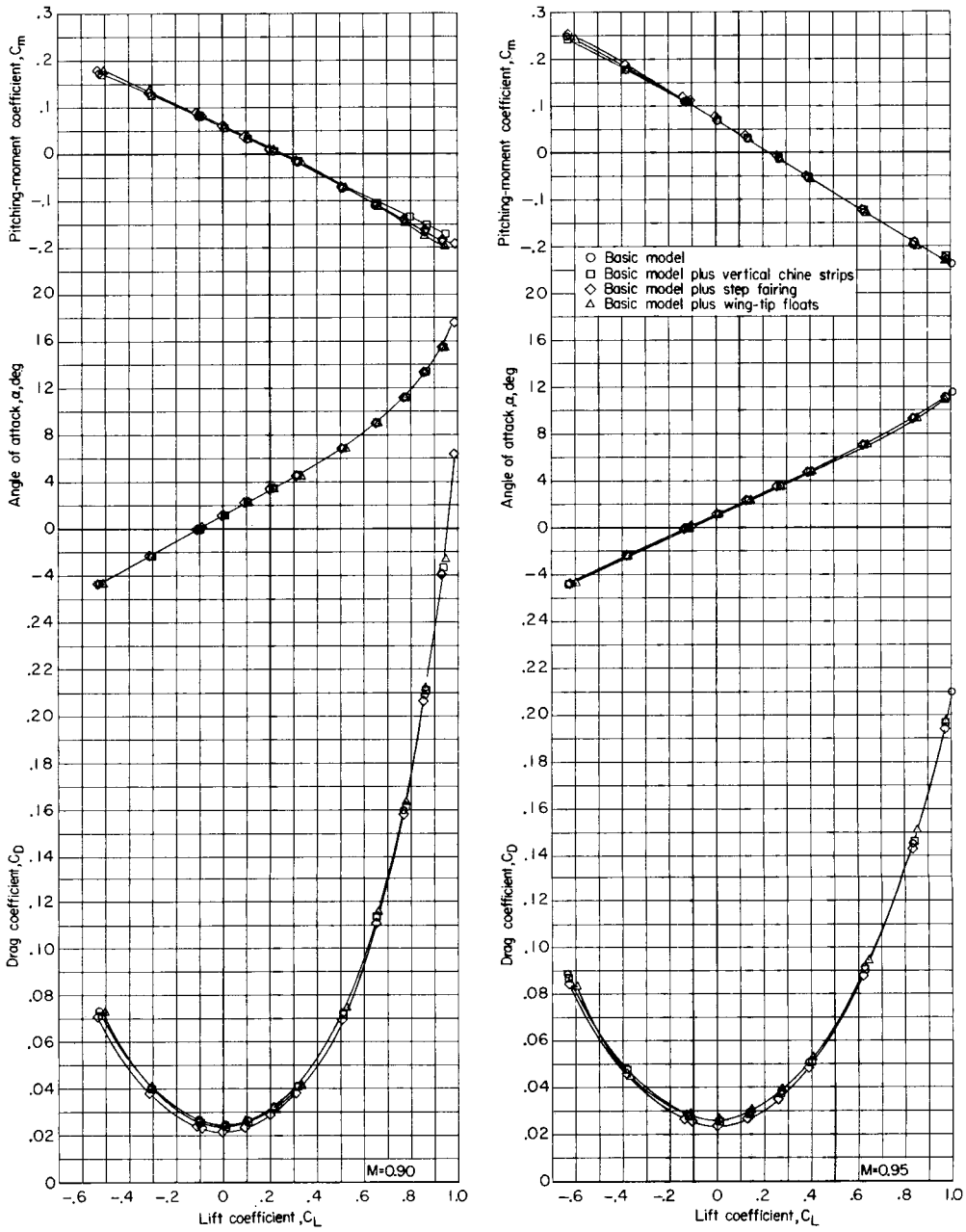

(b) M = 0.90 and 0.95; stagnation pressure, 0.5 atm.

Figure 9.- Continued.

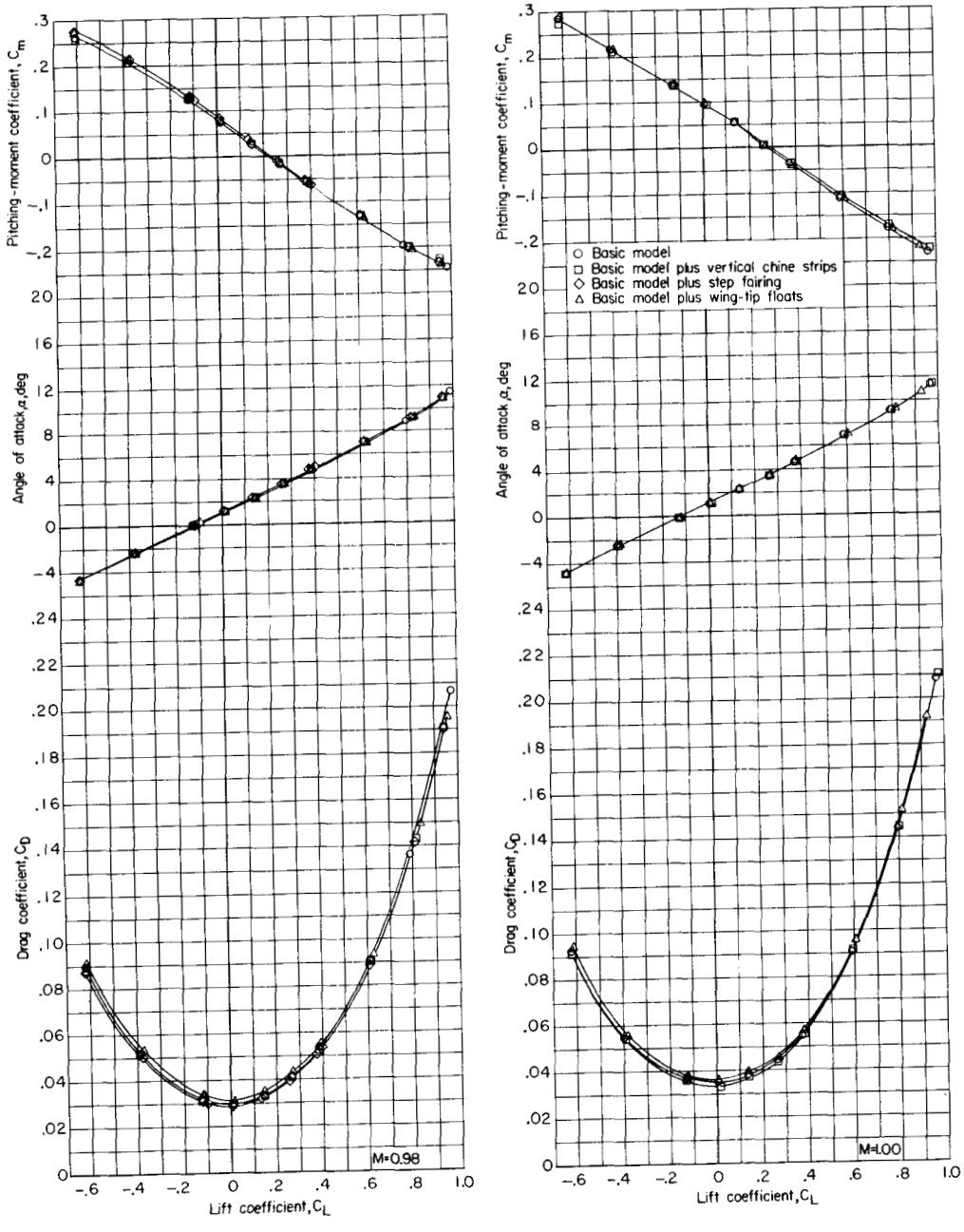

(c) M = 0.98 and 1.00; stagnation pressure, 0.5 atm.

Figure 9.- Continued.

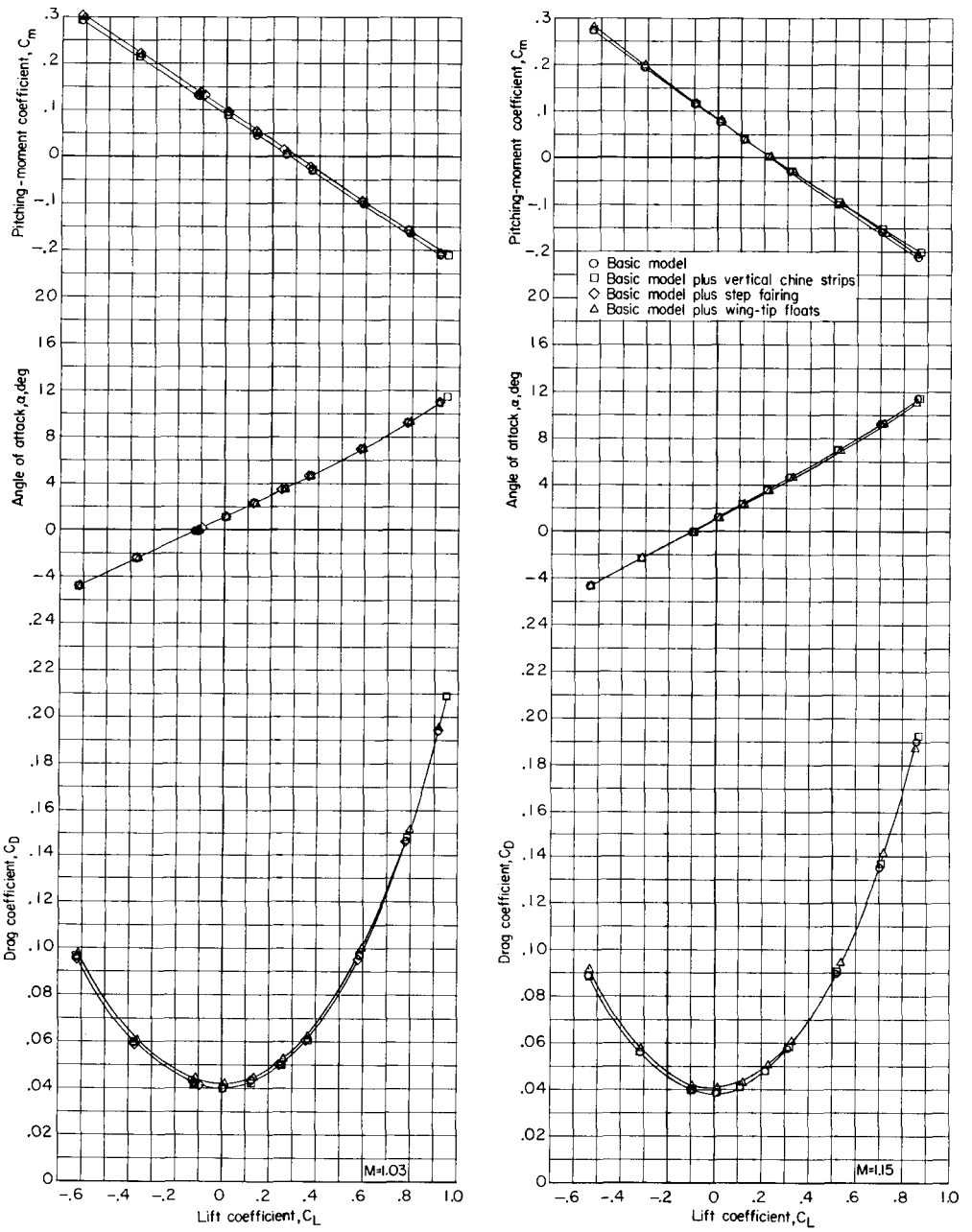

(d) M = 1.03 and 1.15; stagnation pressure, 0.5 atm.

Figure 9.- Continued.

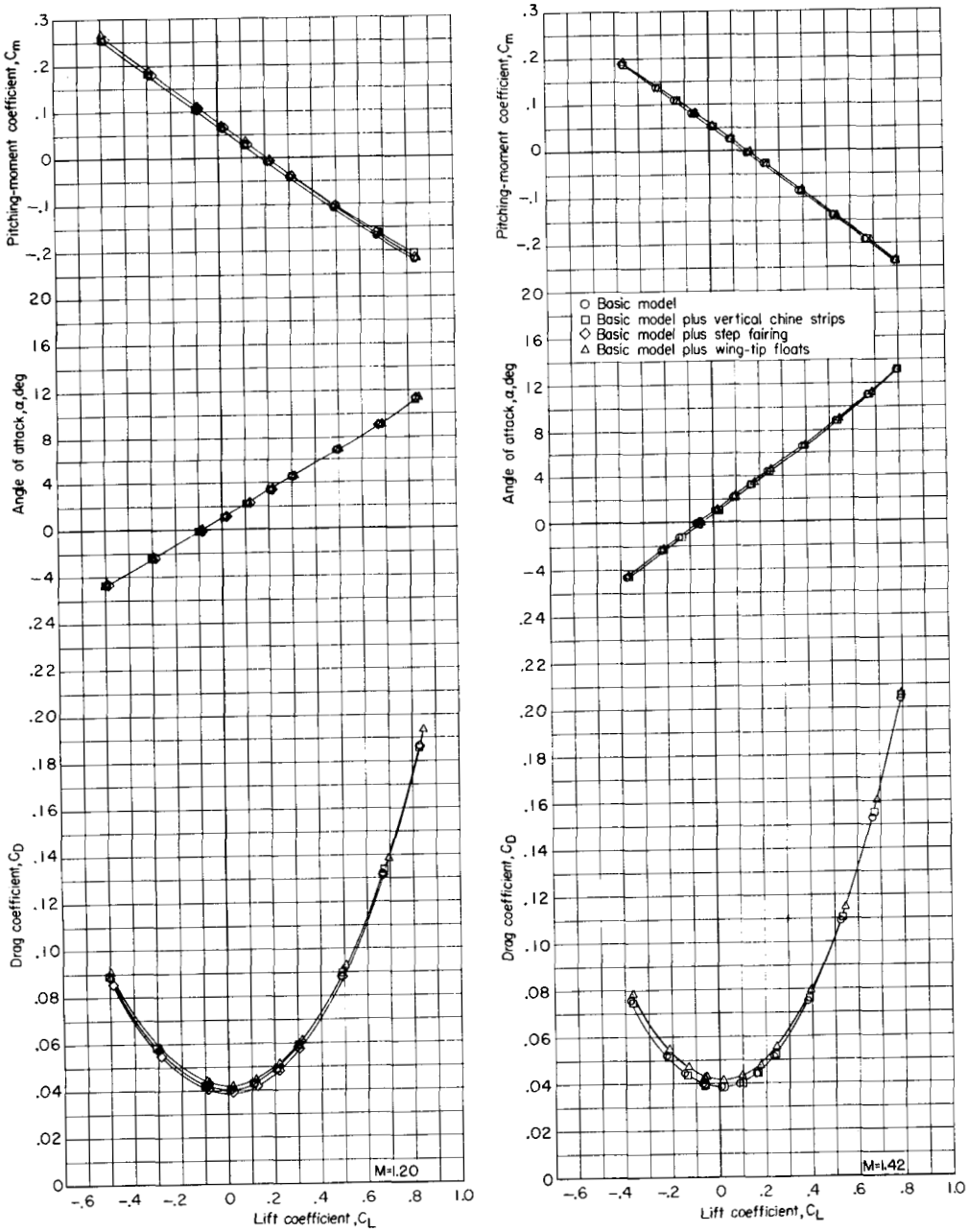

(e) M = 1.20 and 1.42; stagnation pressure, 0.5 atm.

Figure 9.- Continued.

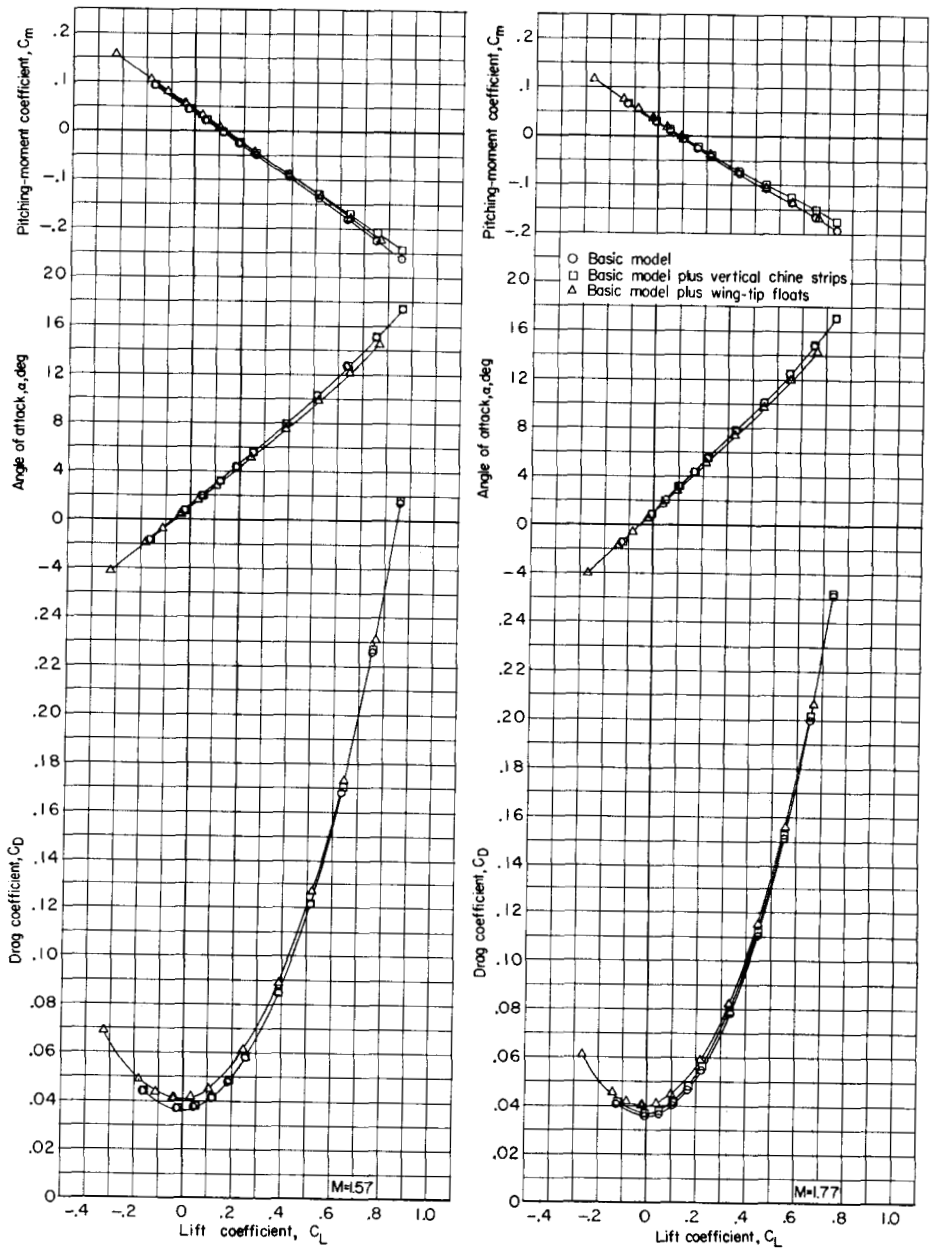

(f) M = 1.57 and 1.77; stagnation pressure, 0.68 atm.

Figure 9.- Continued.

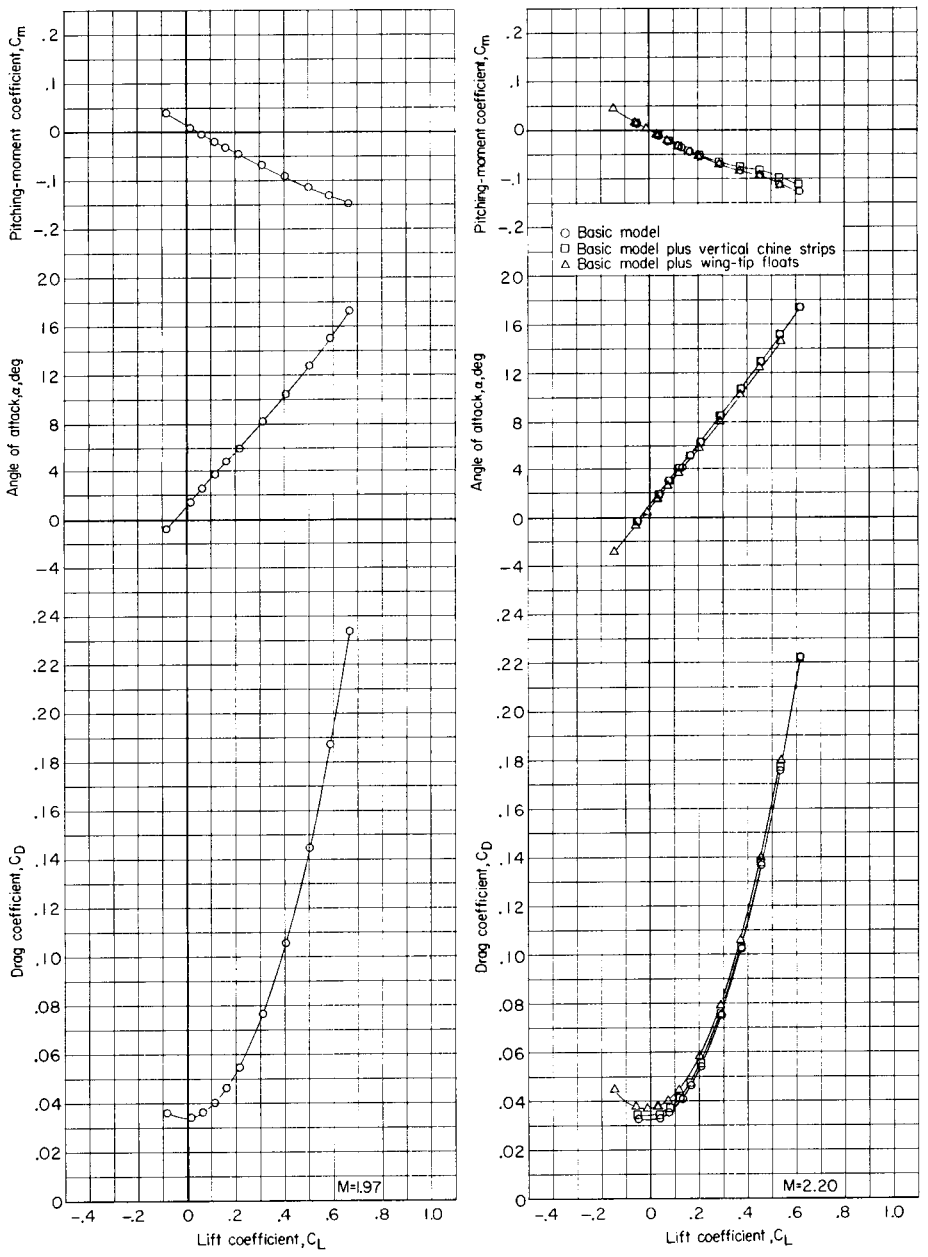

(g) M = 1.97 and 2.20; stagnation pressure, 0.68 atm.

Figure 9.- Concluded.

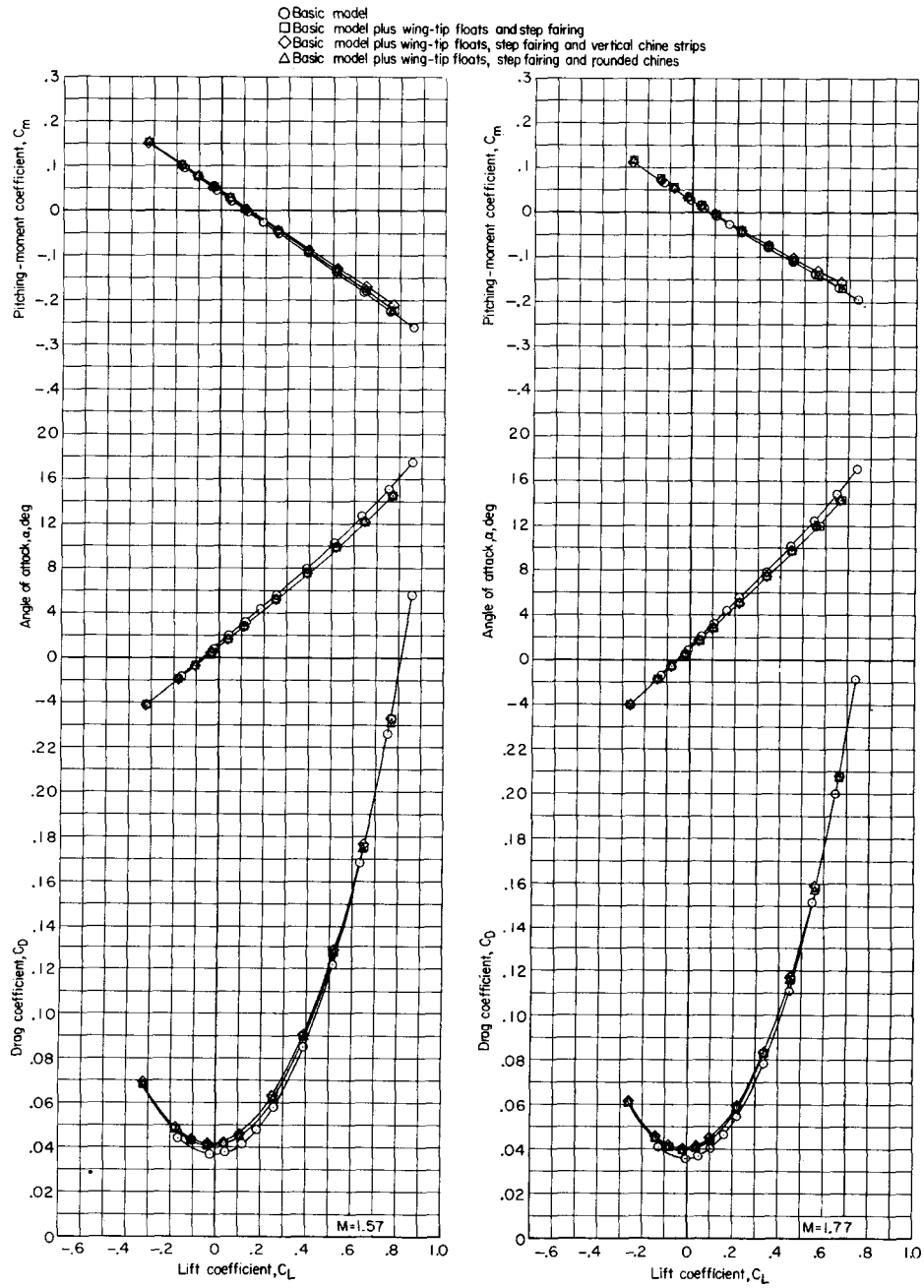

(a) M = 1.57 and 1.77.

Figure 10.- Effects of combined modifications on longitudinal aerodynamic characteristics of basic model. Transition natural; i_t = -2.5°; stagnation pressure, 0.68 atm.

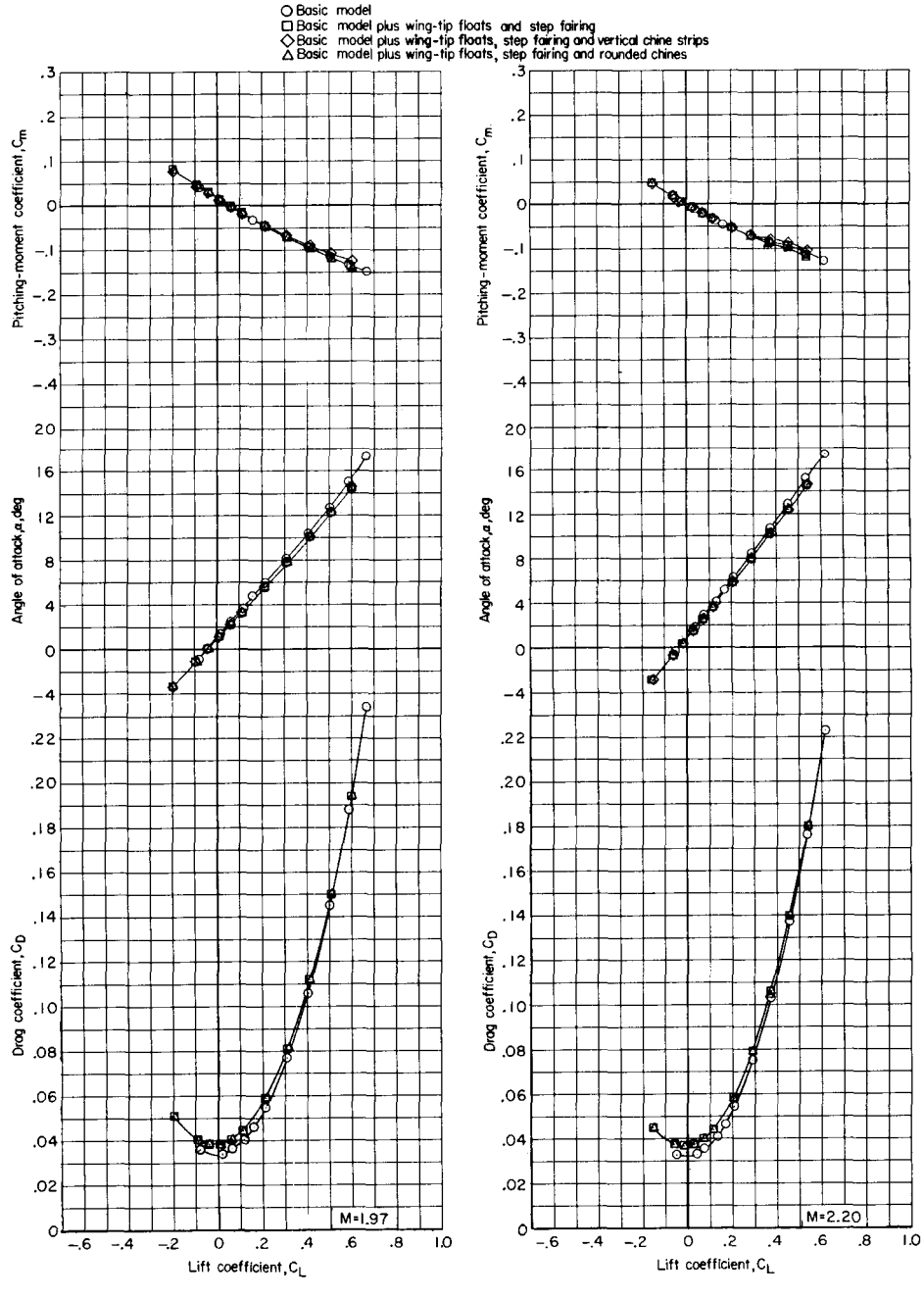

(b) M = 1.97 and 2.20.

Figure 10.- Concluded.

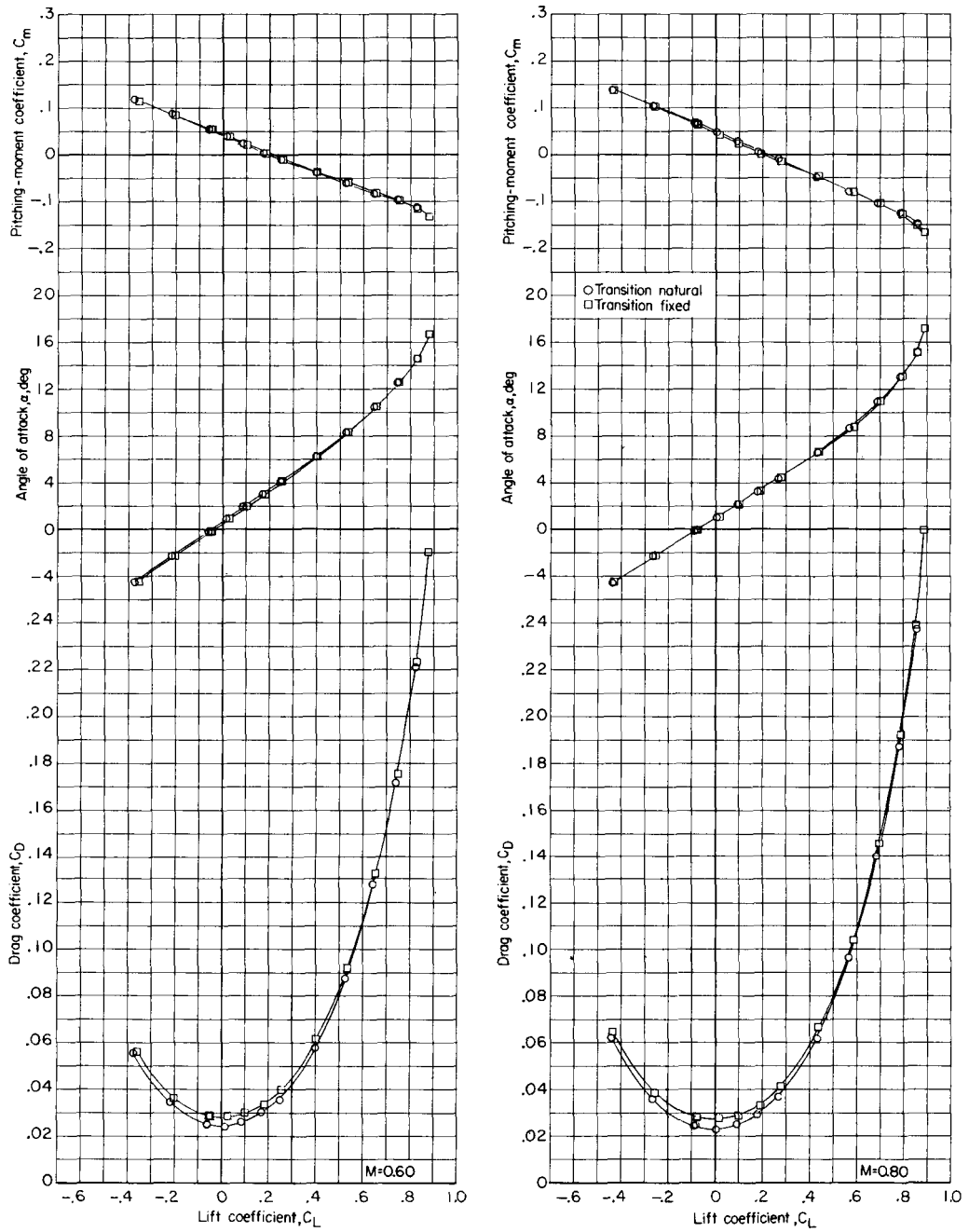

(a) M = 0.60 and 0.80.

Figure 11.- Effects of transition on longitudinal aerodynamic characteristics of basic model. Stagnation pressure, 0.5 atm; $i_t = -2.5^\circ$.

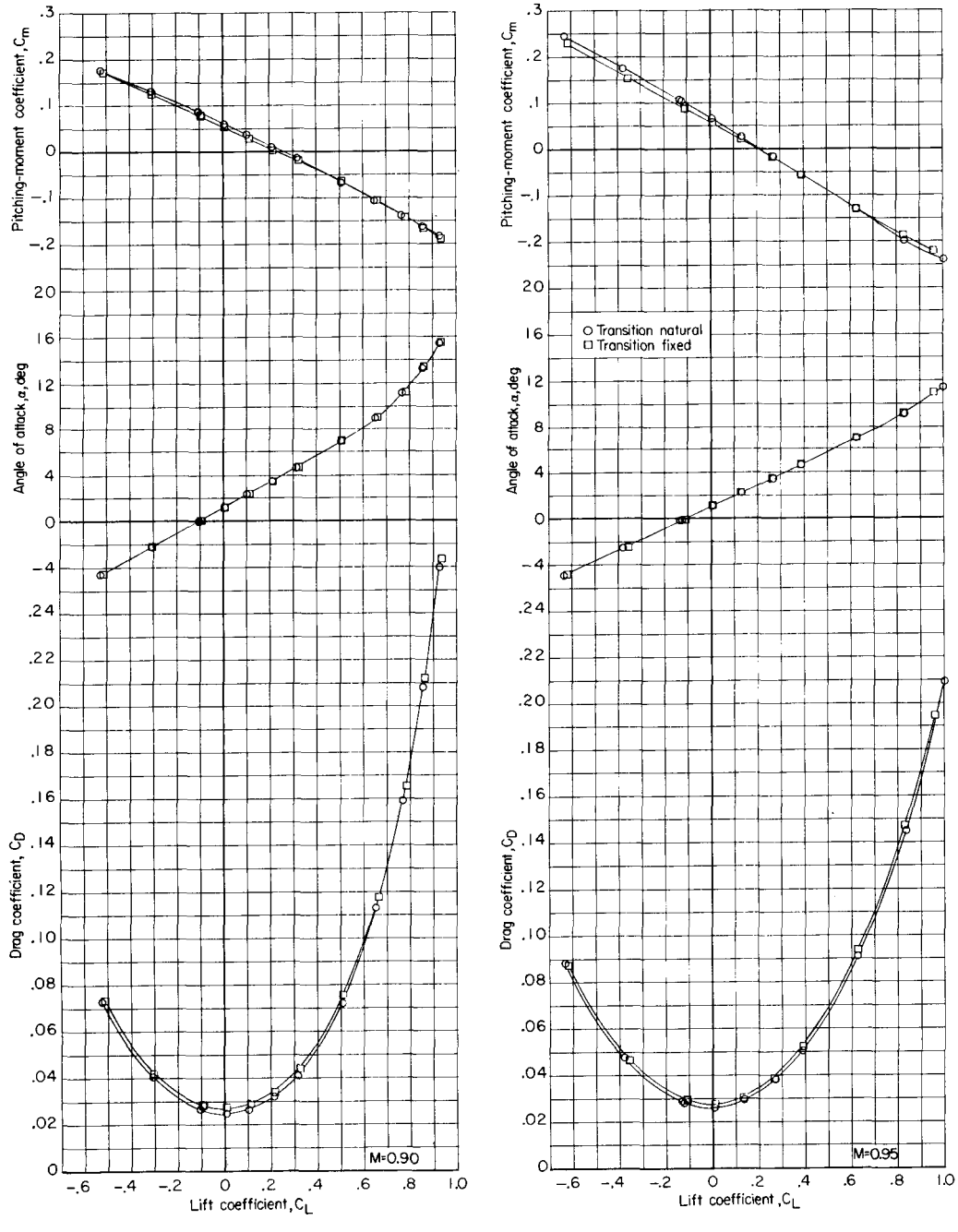

(b) M = 0.90 and 0.95.

Figure 11.- Continued.

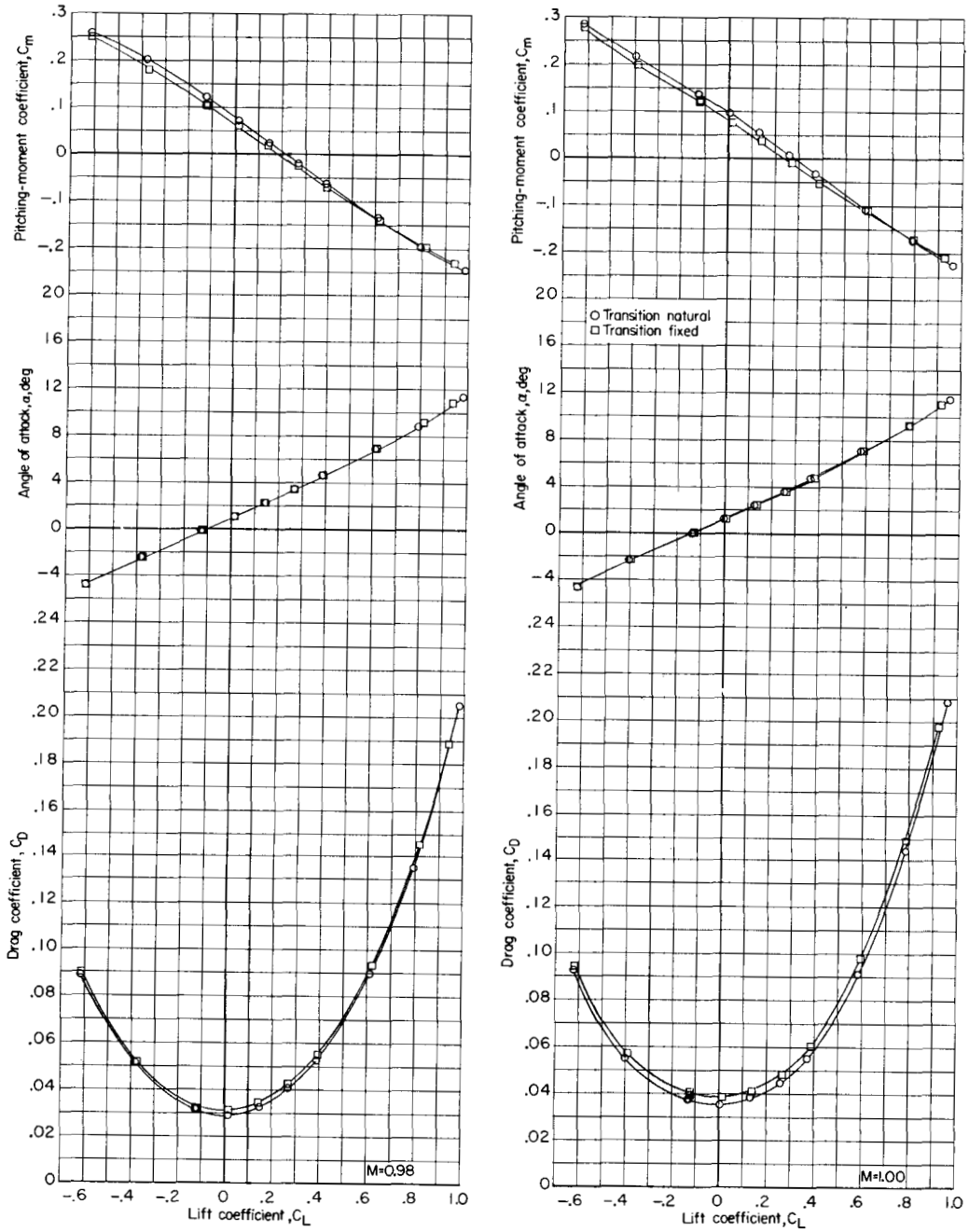

(c) M = 0.98 and 1.00.

Figure 11.- Continued.

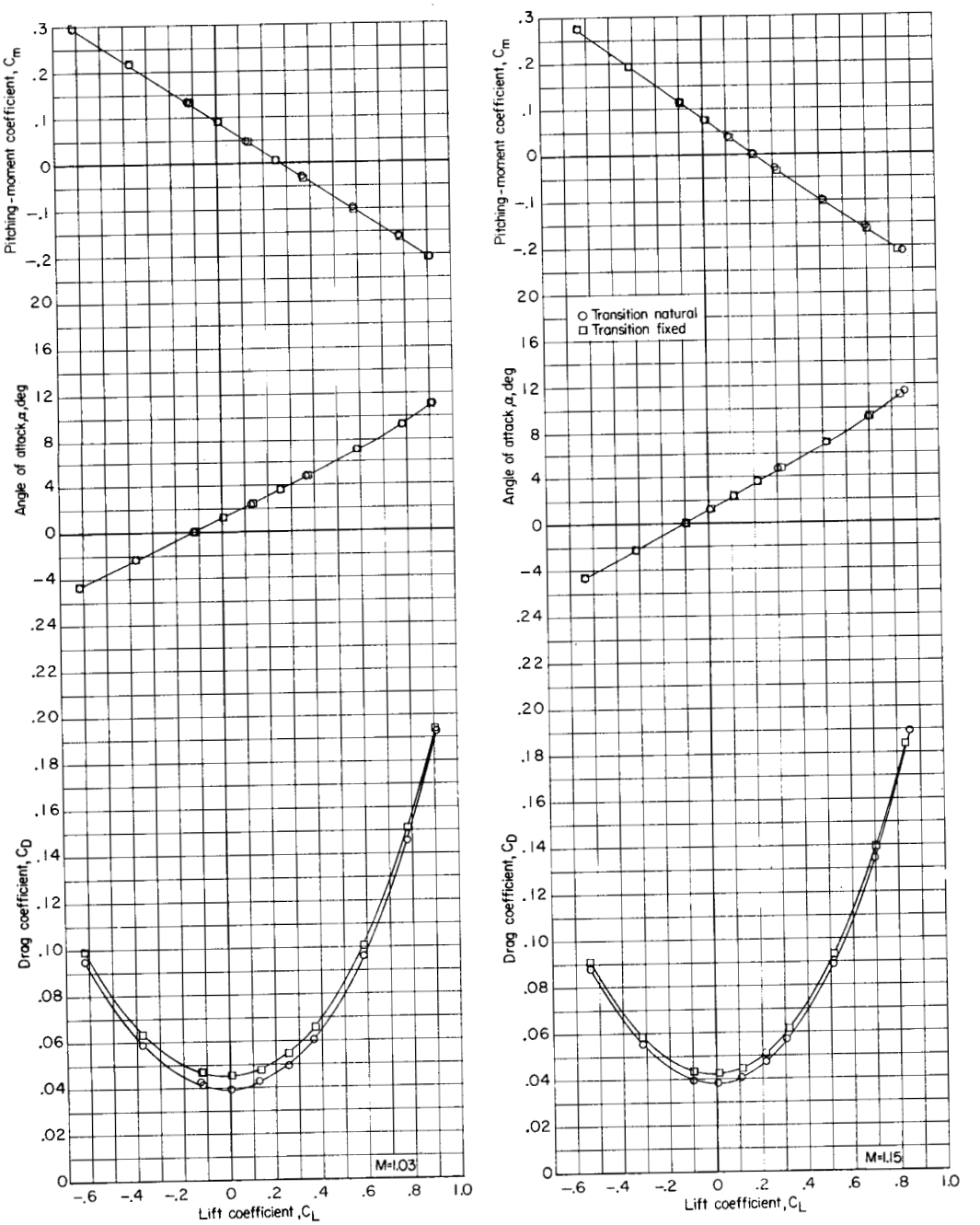

(d) M = 1.03 and 1.15.

Figure 11.- Continued.

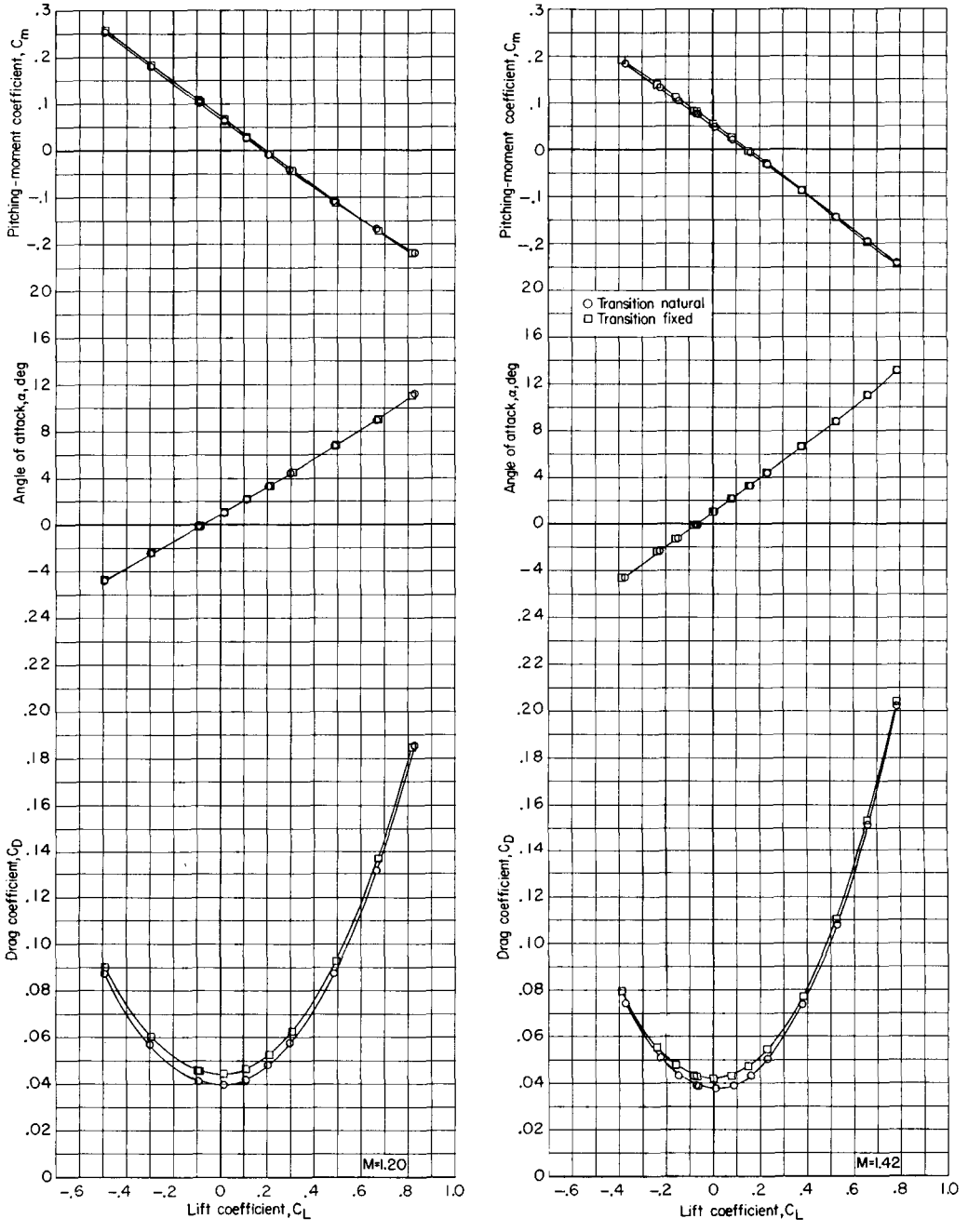

(e) M = 1.20 and 1.42.

Figure 11.- Concluded.

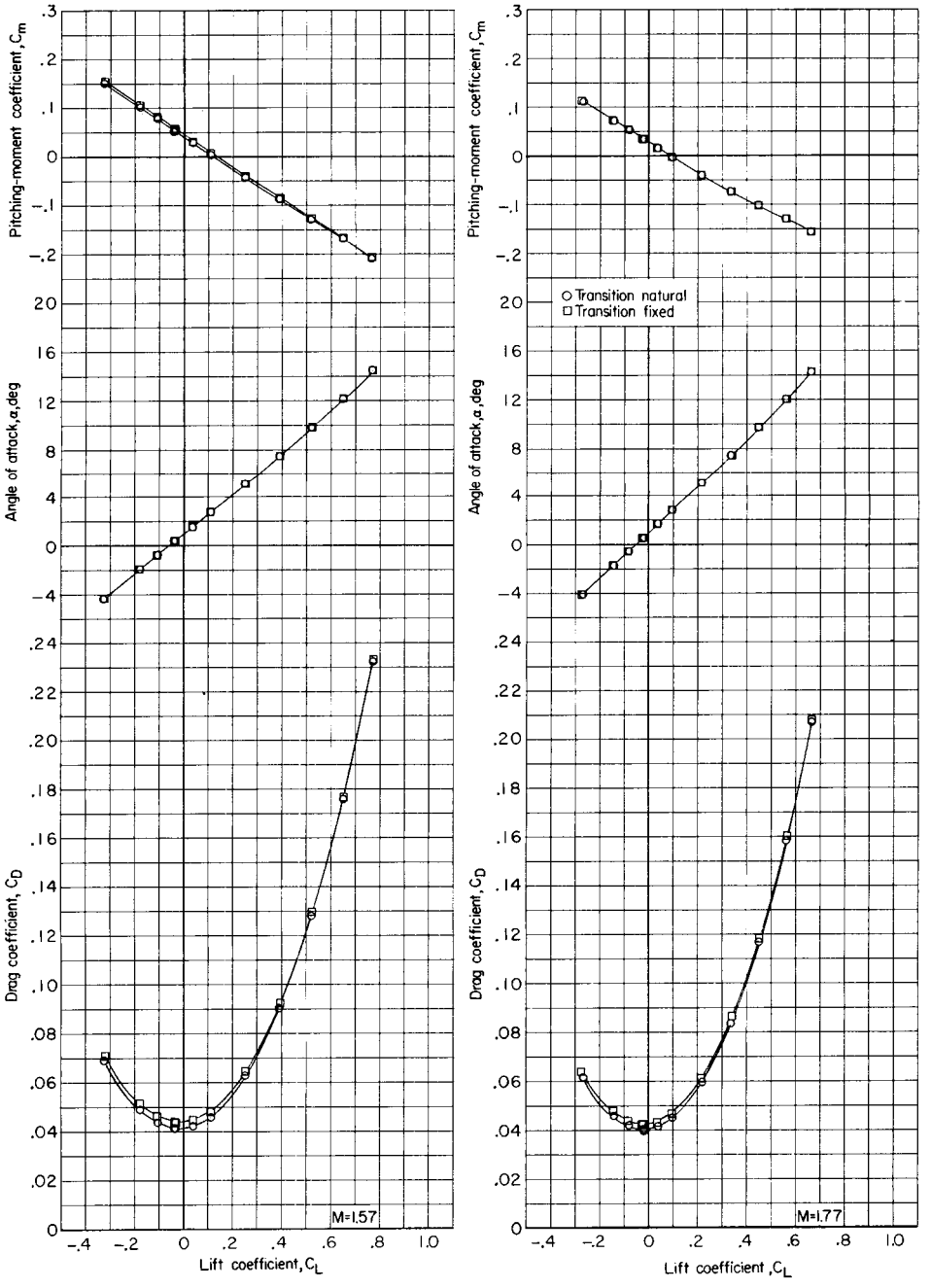

Figure 12.- Effects of transition on longitudinal aerodynamic characteristics of basic model plus wingtip floats, step fairing, and vertical chine strips. Stagnation pressure, 0.68 atm; $i_t = -2.5^\circ$.

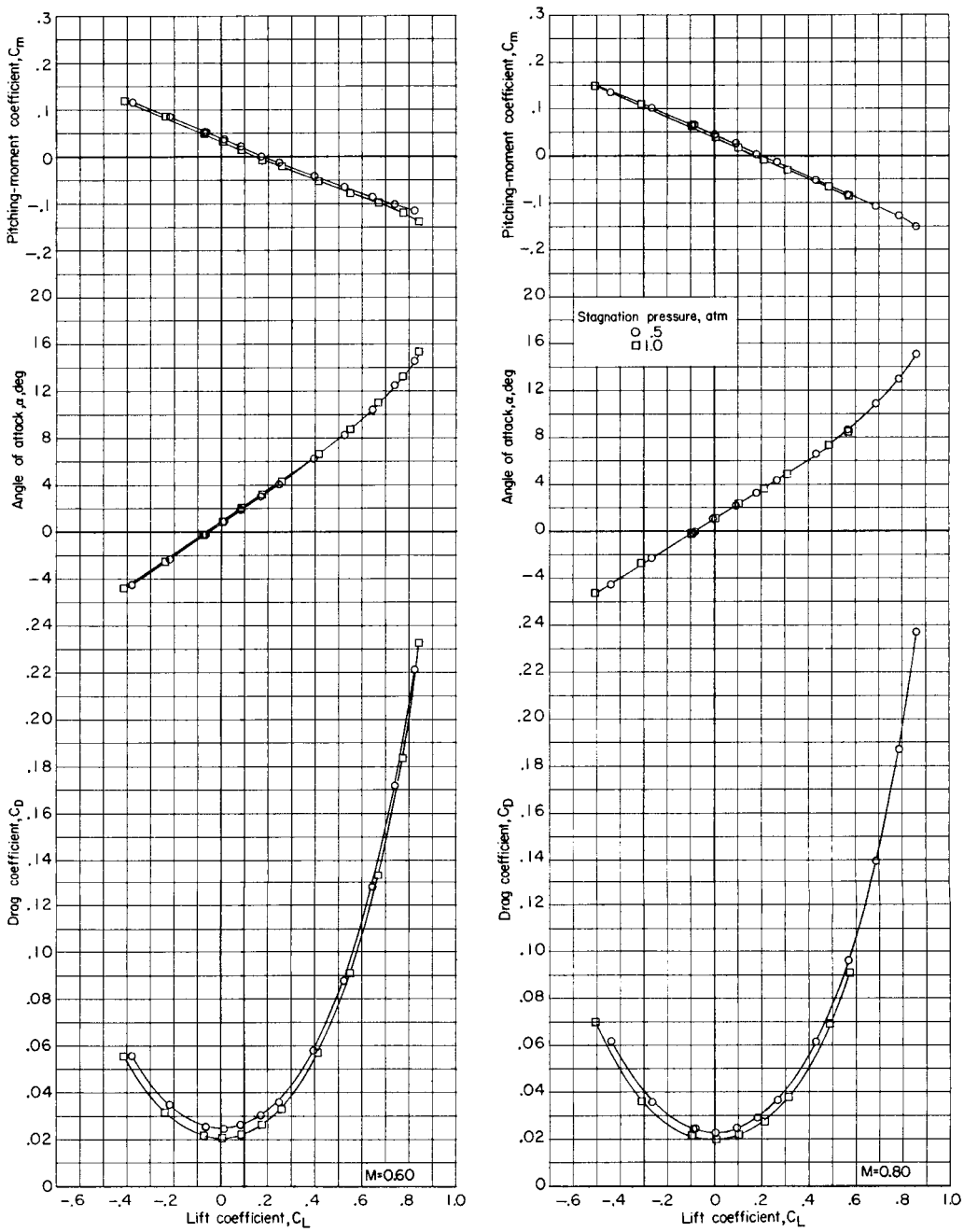

(a) M = 0.60 and 0.80.

Figure 13.- Effects of Reynolds number on longitudinal aerodynamic characteristics of basic model. Natural transition; $i_t = -2.5^\circ$.

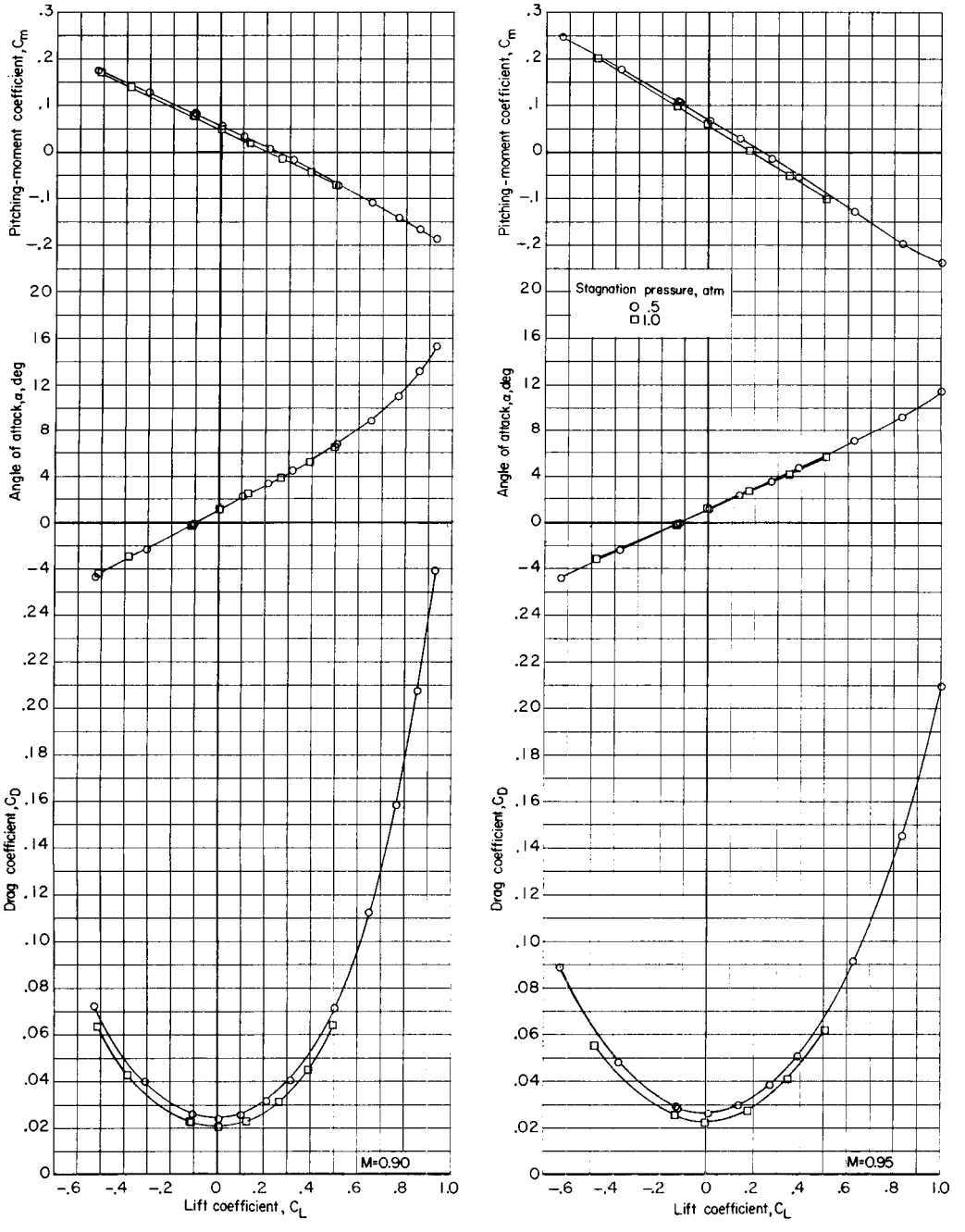

(b) M = 0.90 and 0.95.

Figure 13.- Continued.

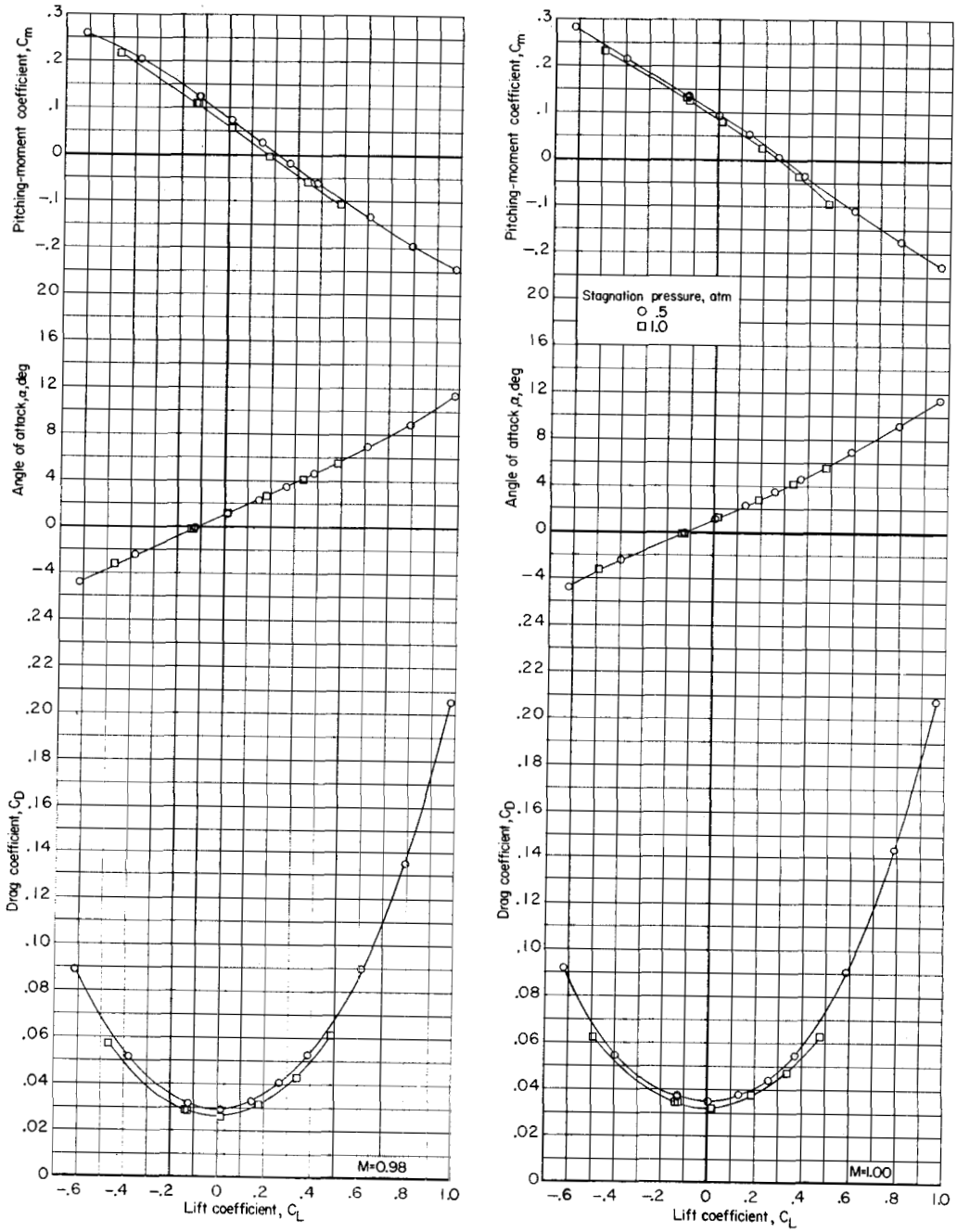

(c) M = 0.98 and 1.00.

Figure 13.- Continued.

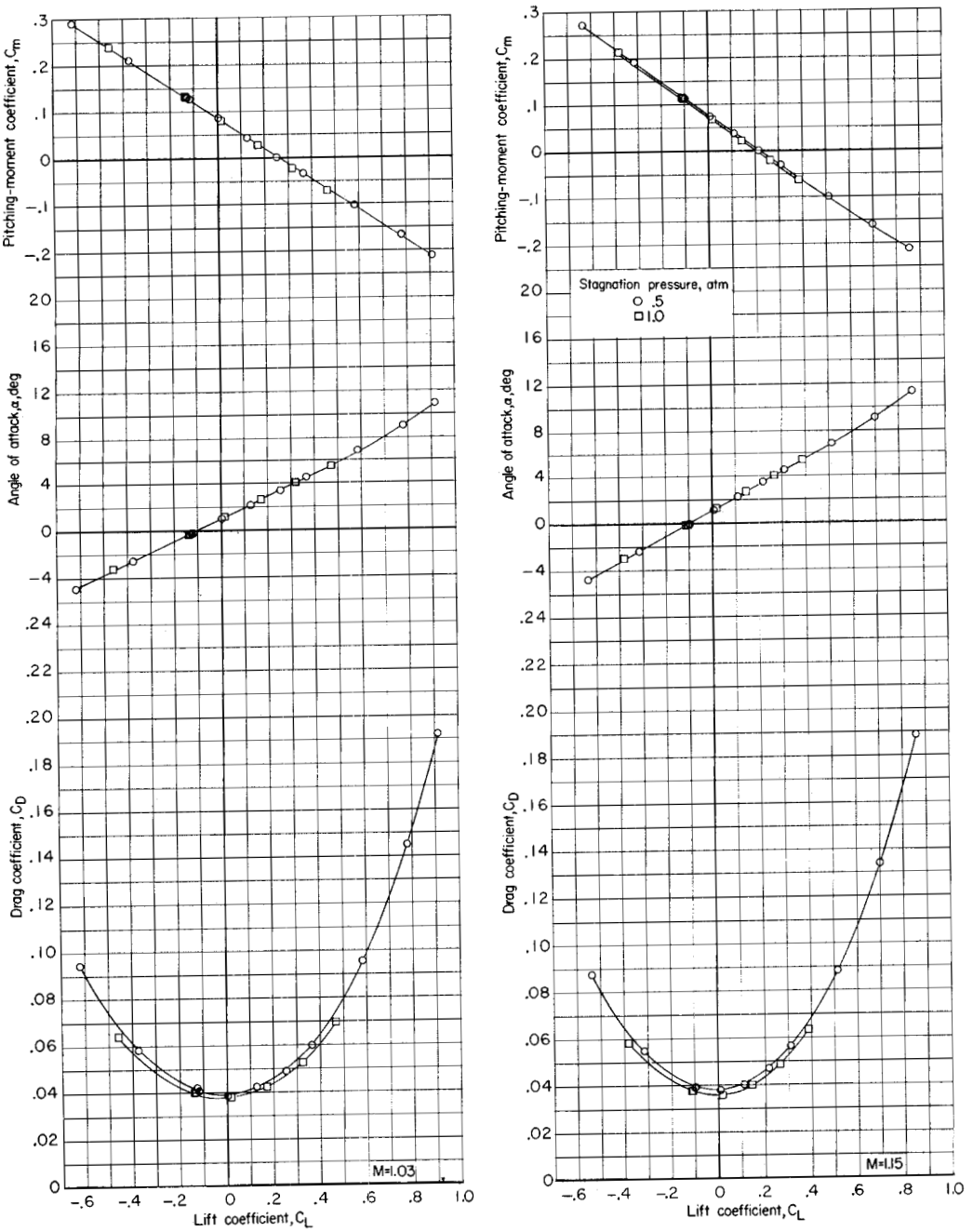

(d) M = 1.03 and 1.15.

Figure 13.- Continued.

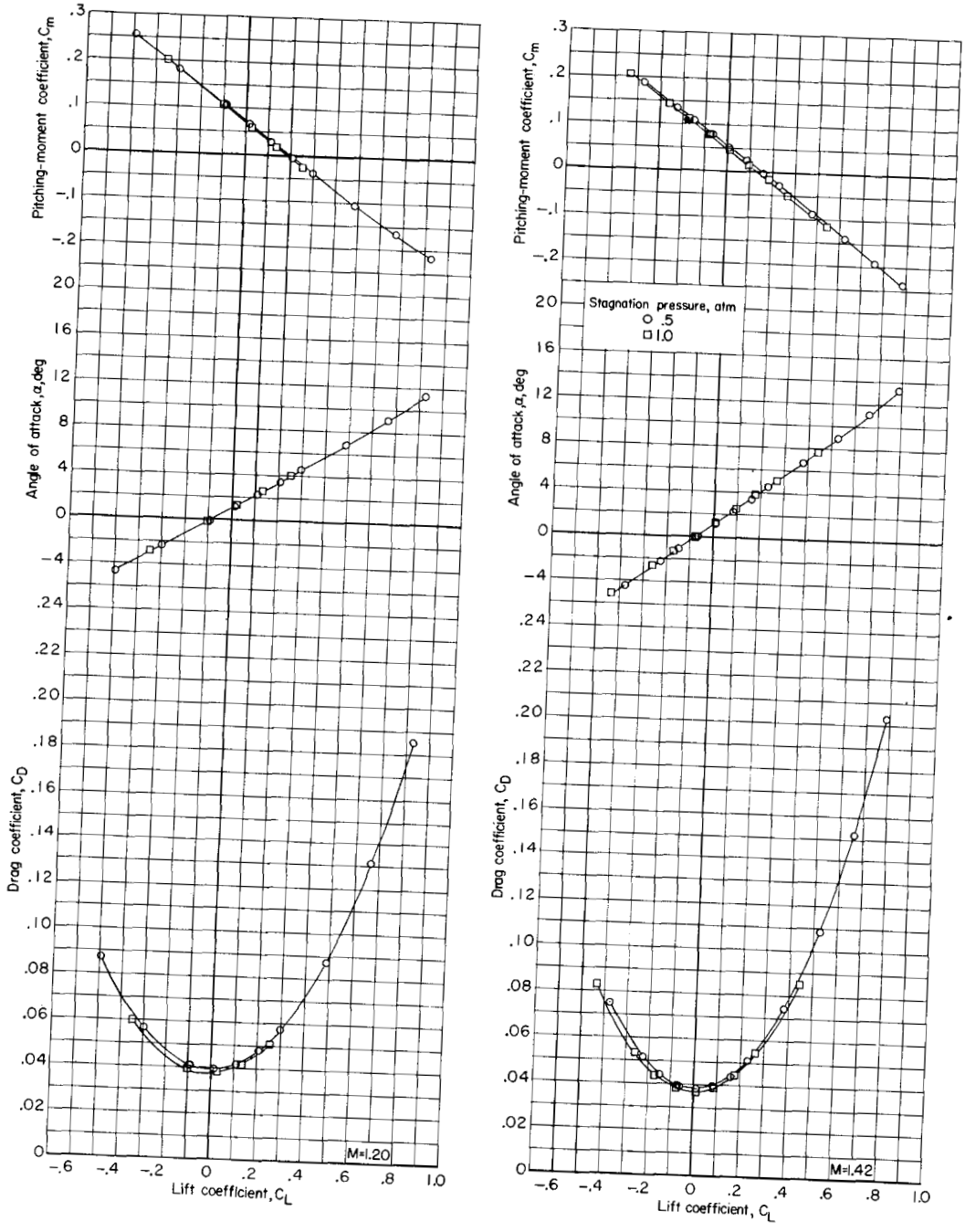

(e) M = 1.20 and 1.42.

Figure 13.- Concluded.

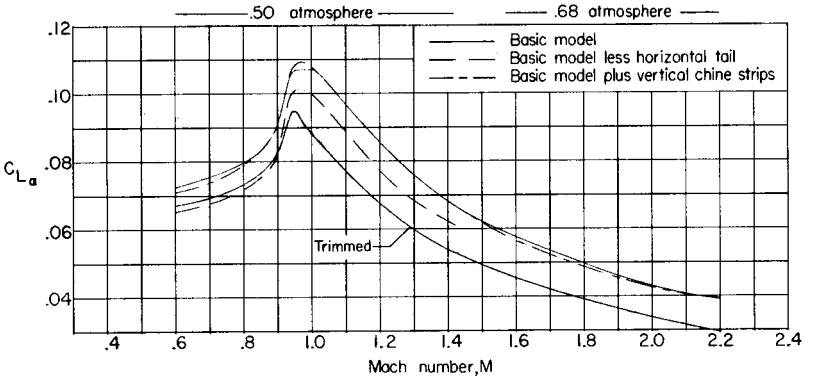

(a) Effects of horizontal tail and vertical chine strips.

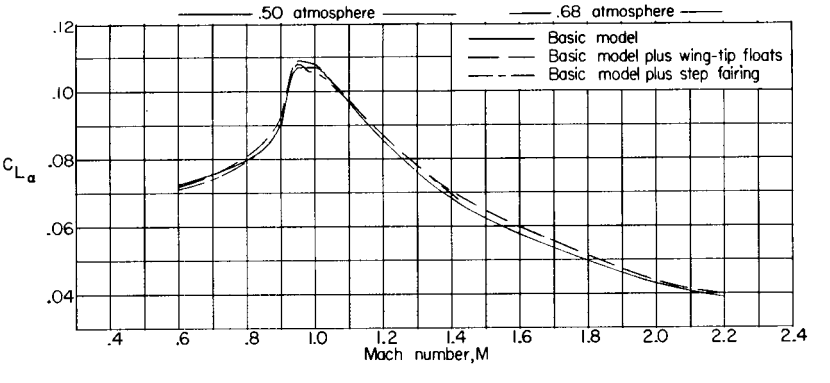

(b) Effects of wingtip floats and step fairing.

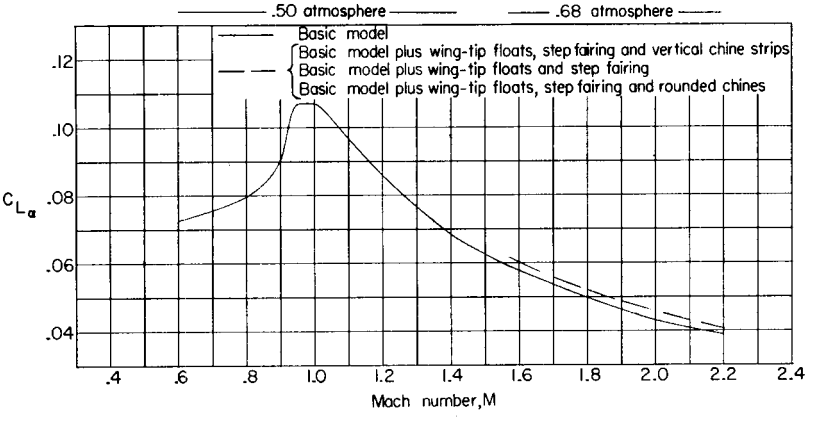

(c) Effects of combined modifications.

Figure 14.- Variation of lift-curve slope C_{L_α} with Mach number.

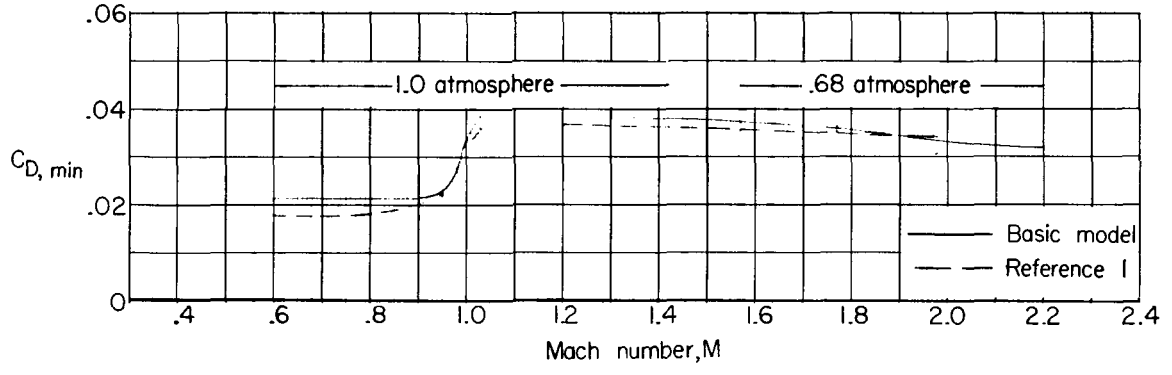

(a) Comparison of basic model to model of reference 1.

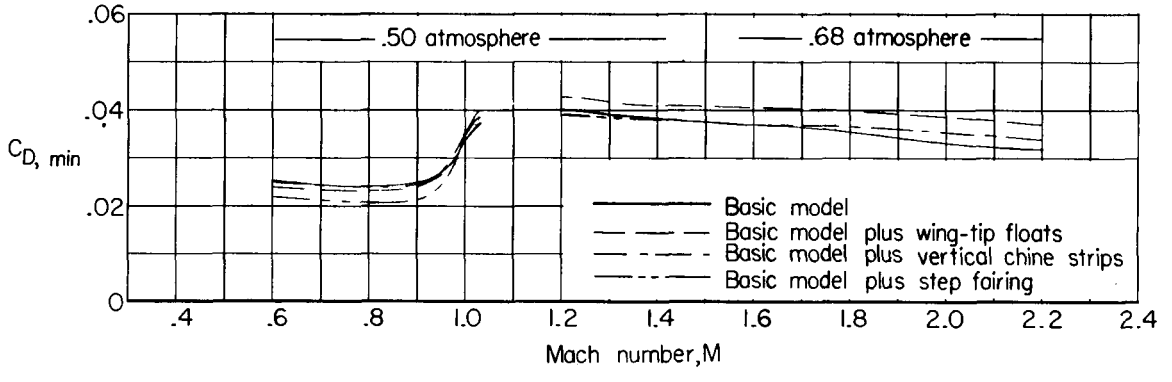

(b) Effects of model modifications.

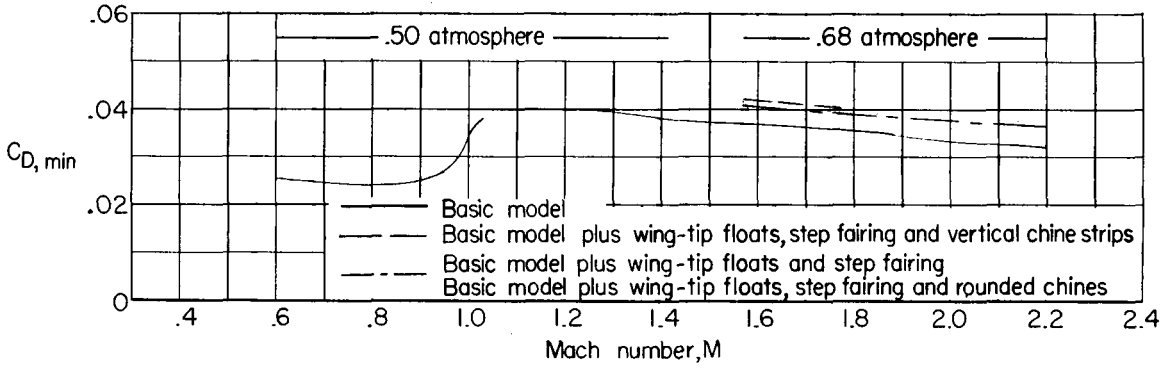

(c) Effects of combined modifications.

Figure 15.- Variation of minimum drag coefficient $C_{D_{min}}$ with Mach number with $i_t = -2.5^\circ$.

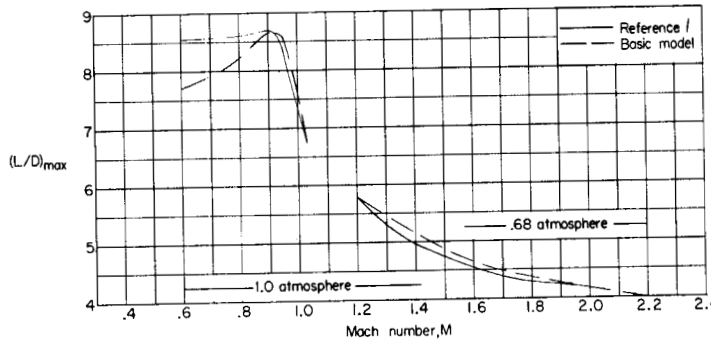

(a) Comparison of basic model to model of reference 1.

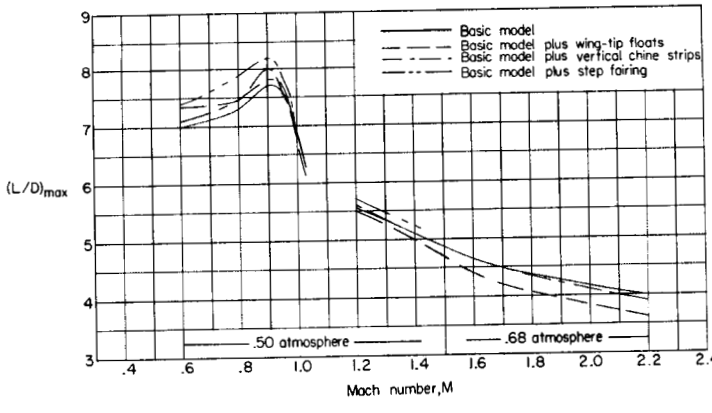

(b) Effects of model modifications.

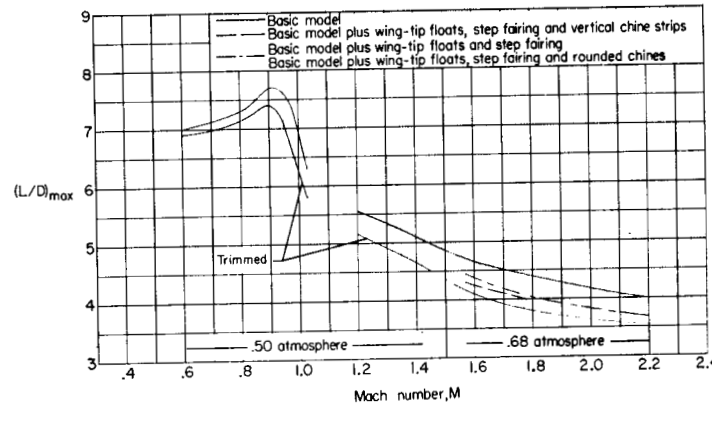

(c) Effects of combined modifications.

Figure 16.- Variation of maximum lift-drag ratio $(L/D)_{max}$ with Mach number.

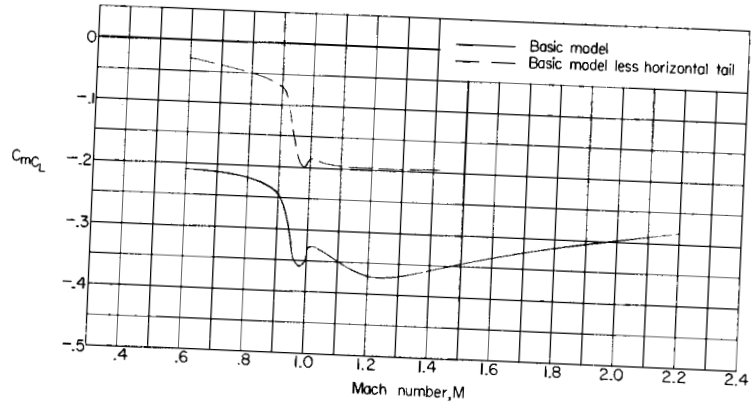

(a) Effect of horizontal tail.

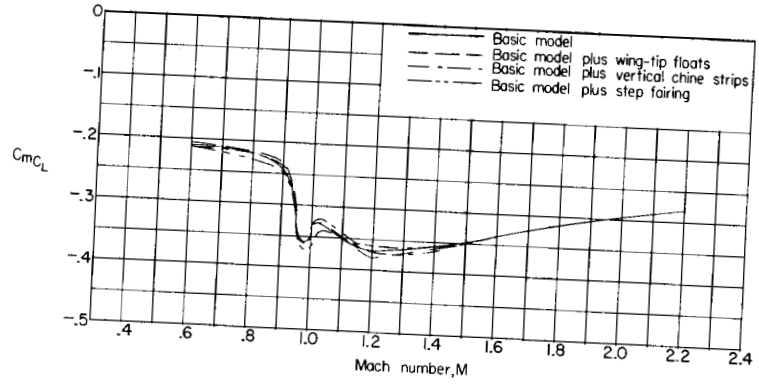

(b) Effects of model modifications.

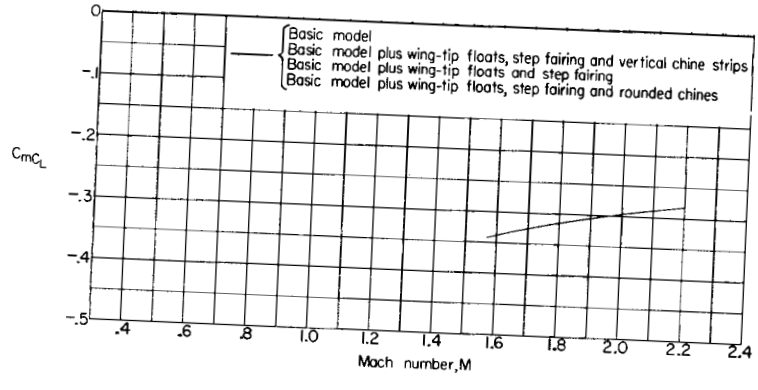

(c) Effects of combined modifications.

Figure 17.- Variation of static longitudinal stability parameter C_{mC_L} with Mach number.

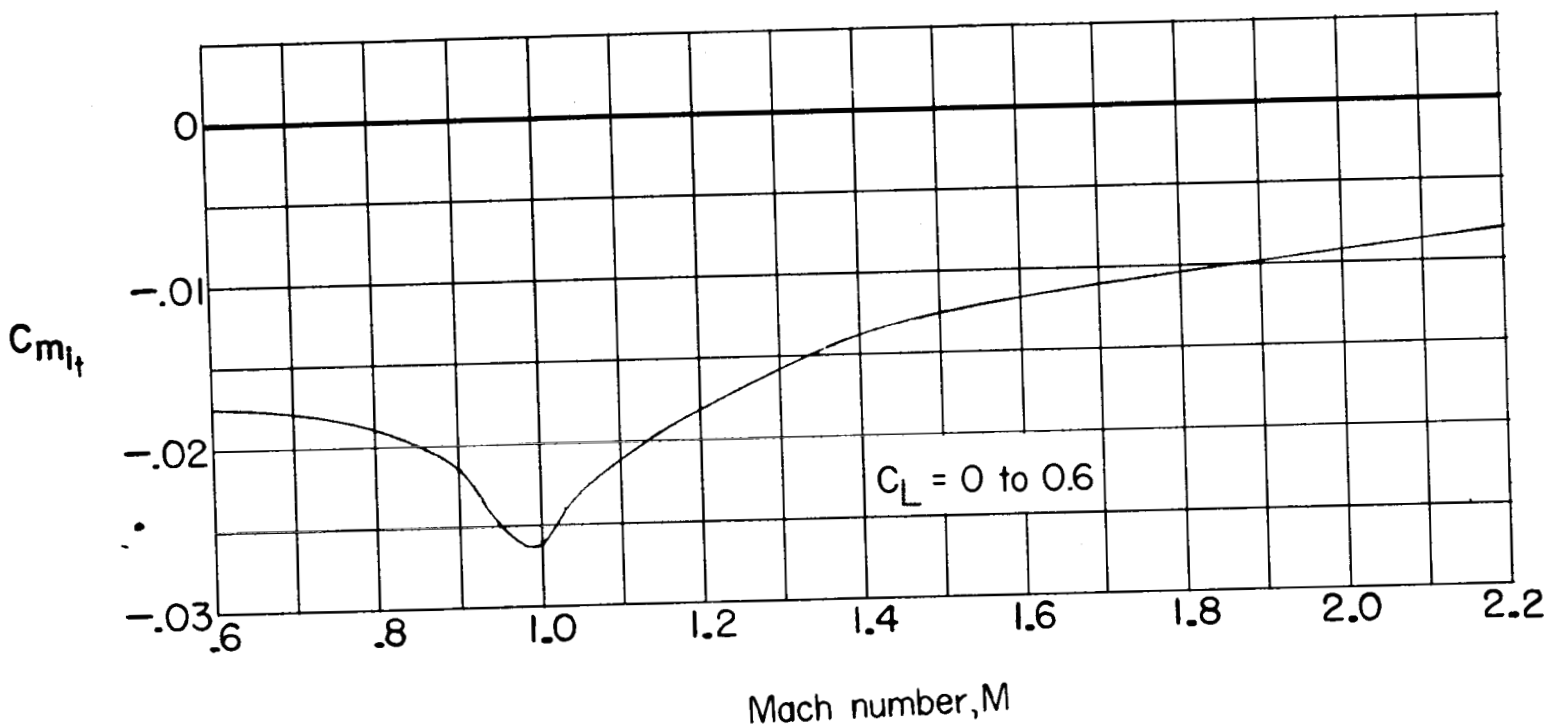

Figure 18.- Variation of horizontal-tail-effectiveness parameter $C_{m_{i_t}}$ for basic model with Mach number.

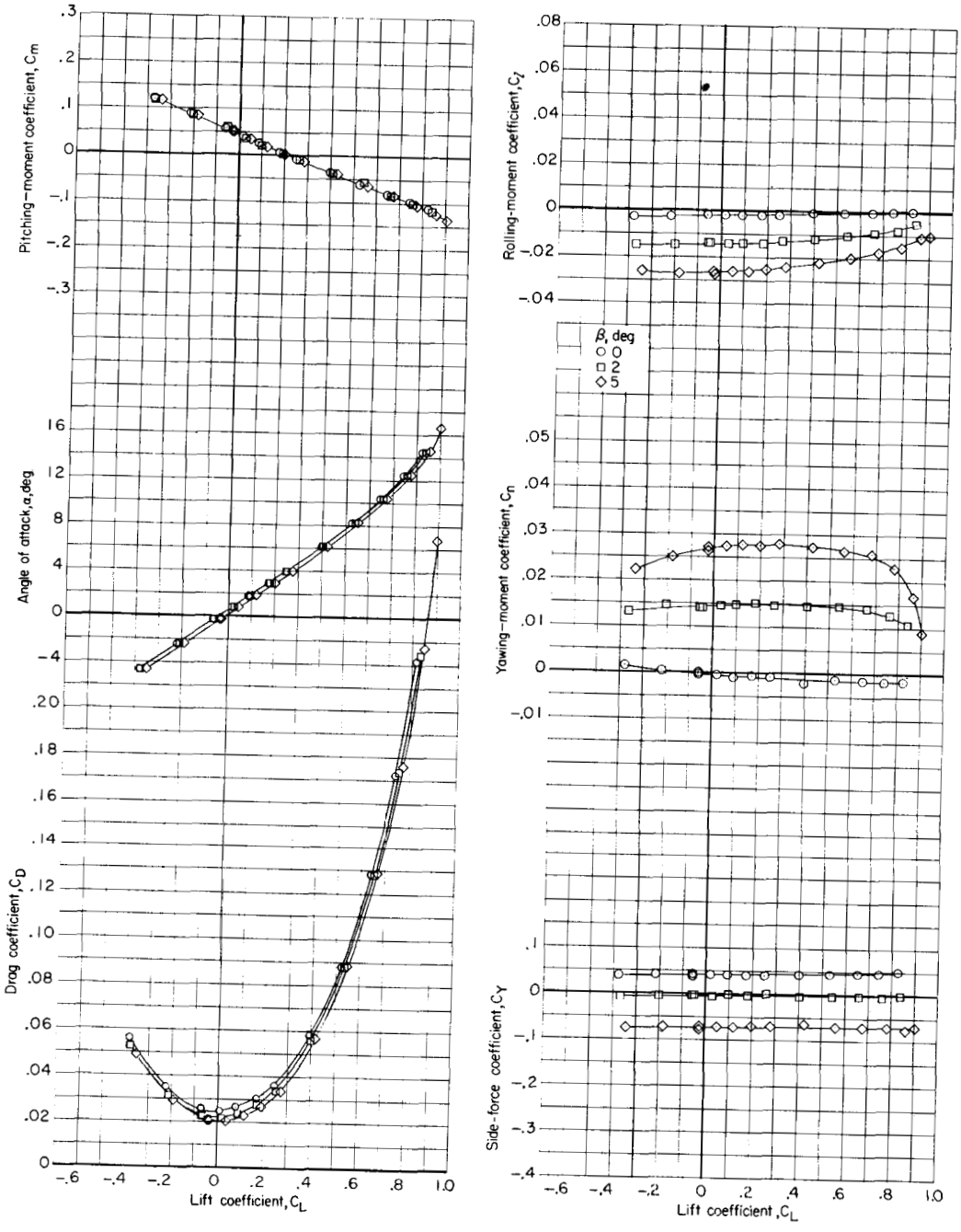

(a) M = 0.60; stagnation pressure, 0.5 atm.

Figure 19.- Effects of sideslip on aerodynamic characteristics in pitch of basic model. Transition natural; $i_t = -2.5^o$.

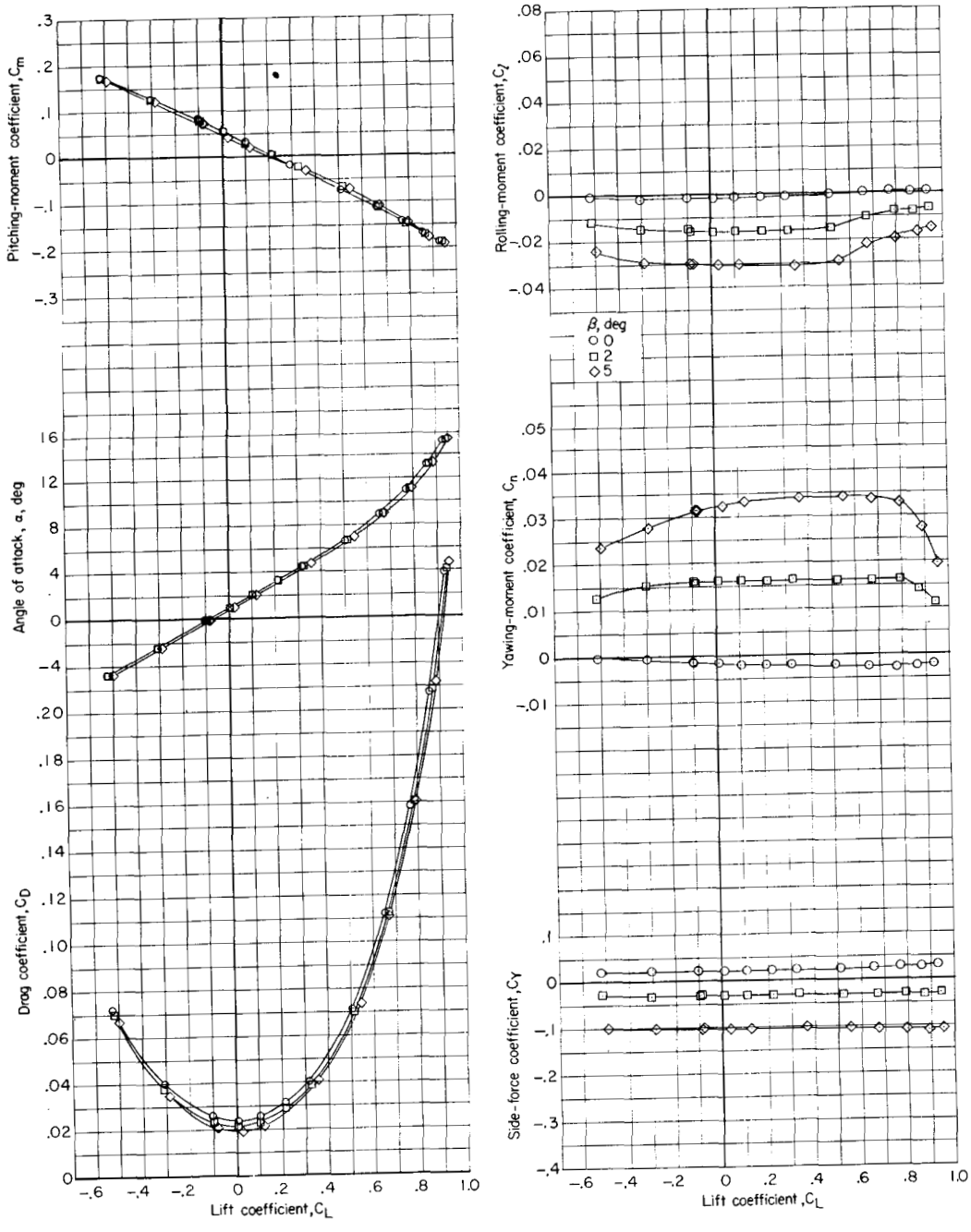

(b) M = 0.90; stagnation pressure, 0.5 atm.

Figure 19.- Continued.

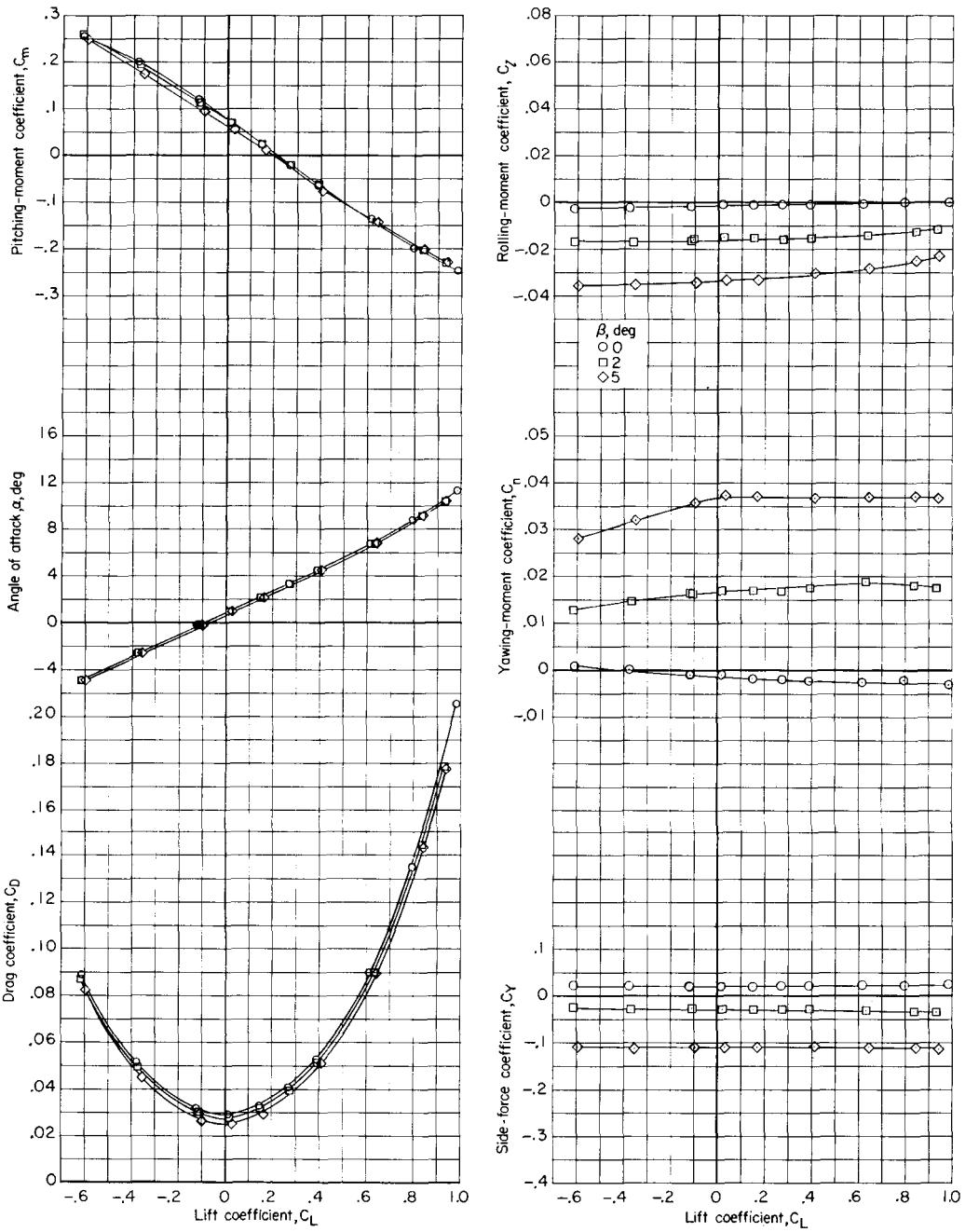

(c) M = 0.98; stagnation pressure, 0.5 atm.

Figure 19.- Continued.

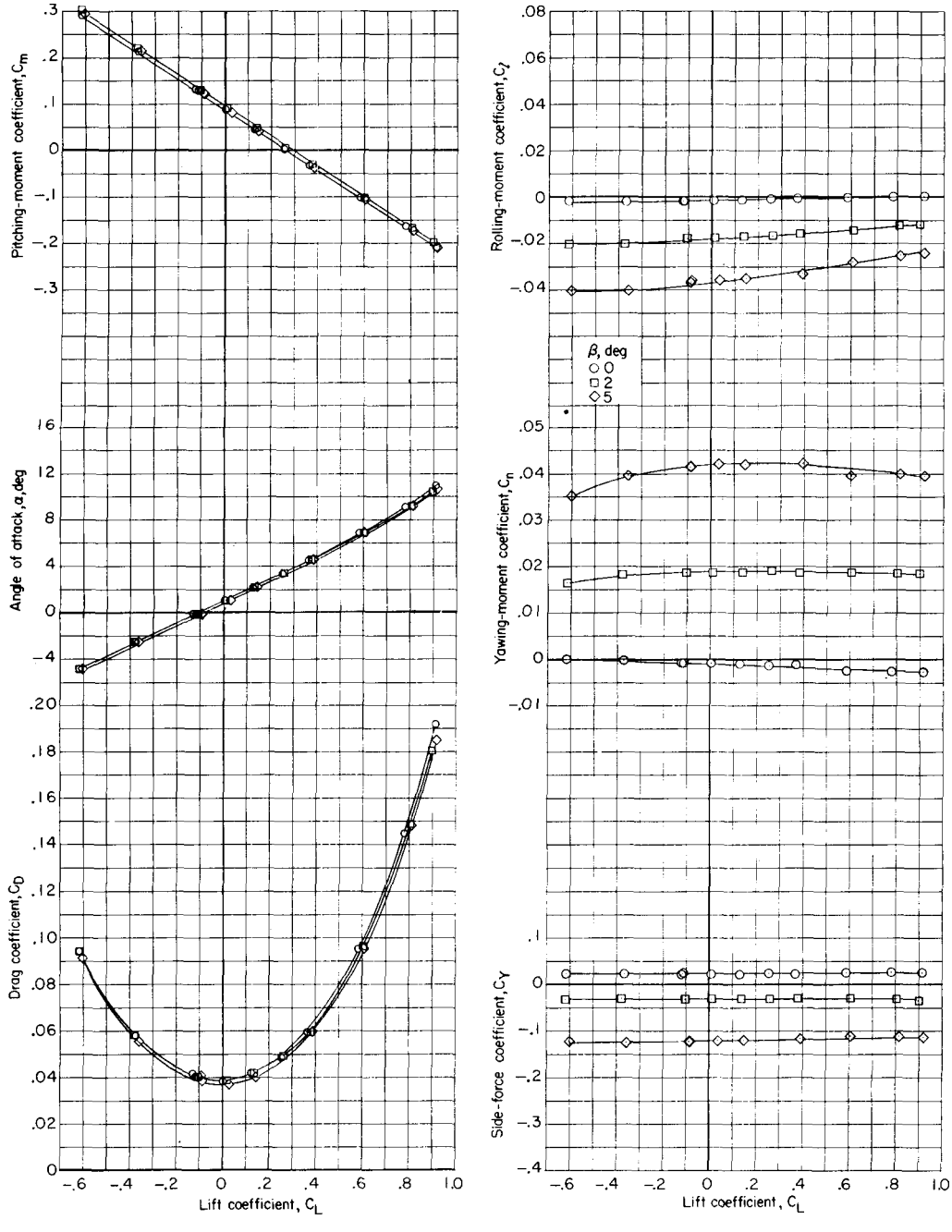

(d) M = 1.03; stagnation pressure, 0.5 atm.

Figure 19.- Continued.

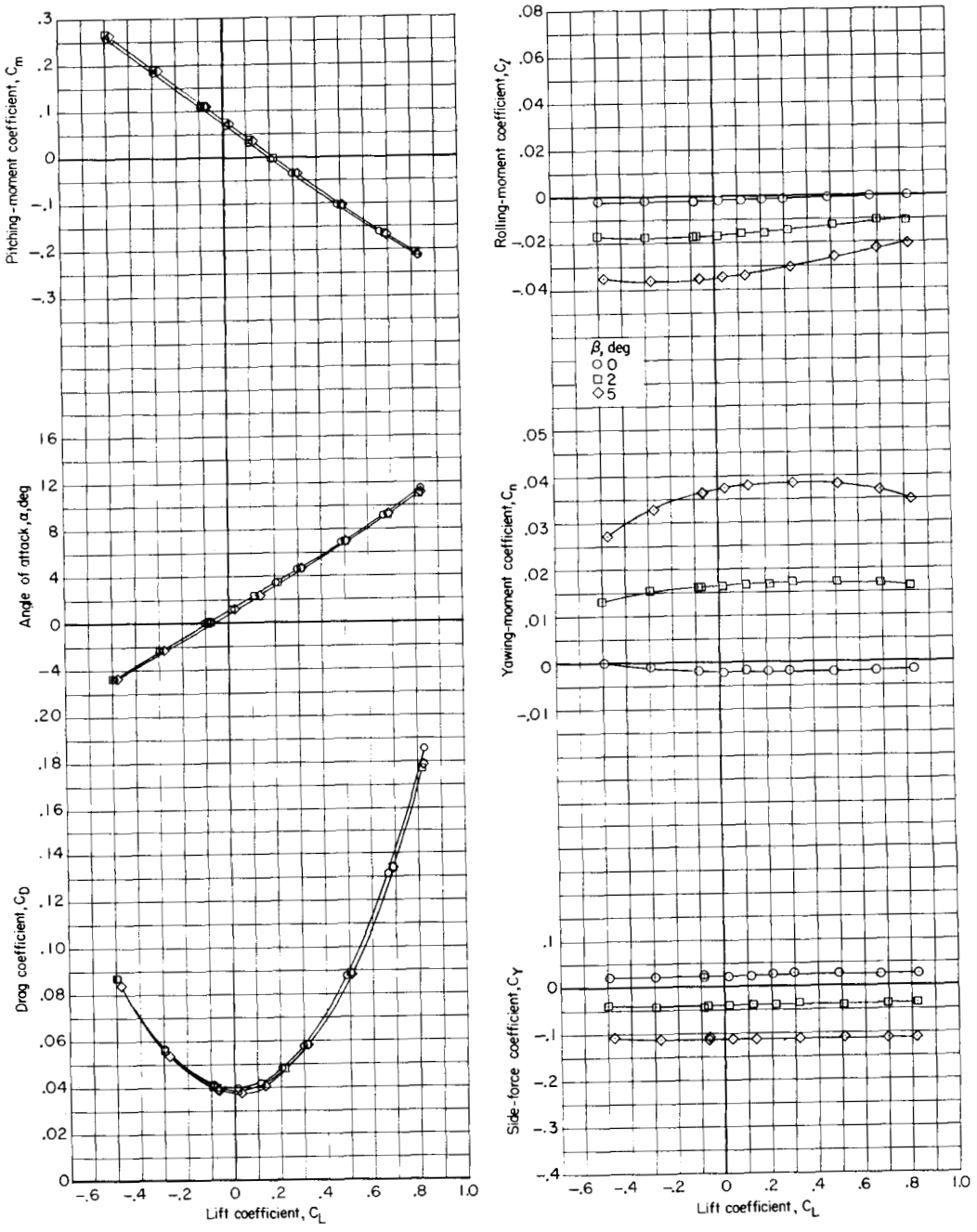

(e) M = 1.20; stagnation pressure, 0.5 atm.

Figure 19.- Continued.

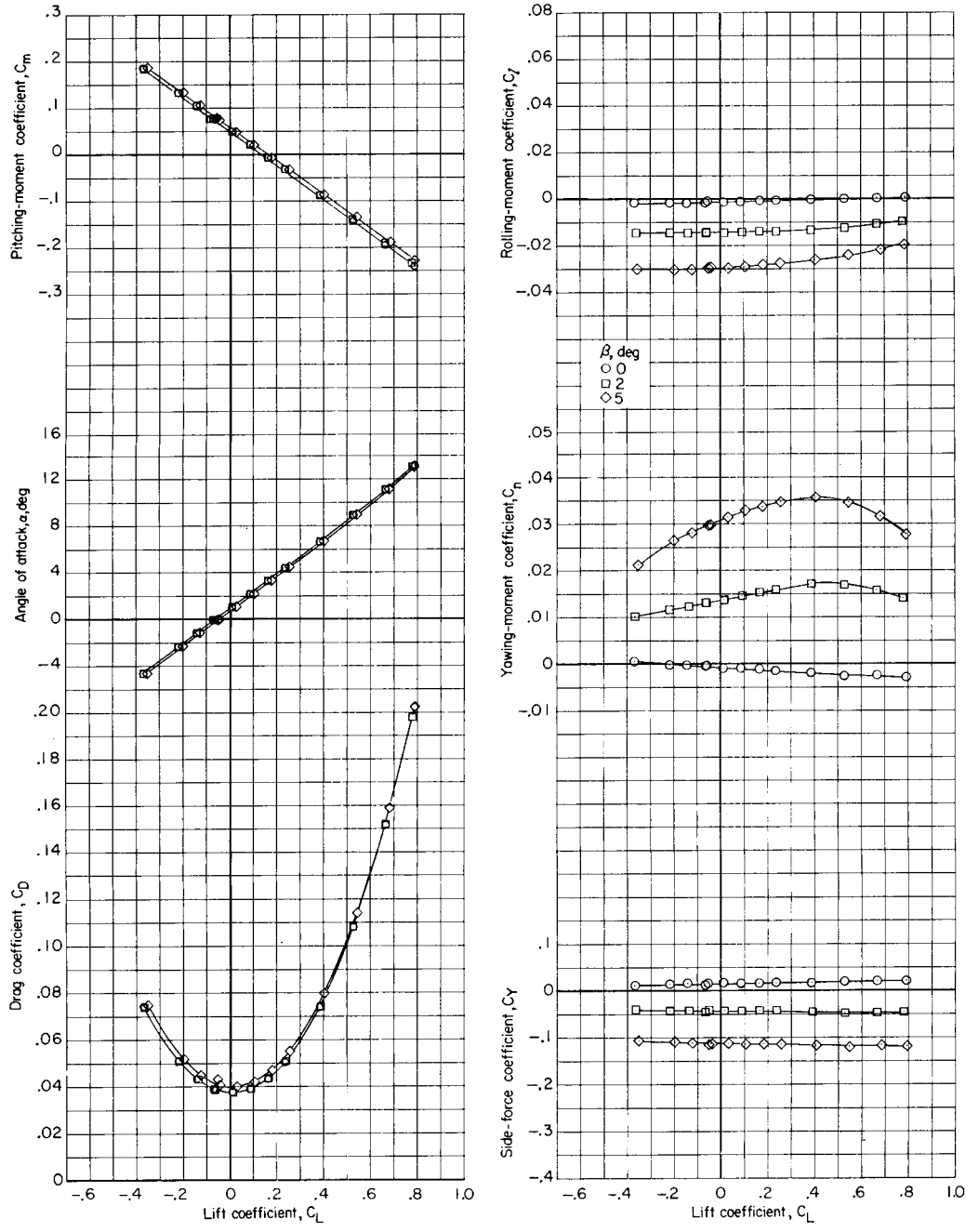

(f) M = 1.42; stagnation pressure, 0.5 atm.

Figure 19.- Continued.

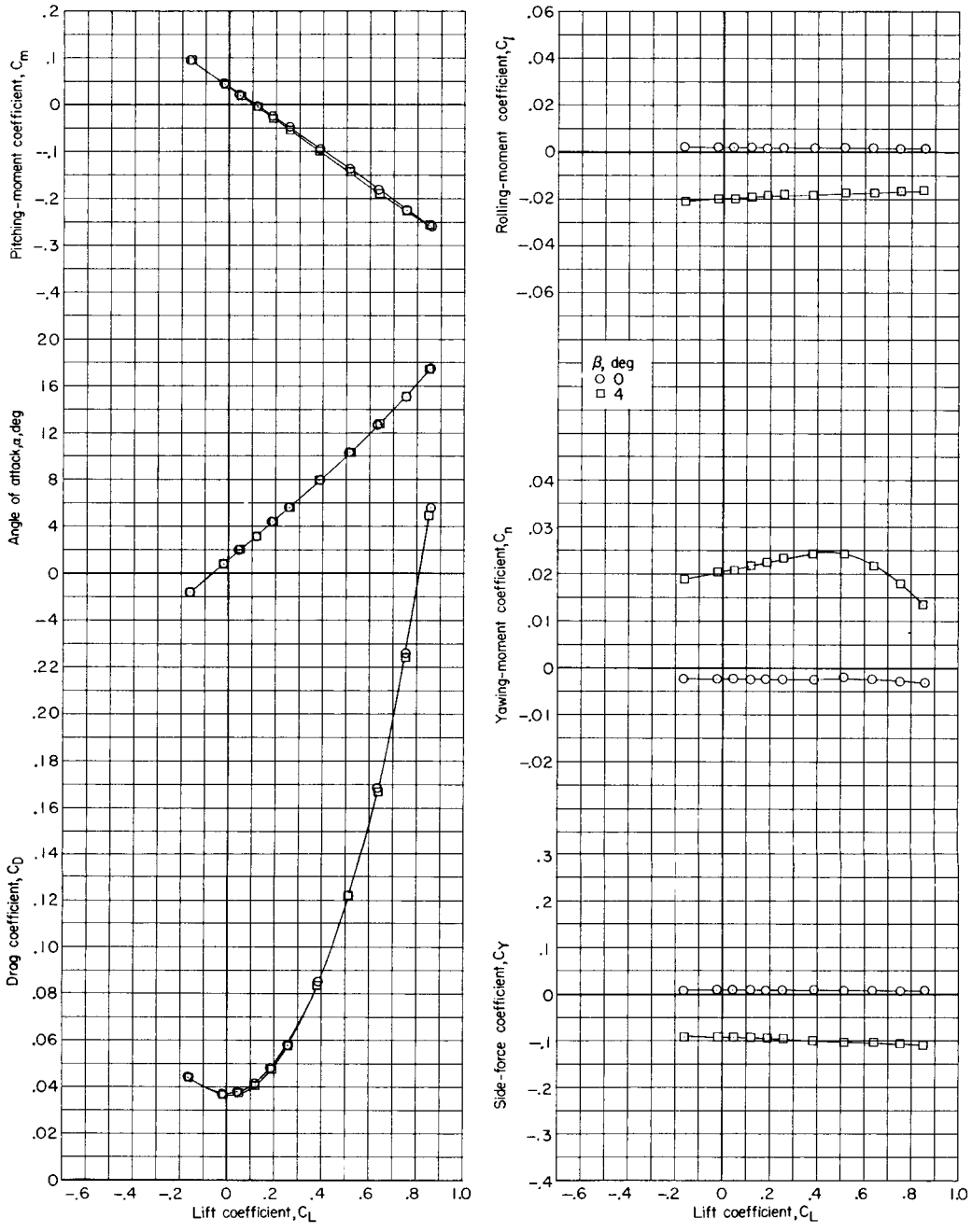

(g) M = 1.57; stagnation pressure, 0.68 atm.

Figure 19.- Continued.

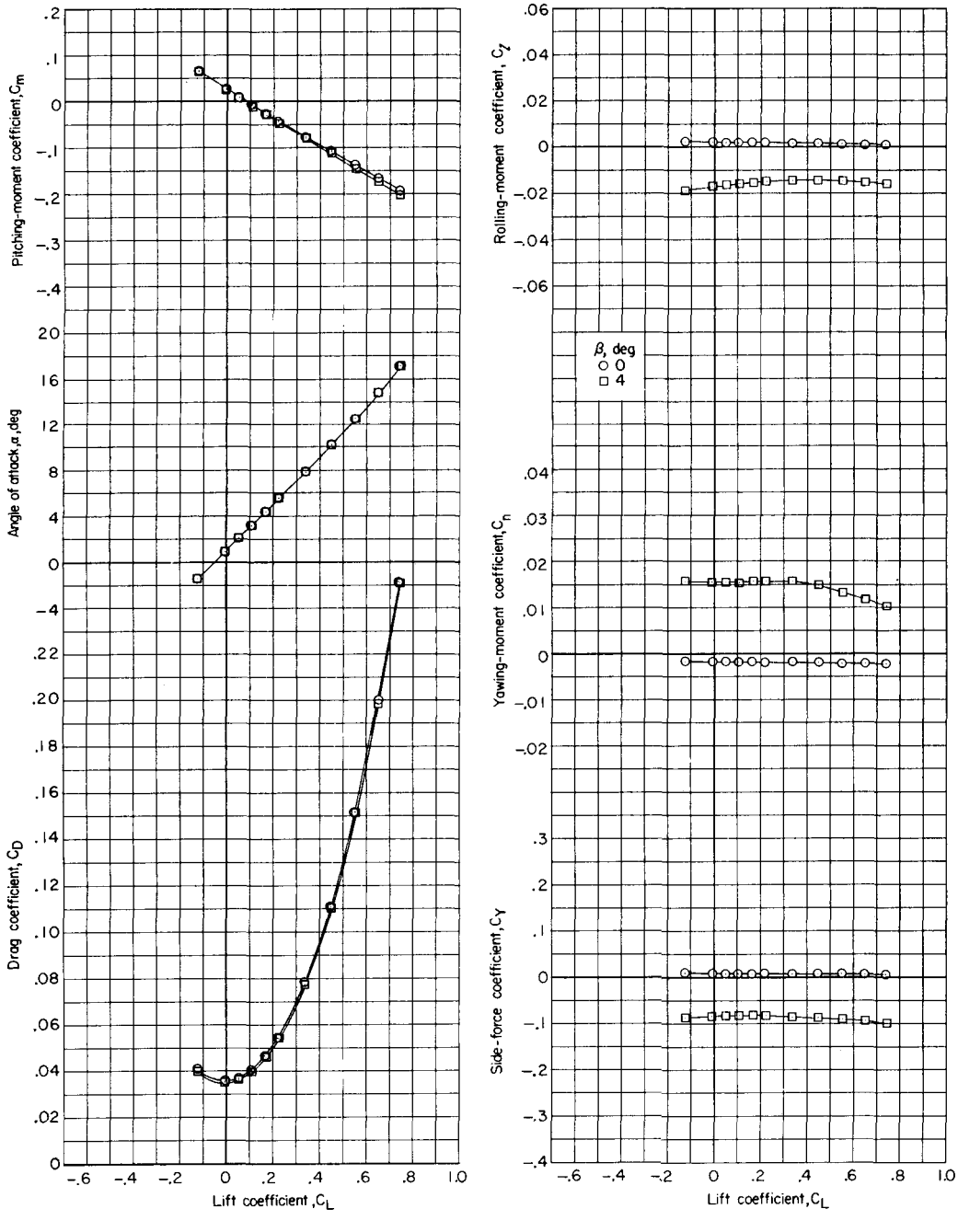

(h) M = 1.77; stagnation pressure, 0.68 atm.

Figure 19.- Continued.

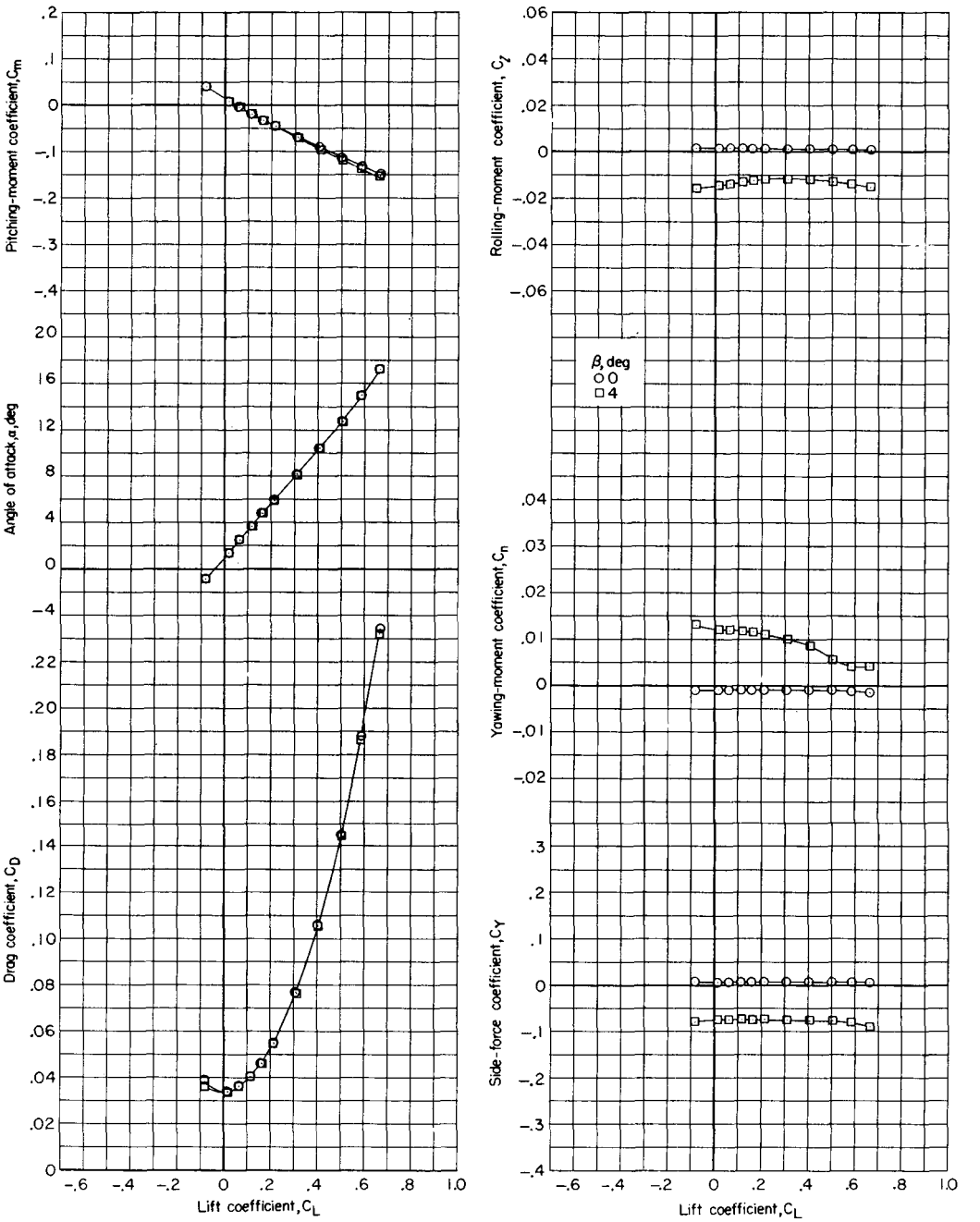

(i) M = 1.97; stagnation pressure, 0.68 atm.

Figure 19.- Continued.

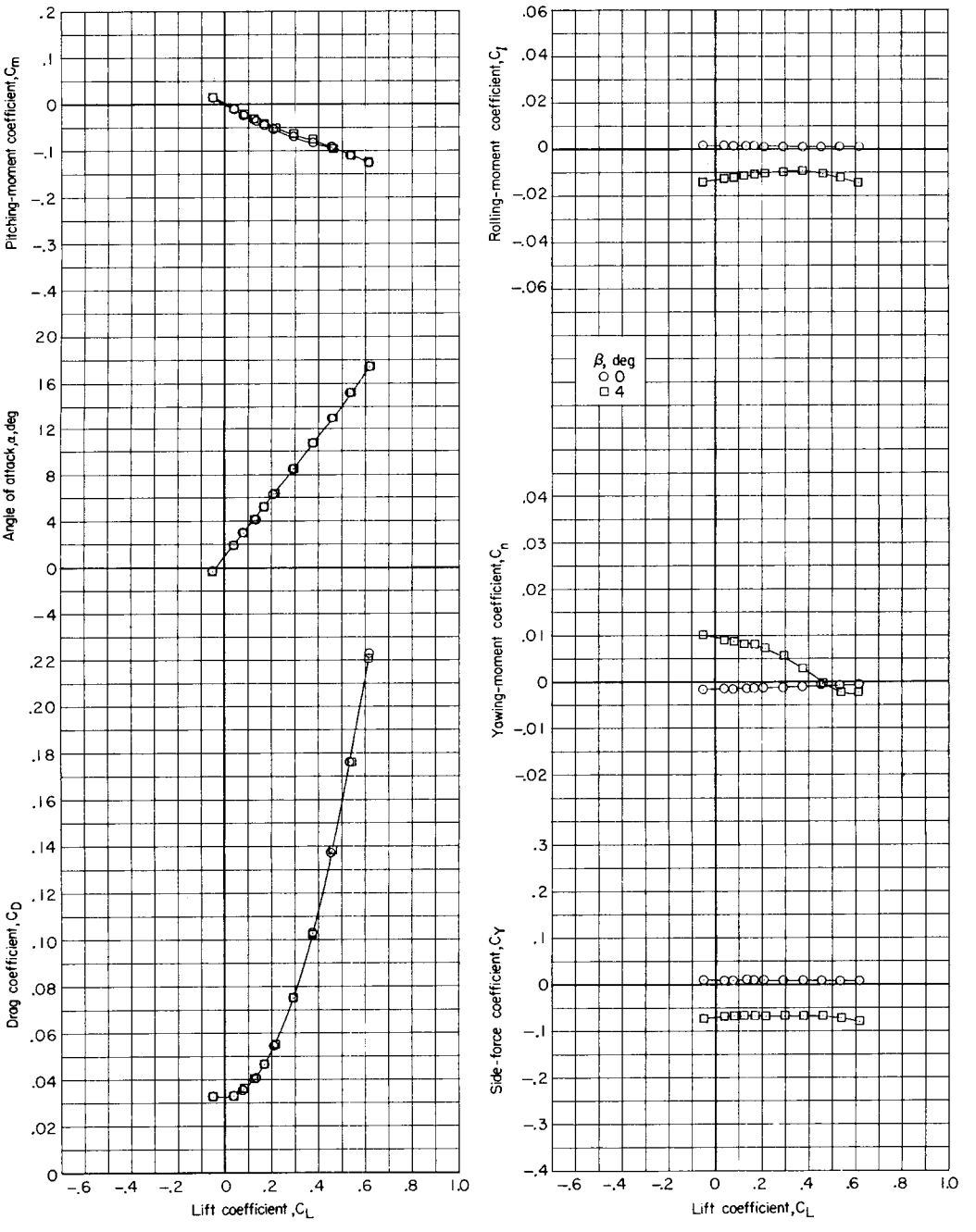

(j) M = 2.20; stagnation pressure, 0.68 atm.

Figure 19.- Concluded.

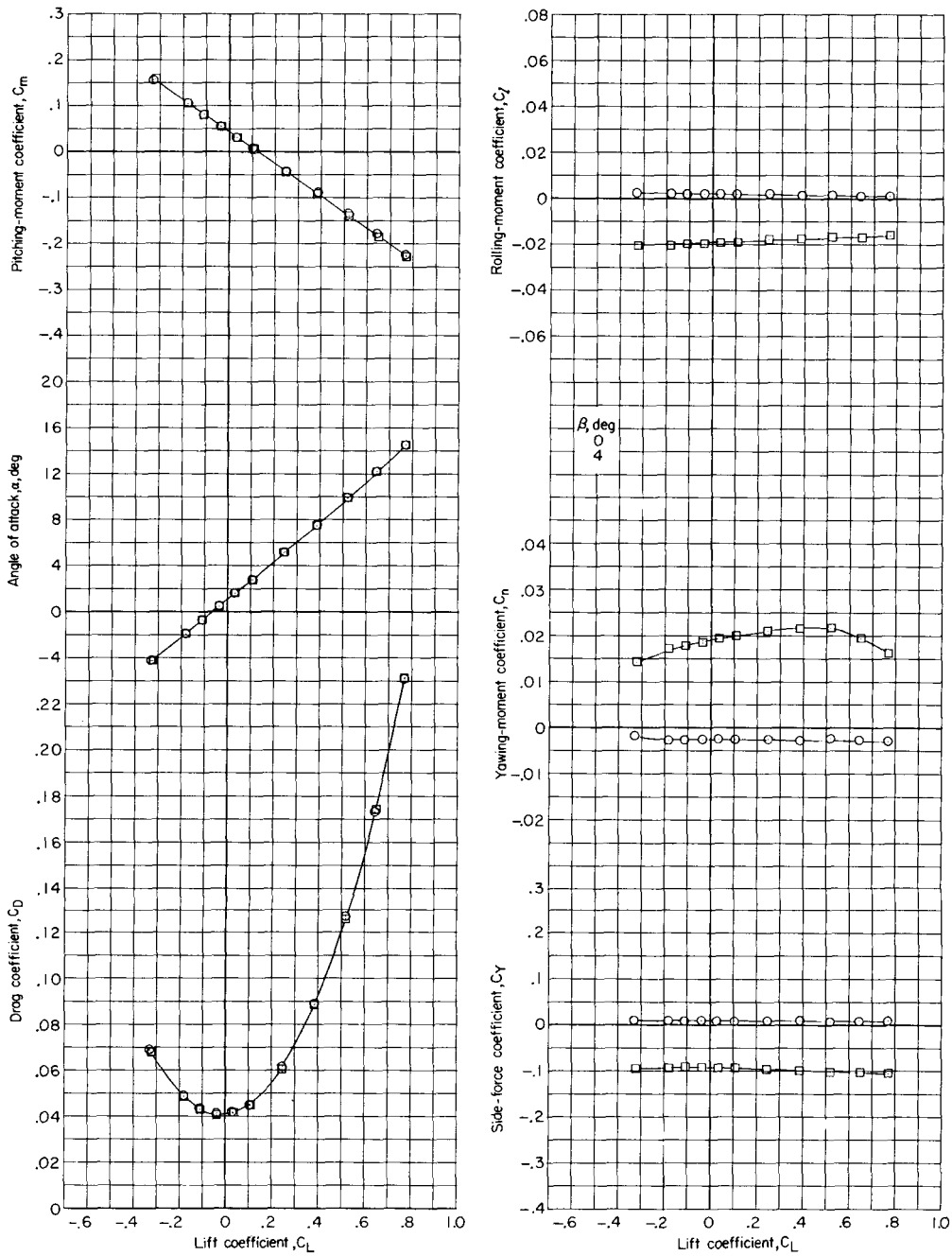

(a) M = 1.57.

Figure 20.- Effects of sideslip on aerodynamic characteristics of basic model plus wingtip floats. Natural transition; stagnation pressure, 0.68; $i_t = -2.5^\circ$.

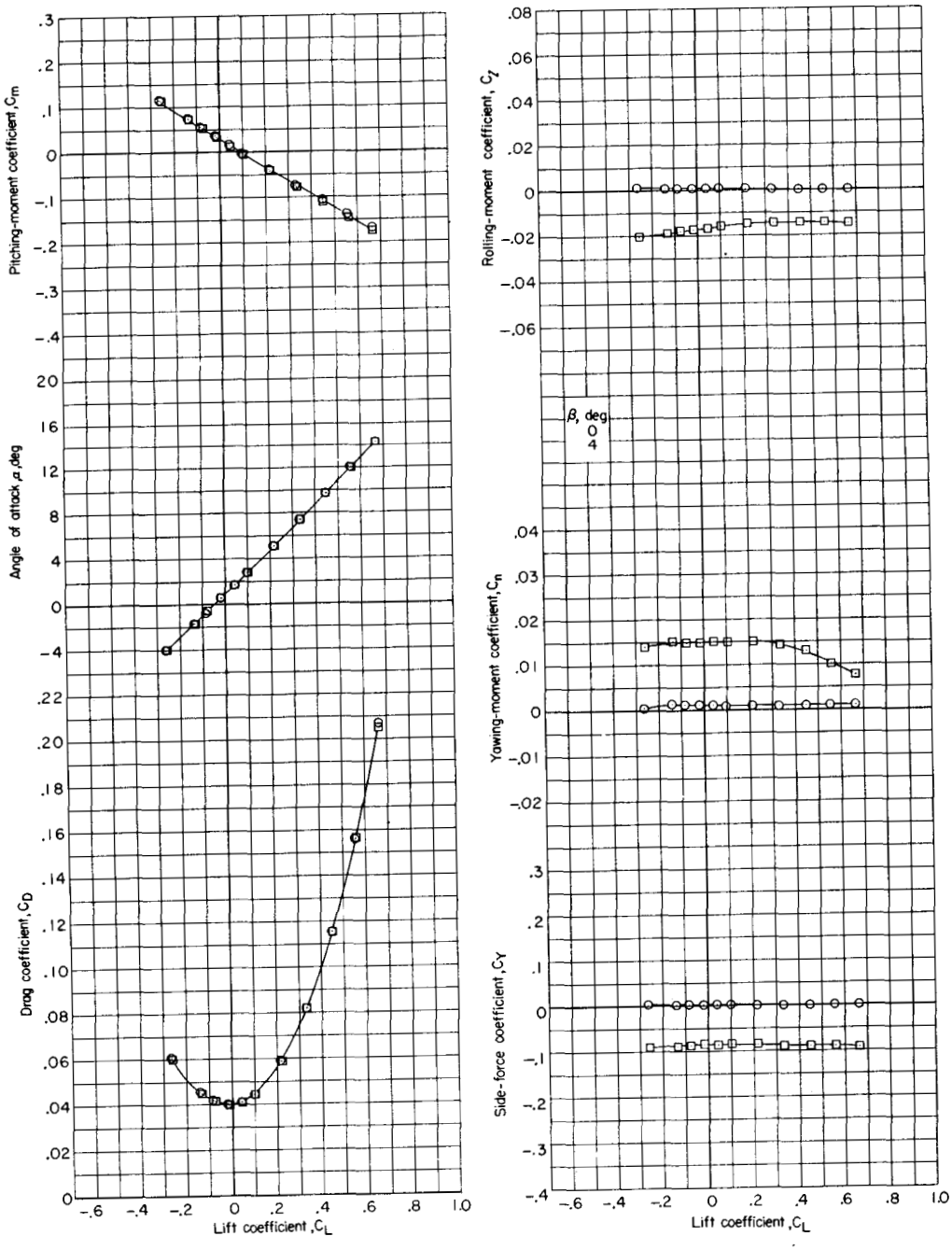

(b) M = 1.77.

Figure 20.- Continued.

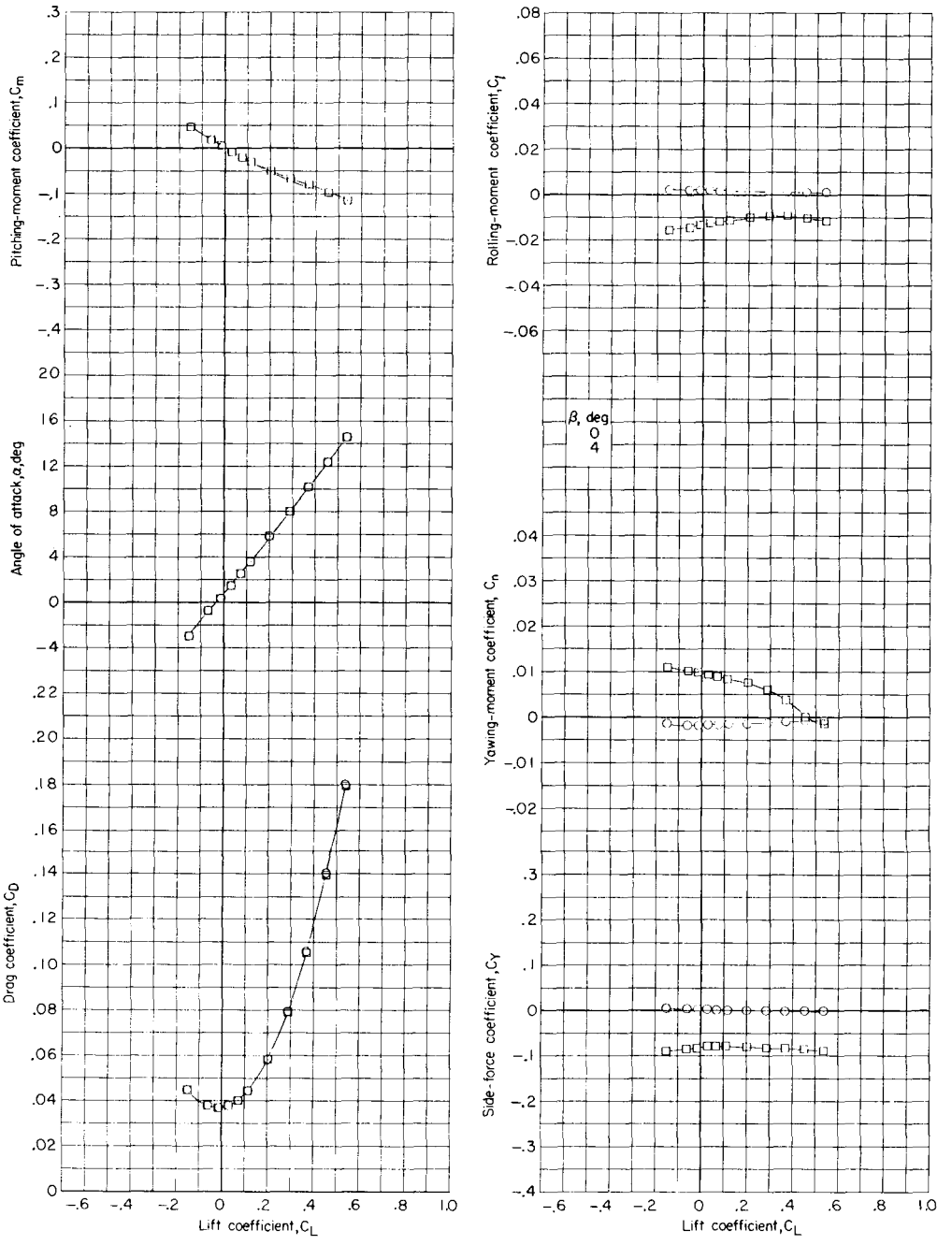

(c) M = 2.20.

Figure 20.- Concluded.

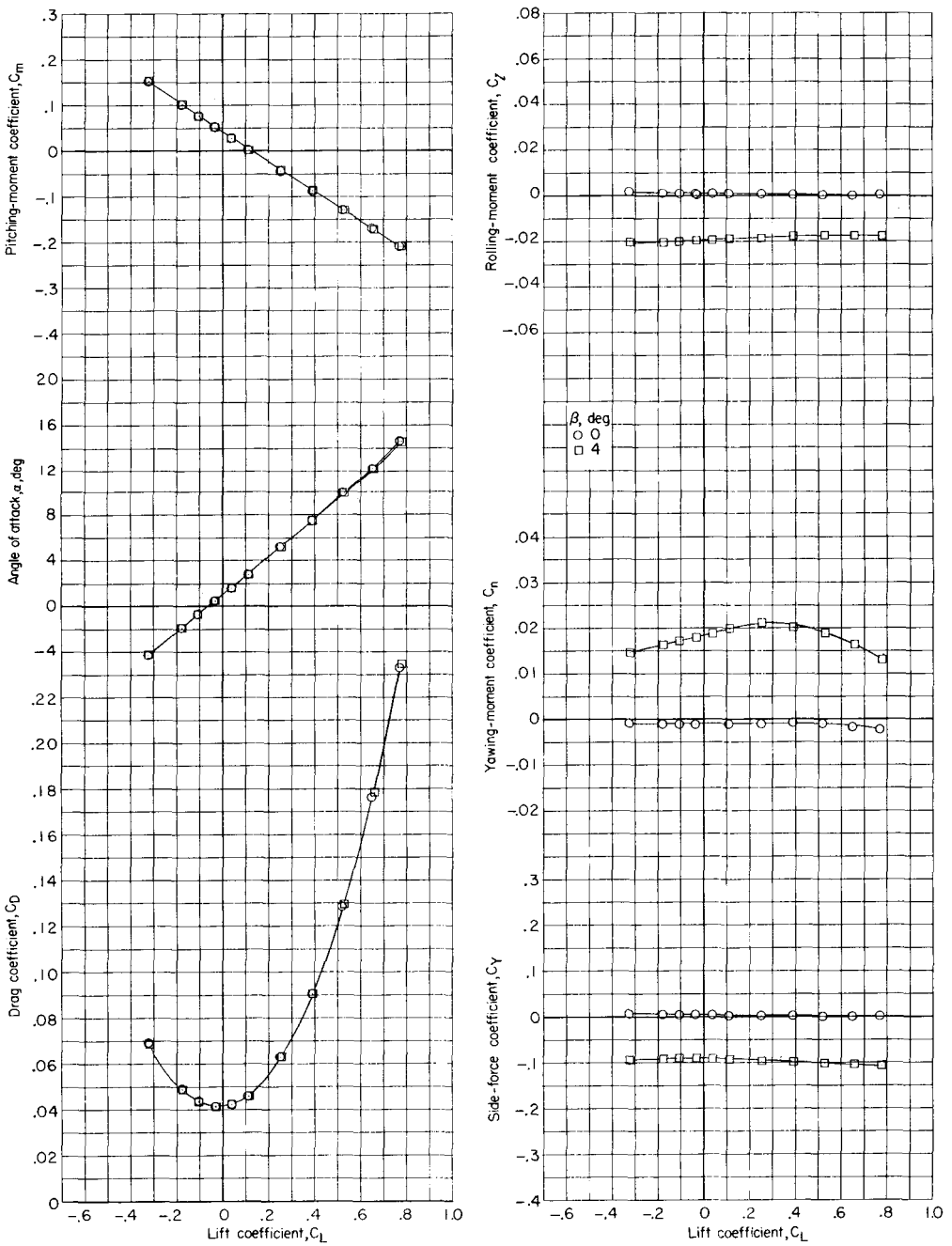

(a) M = 1.57.

Figure 21.- Effects of sideslip on aerodynamic characteristics in pitch of basic model plus wingtip floats, step fairing, and vertical chine strips.

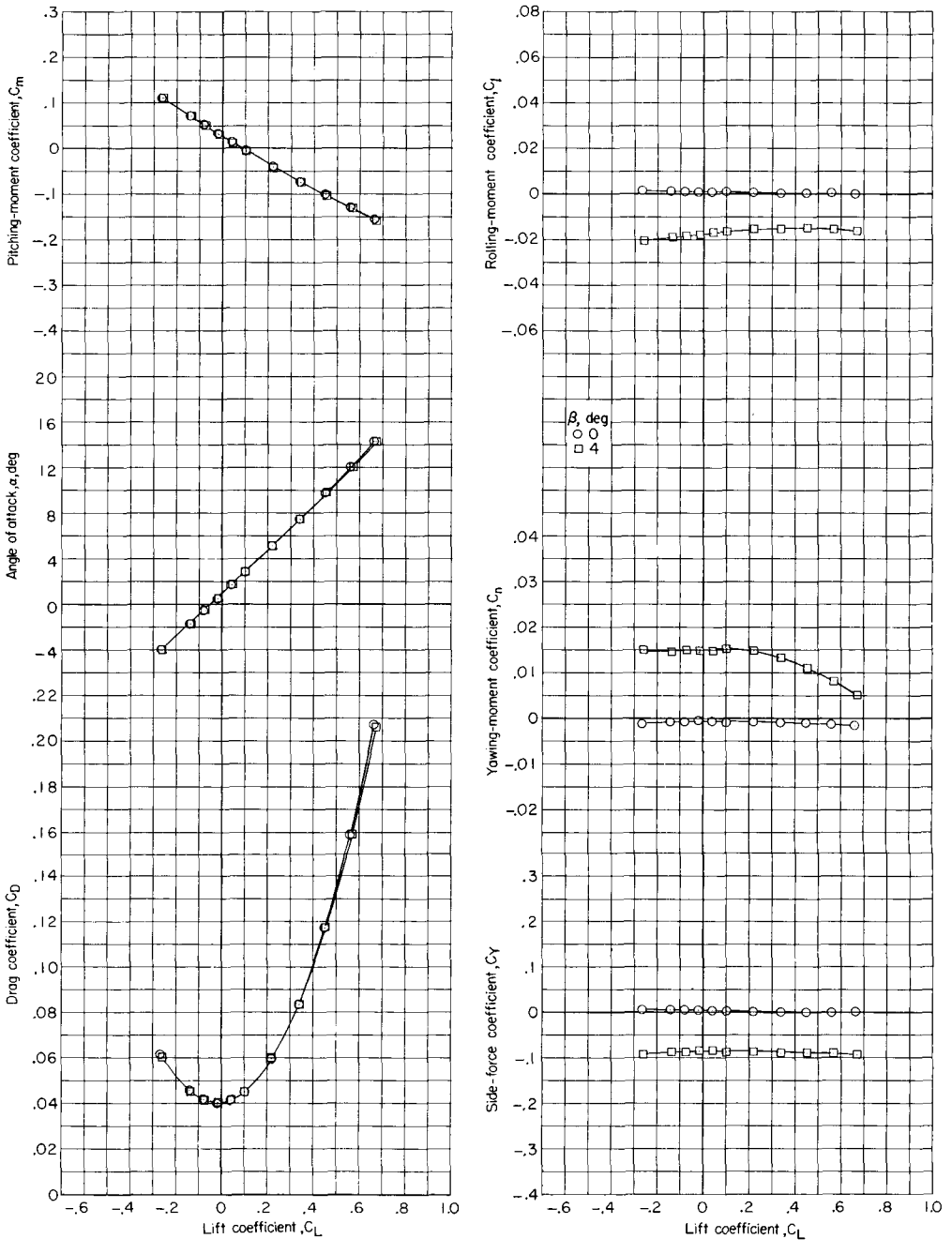

(b) M = 1.77.

Figure 21.- Continued.

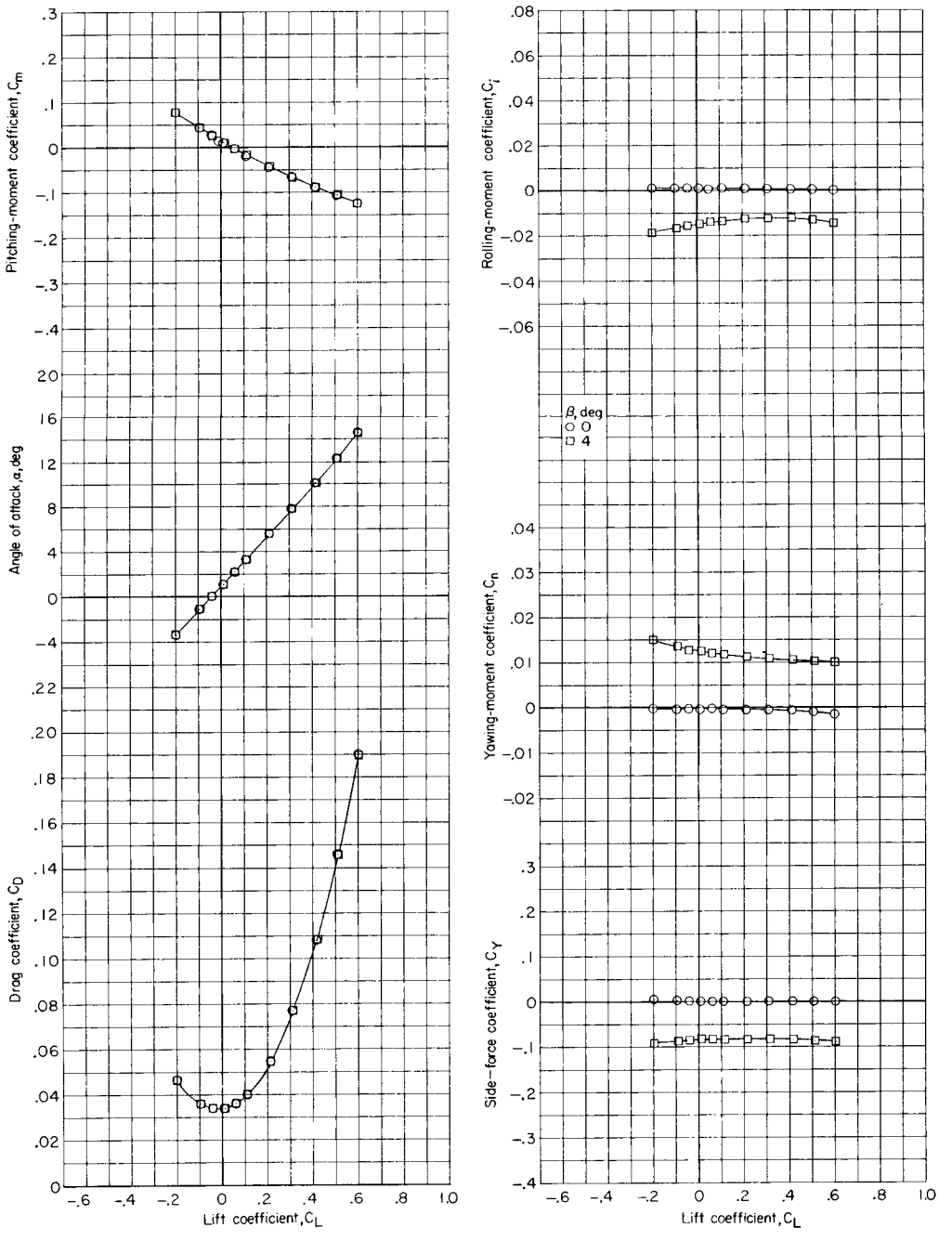

(c) M = 1.97.

Figure 21.- Continued.

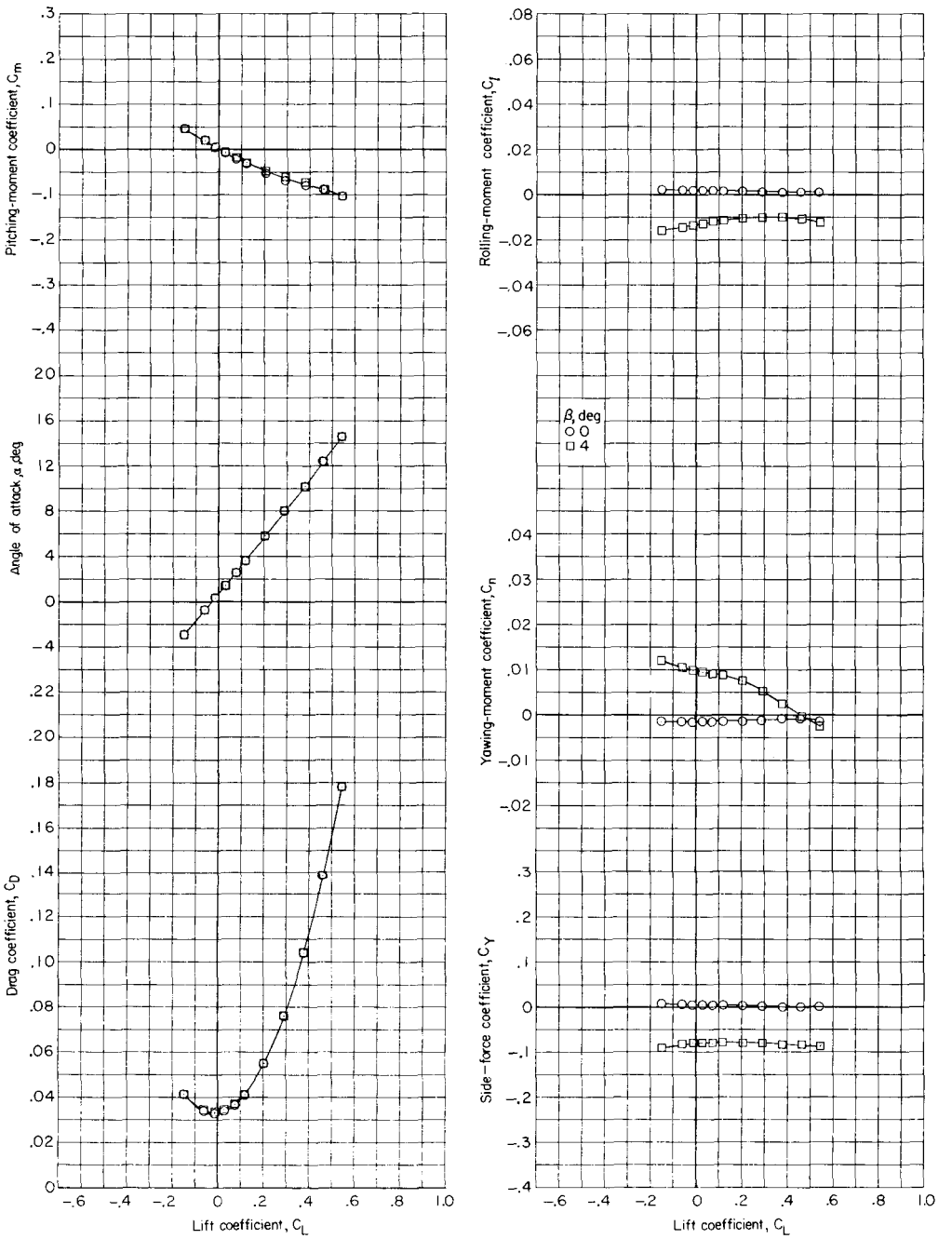

(d) M = 2.20.

Figure 21.- Concluded.

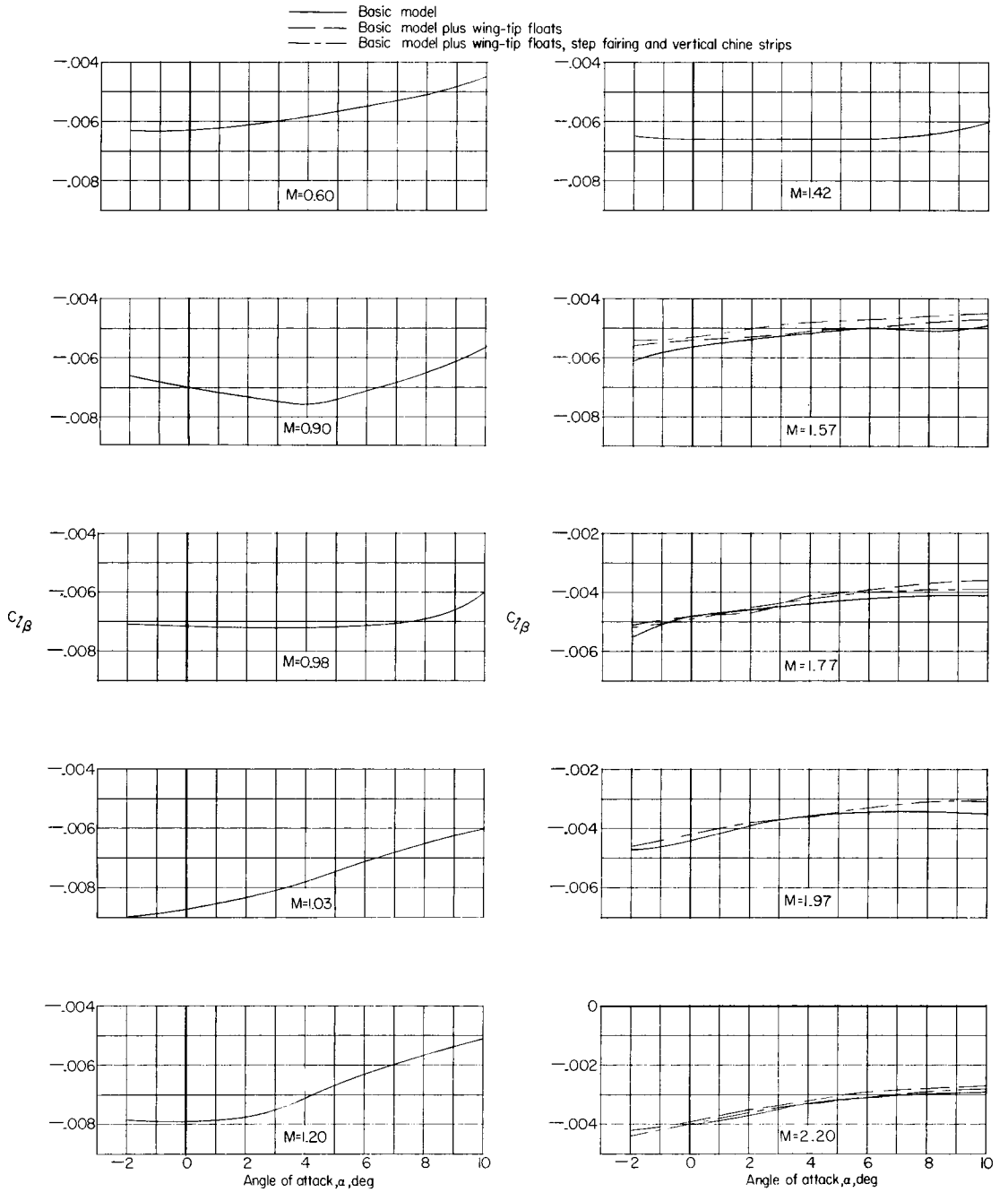

(a) Effective-dihedral derivative.

Figure 22.- Variation with angle of attack of the lateral-stability derivatives.

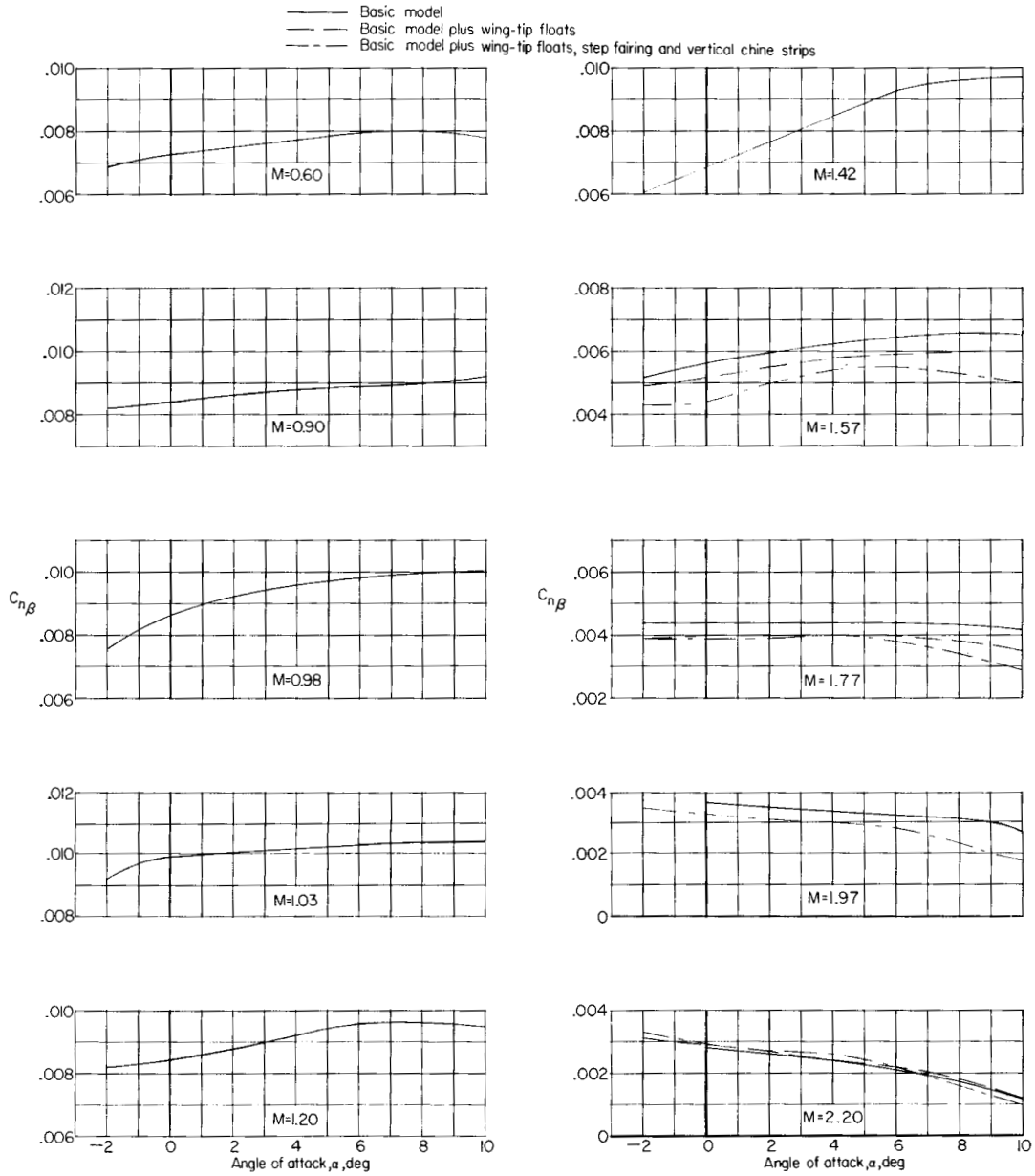

(b) Directional-stability derivative.

Figure 22.- Continued.

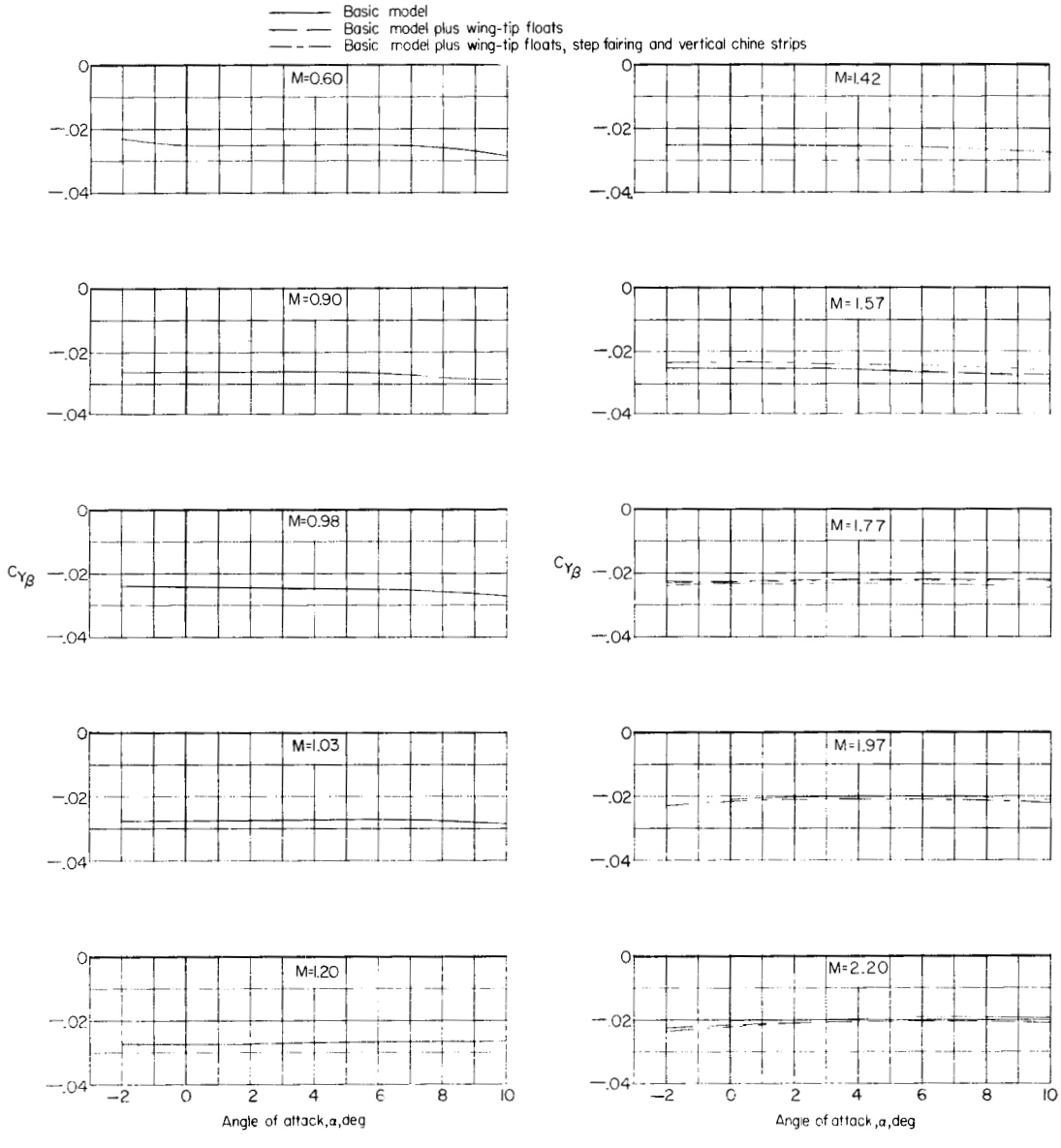

(c) Lateral-force derivative.

Figure 22.- Concluded.

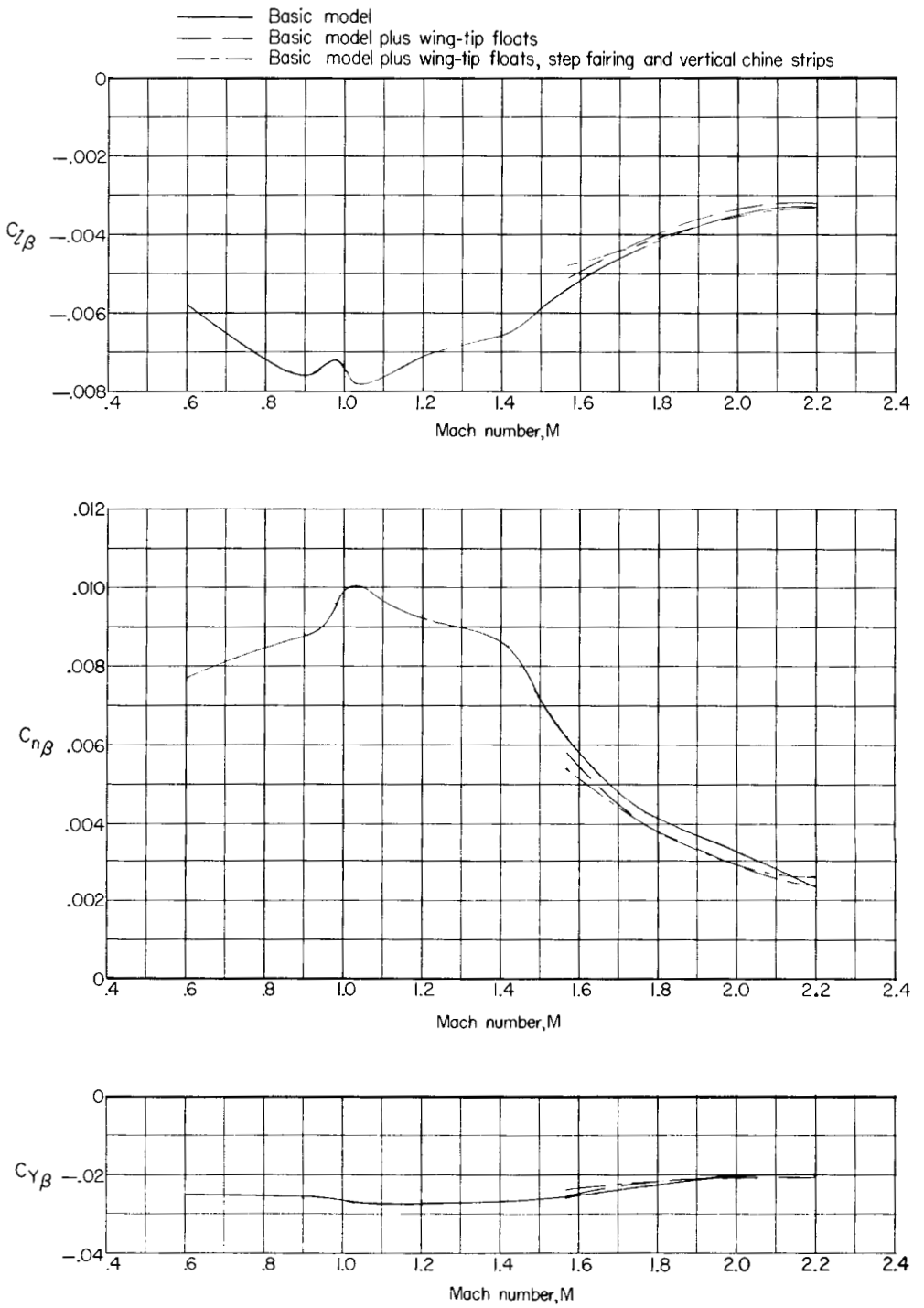

Figure 23.- Variation with Mach number of the lateral-stability derivatives. $\alpha \approx 4^\circ$.

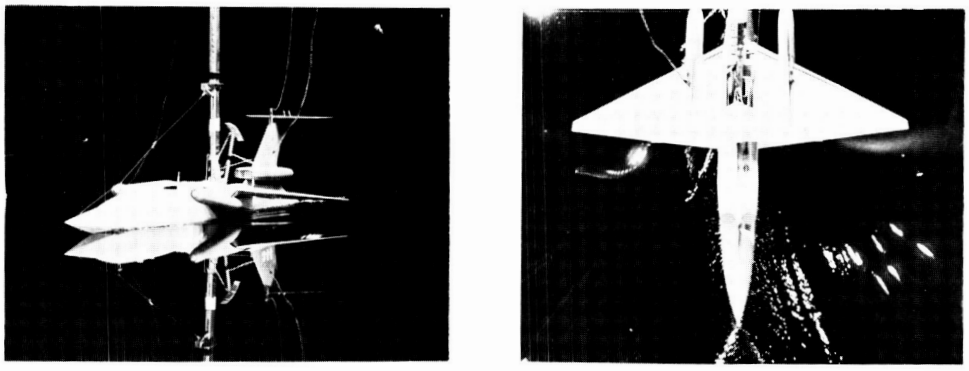

(a) Speed, 13.2 knots.

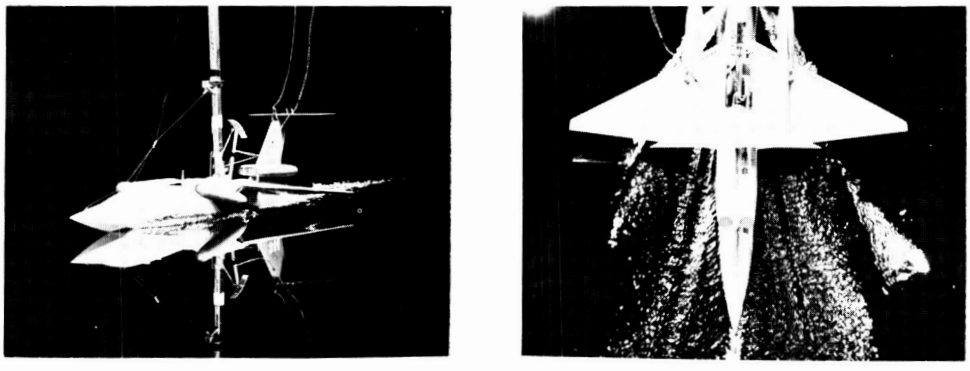

(b) Speed, 26.5 knots.

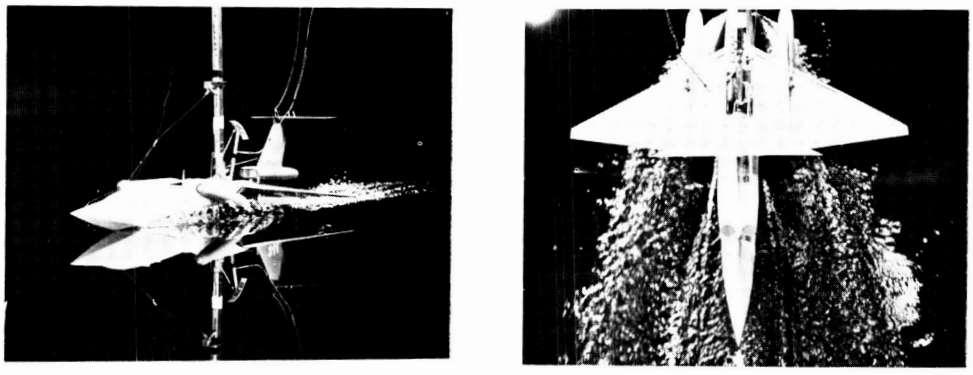

(c) Speed, 39.7 knots. L-59-8207

Figure 24.- Spray photographs of model with power off. Gross load, 225,000 pounds. δ_e, -2.5°; δ_s, -5°.

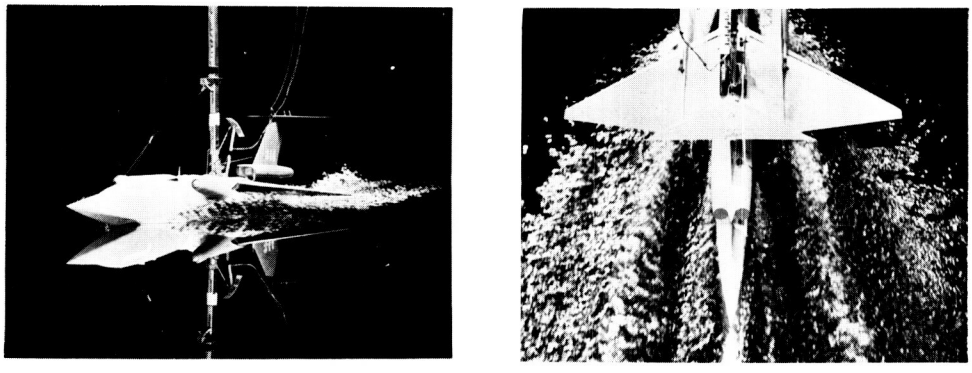

(d) Speed, 47 knots.

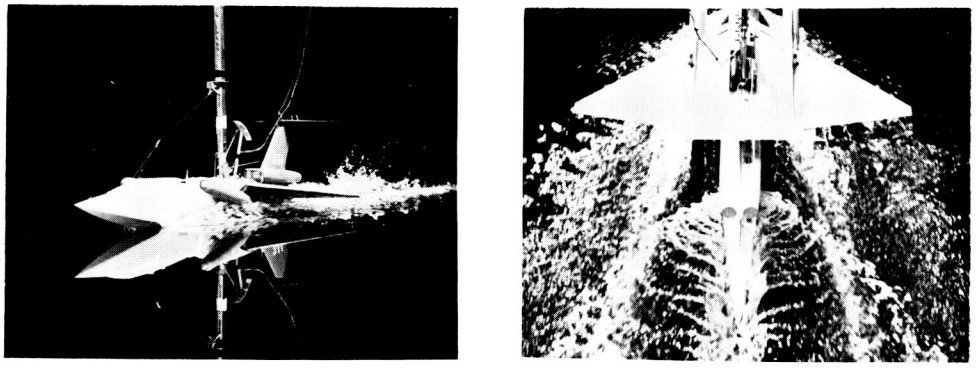

(e) Speed, 53.8 knots.

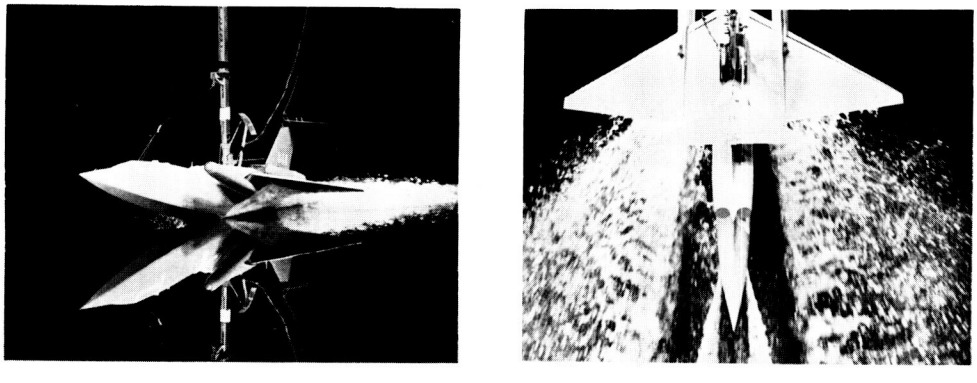

(f) Speed, 80.5 knots. L-59-8208

Figure 24.- Continued.

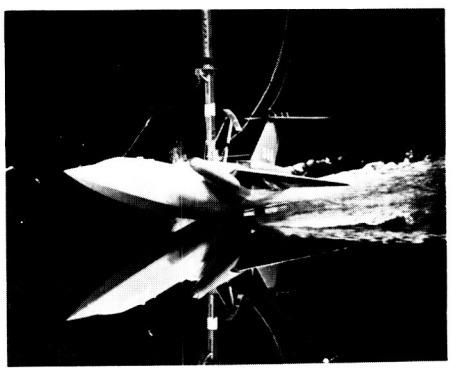
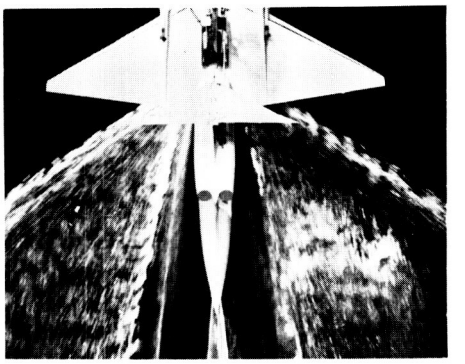

(g) Speed, 134.5 knots.

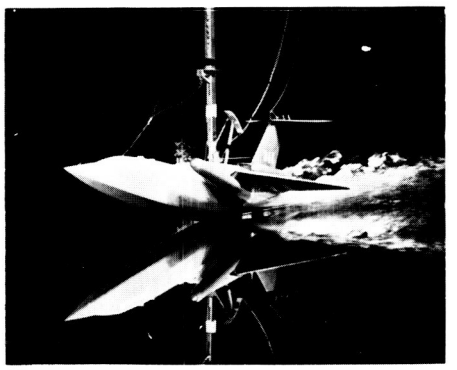
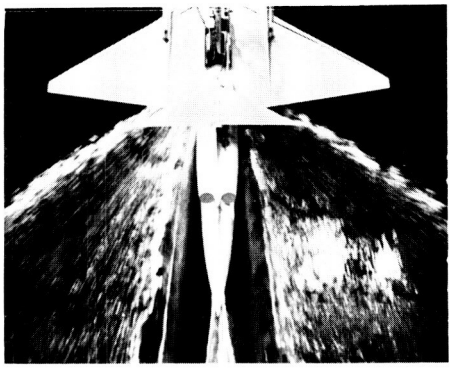

(h) Speed, 143.8 knots.

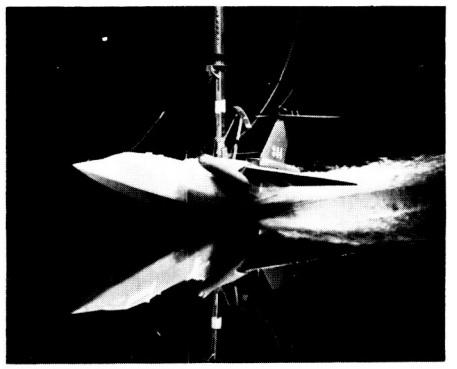
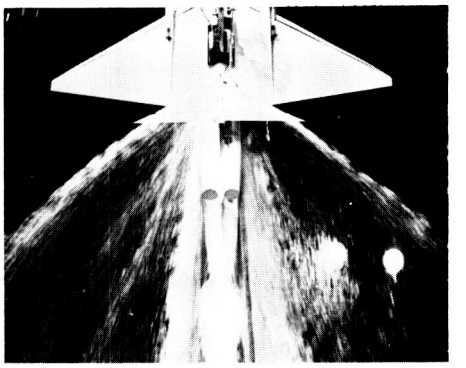

(i) Speed, 162.9 knots. L-59-8209

Figure 24.- Concluded.

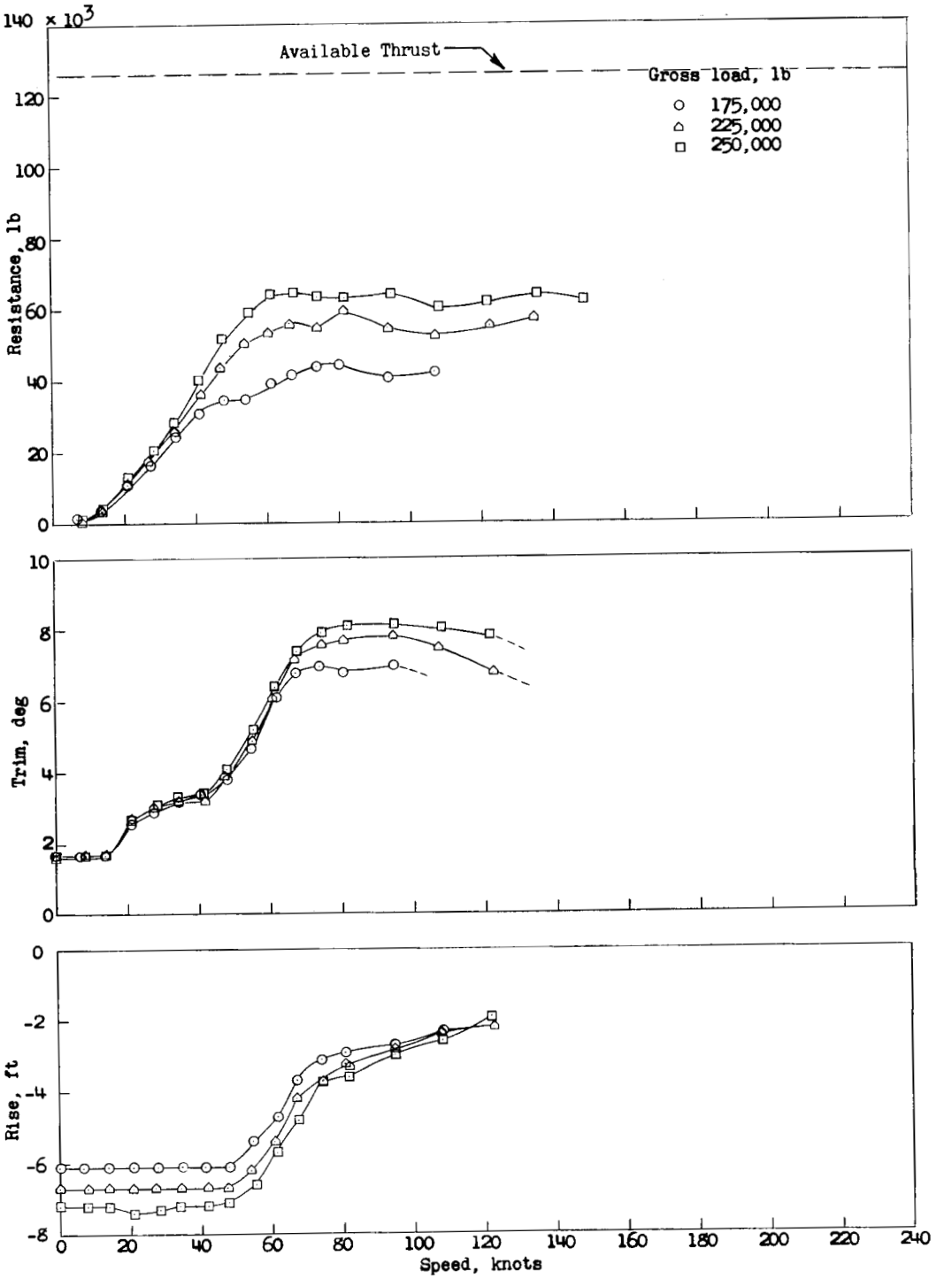

Figure 25.- Effect of gross load upon the resistance, trim, and rise. $\delta_s = -2.5^\circ$; $\delta_e = -5^\circ$.

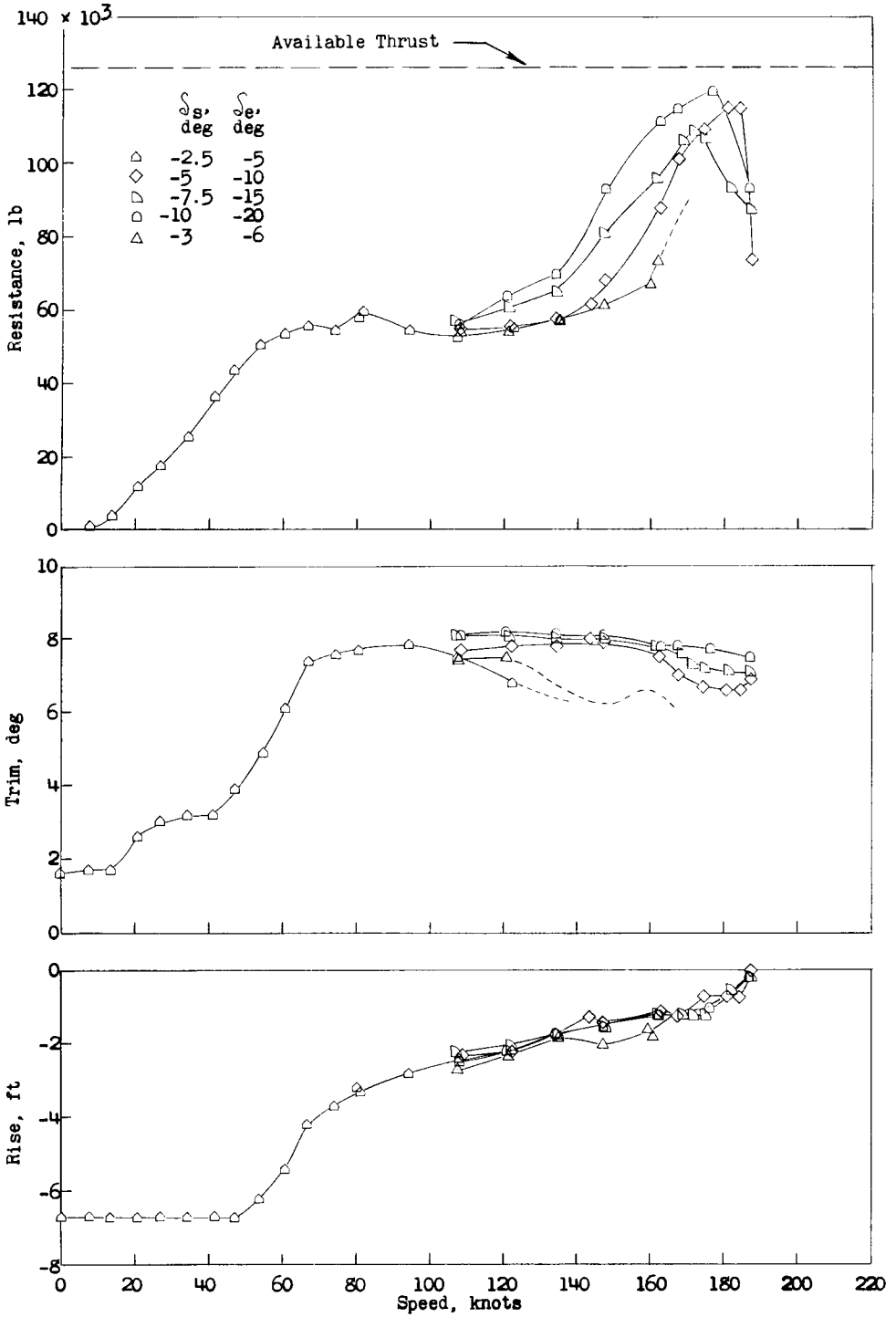

Figure 26.- Effect of stabilizer-elevator setting upon resistance, trim, and rise. Gross load, 225,000 pounds.

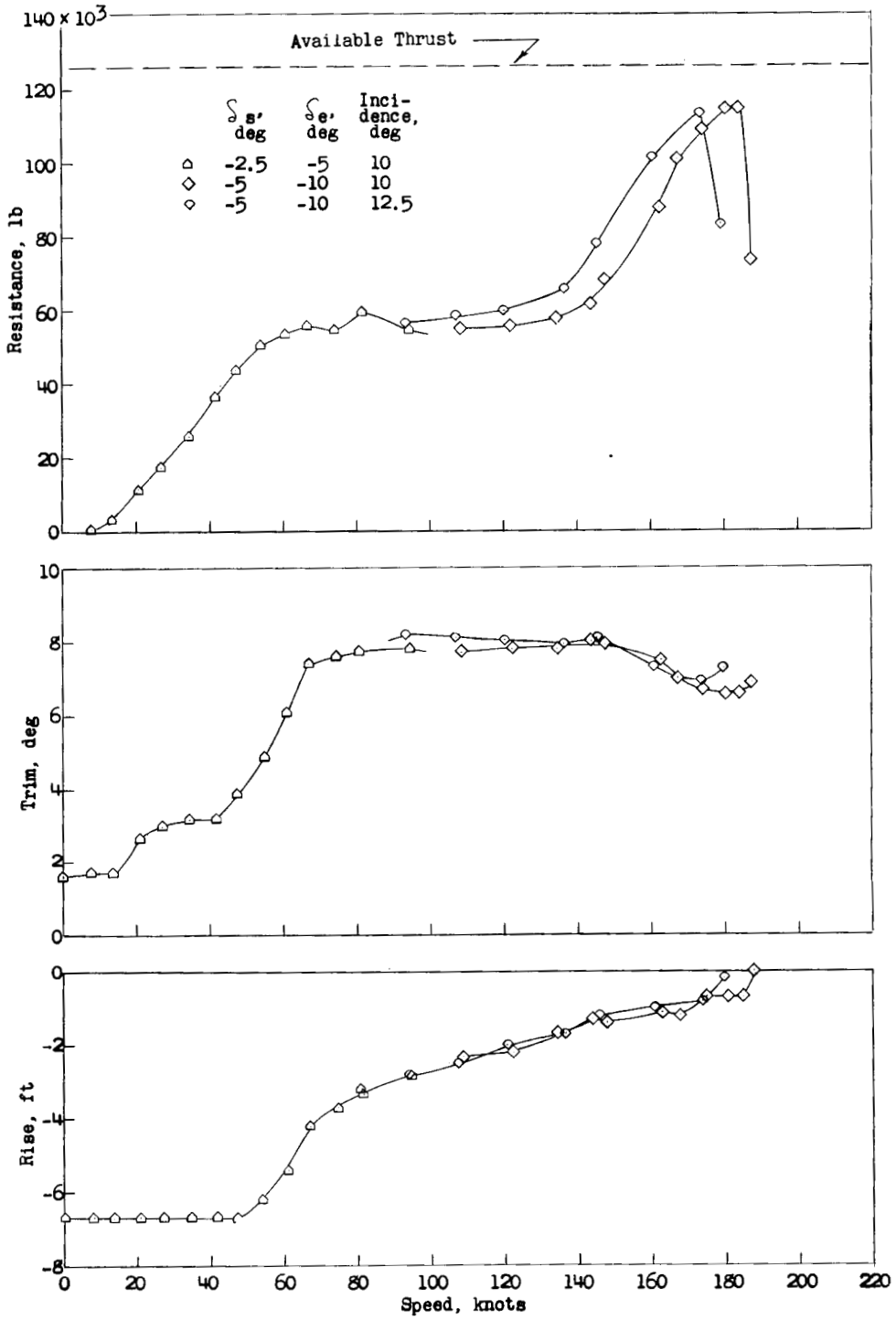

Figure 27.- Effect of wing incidence upon resistance, trim, and rise. Gross load, 225,000 pounds.

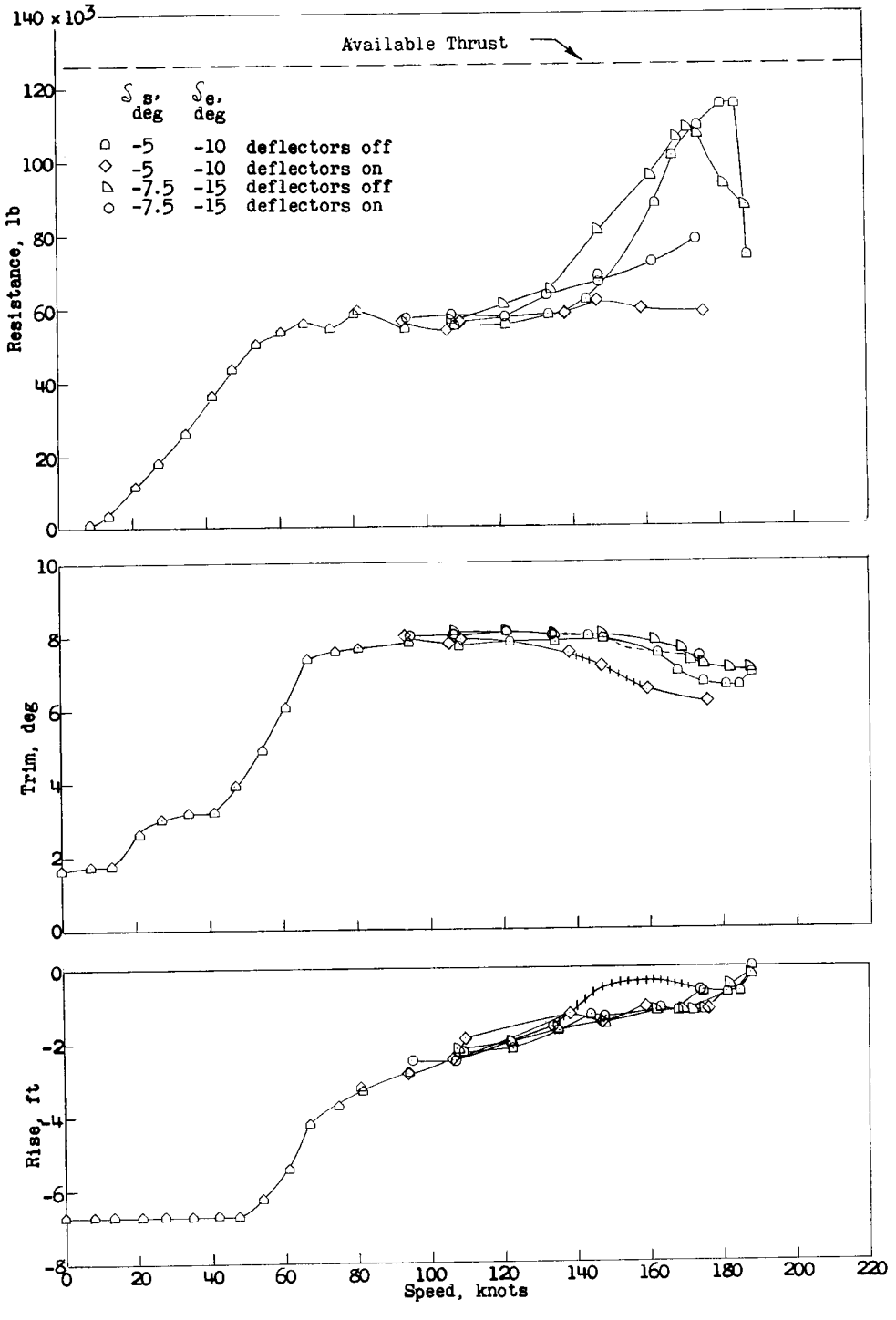

Figure 28.- Effect of afterbody flow deflectors upon resistance, trim, and rise. Gross load, 225,000 pounds.

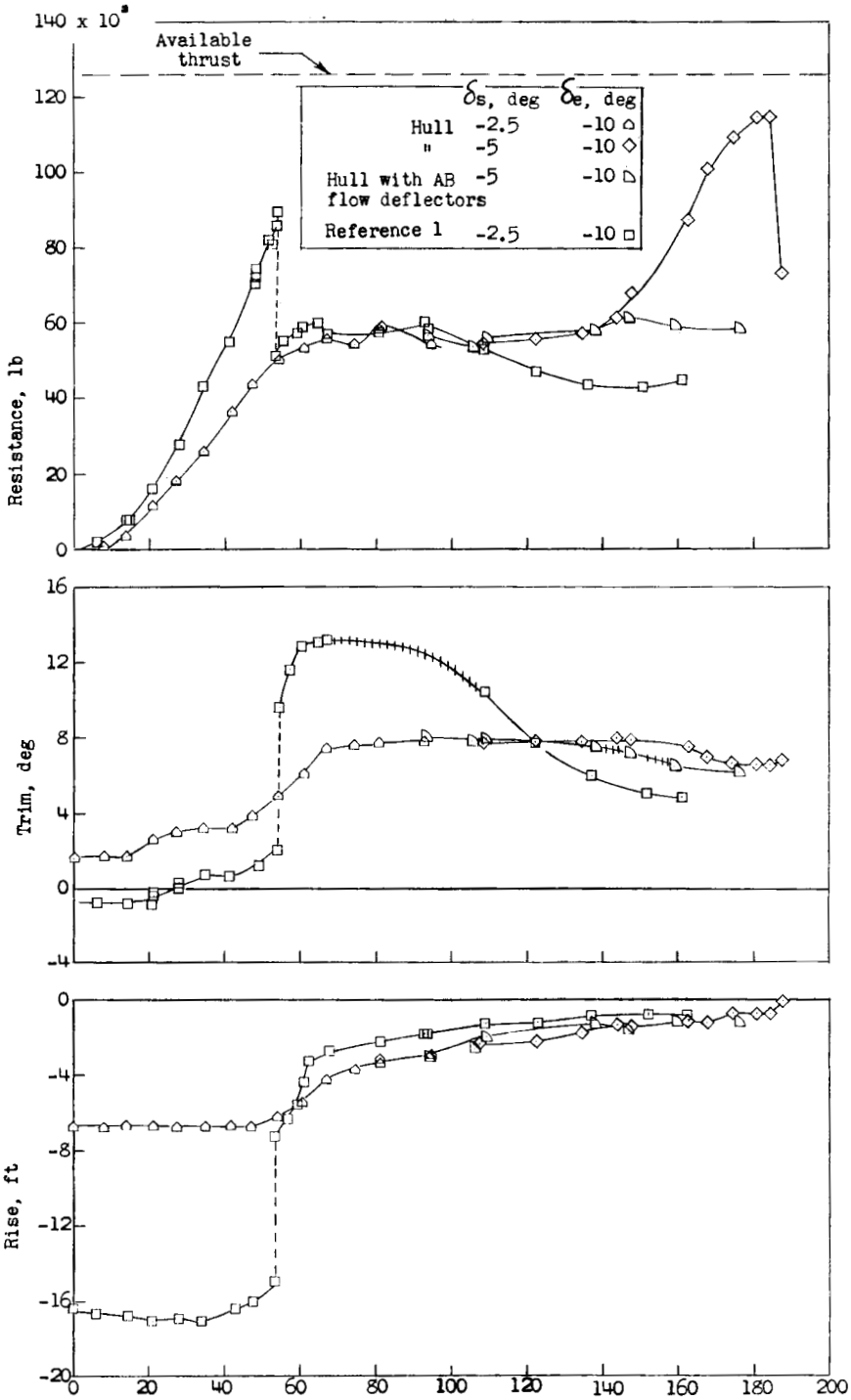

Figure 29.- The resistance, trim, and rise of the hull model compared with that obtained for a similar hydro-ski model (ref. 1).

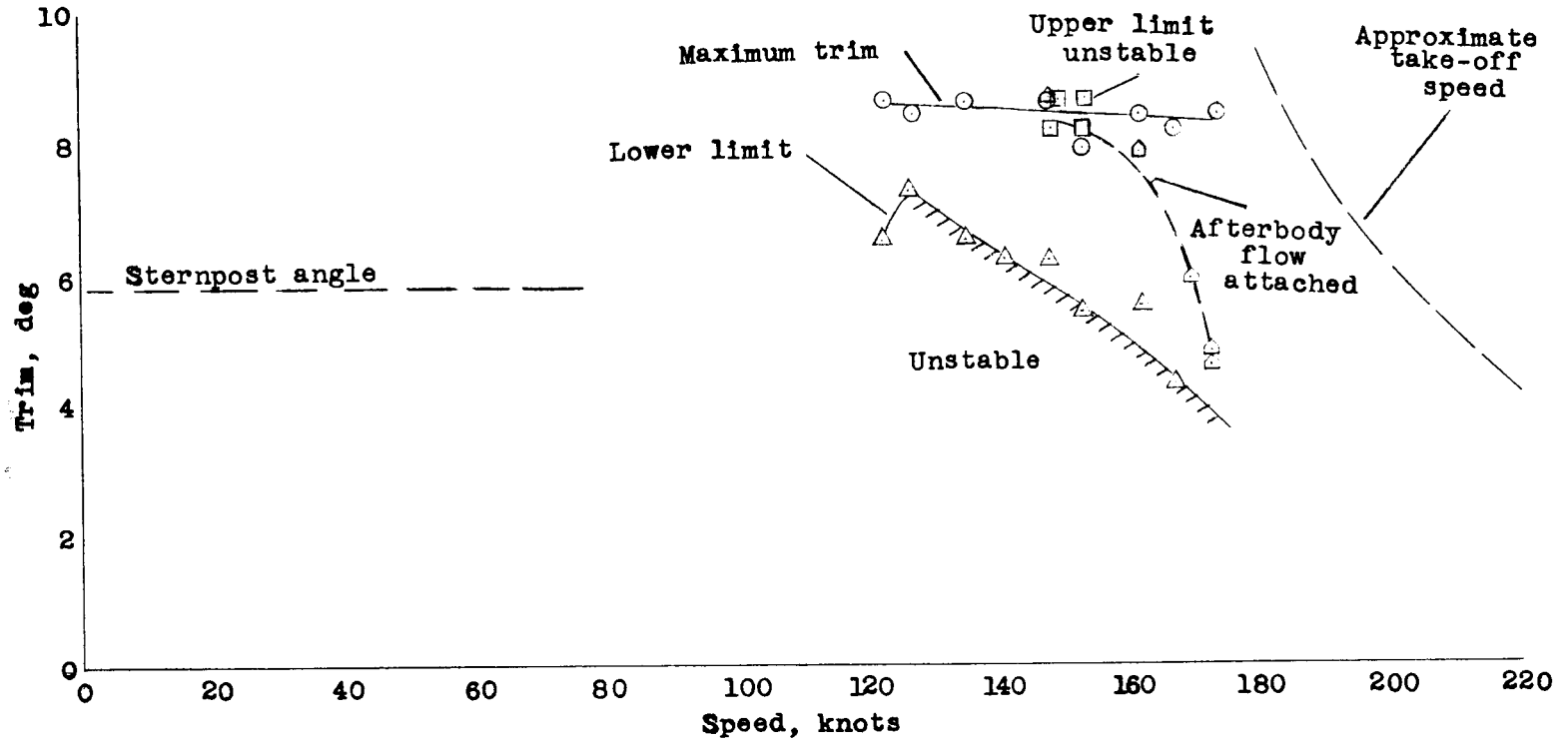

Figure 30.- Trim limits of stability. Gross load, 225,00 pounds.

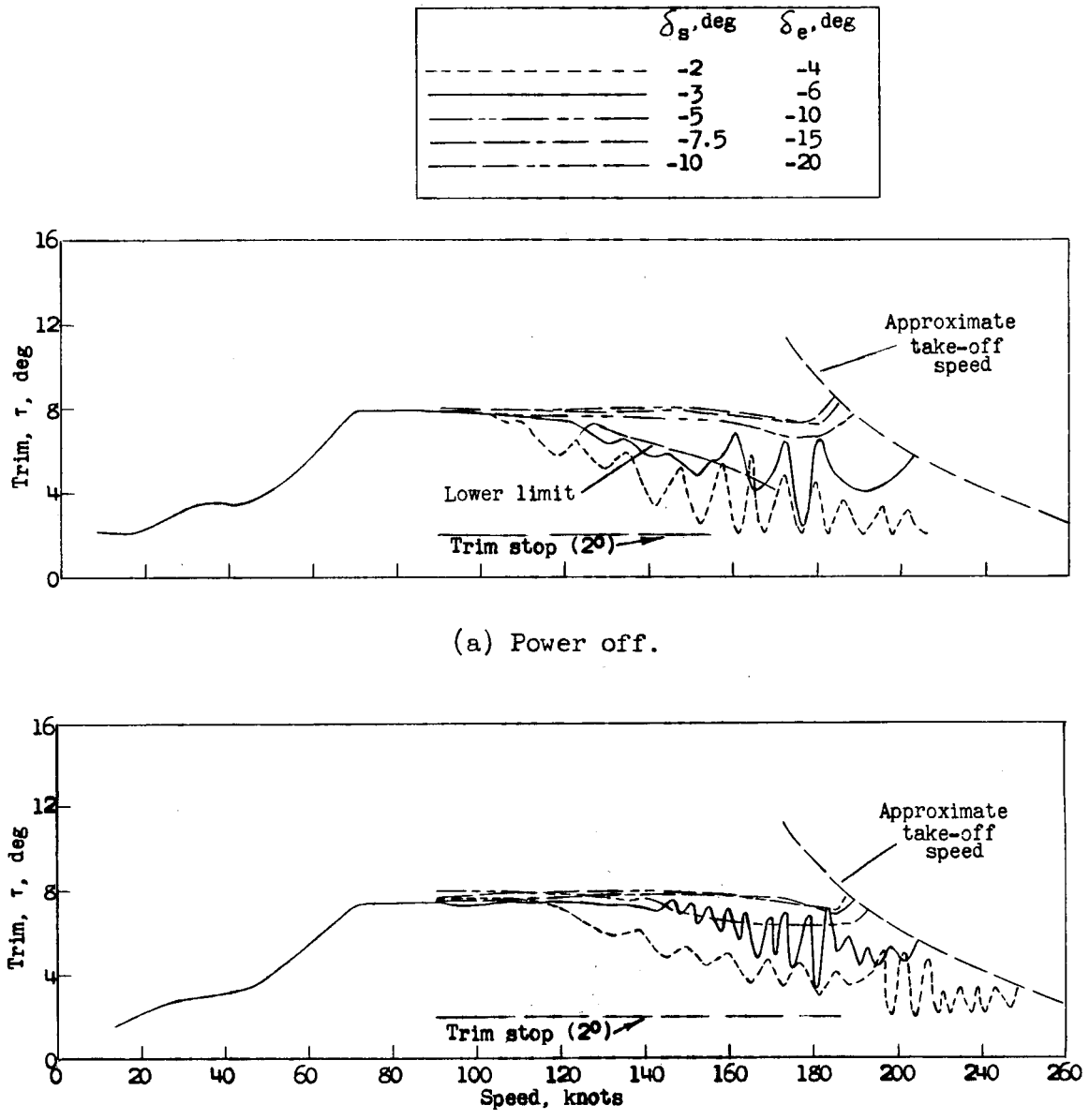

(a) Power off.

(b) Power on.

Figure 31.- Variations in trim during smooth-water take-offs for various stabilizer settings with and without power. Gross load, 225,000 pounds.

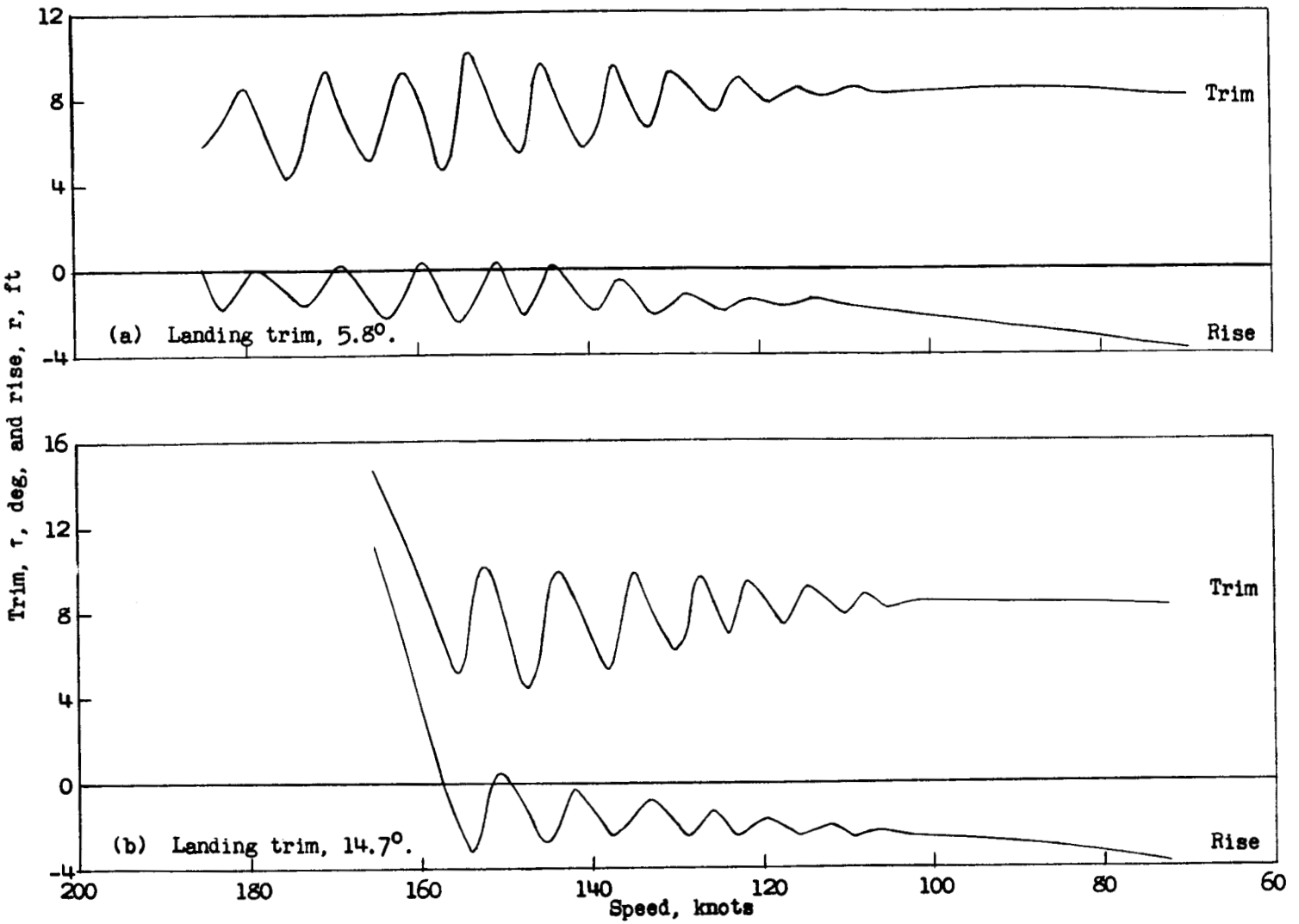

Figure 32.- Variation in trim and rise during two typical smooth-water landings.